Lehrstuhl für Werkstoffkunde und Werkstoffmechanik mit
Materialprüfamt für den Maschinenbau
Technische Universität München

A Fracture Mechanics Study of Tungsten Failure under High Heat Flux Loads

Muyuan Li

Vollständiger Abdruck der von der Fakultät für Maschinenwesen
der Technischen Universität München
zur Erlangung des akademischen Grades eines

Doktor-Ingenieurs (Dr.-Ing.)

genehmigten Dissertation.

Vorsitzender:	Univ.-Prof. dr. ir. Daniel J. Rixen
Prüfer der Dissertation:	
	1. Univ.-Prof. Dr. mont. habil. Dr. rer. nat. h. c. Ewald Werner
	2. Univ.-Prof. Dr. rer. nat. Rudolf Neu

Die Dissertation wurde am 28.10.2014 bei der Technischen Universität München
eingereicht und durch die Fakultät für Maschinenwesen
am 20.02.2015 angenommen.

Announcement

Parts of the results presented in this dissertation have been published in the following articles:

Muyuan Li, Ewald Werner, Jeong-Ha You, Fracture mechanical analysis of tungsten armor failure of a water-cooled divertor target, Fusion Engineering Design, 89 (2014) 2716-2725.

Muyuan Li, Mathias Sommerer, Ewald Werner, Stefan Lampenscherf, Thorsten Steinkopff, Philipp Wolfrum, Jeong-Ha You, Experimental and computational study of damage behavior of tungsten under high energy electron beam irradiation, Engineering Fracture Mechanics, 135 (2015) 64-80.

Muyuan Li, Ewald Werner, Jeong-Ha You, Cracking behavior of tungsten armor under ELM-like thermal shock loads: A computational study, Nuclear Materials and Energy, 2 (2015) 1-11.

Muyuan Li, Ewald Werner, Jeong-Ha You, Influence of heat flux loading patterns on the surface cracking features of tungsten armor under ELM-like thermal shocks, Journal of Nuclear Materials, 457 (2015) 256-265.

Abstract

The performance of fusion devices is highly dependent on plasma-facing components, which have to withstand stationary thermal loads as well as the thermal transients induced by the instabilities of the plasma confinement. Tungsten is the most promising candidate material for armors in the plasma-facing components in ITER and DEMO. However, the brittleness of tungsten below the ductile-to-brittle transition temperature is very critical to the reliability of the plasma-facing components. In this work, thermo-mechanical and fracture behaviors of tungsten are predicted numerically under fusion relevant thermal loadings, which are short transient thermal loads induced by edge localized mode (ELM), slow high-energy-deposition thermal loads (e.g. Vertical Displacement Event (VDE)) and stationary heat flux loads. The results are compared with the corresponding experimental observations, and the good agreement between the experimental observations and numerical predictions proves the validity of the computational approaches.

Zusammenfassung

Die Leistungsfähigkeit von Kernfusionsanlagen hängt stark von den dem Plasma zugewandten Komponenten ab, welche den stationären thermischen Belastungen ebenso standhalten müssen wie thermischen Belastungen, die auf Instabilitäten des Plasmas zurückzuführen sind. Für ITER und DEMO ist Wolfram als das vielversprechendste Material zum Schutz der plasmabelasteten Komponenten anzusehen. Allerdings stellt die Sprödigkeit von Wolfram unterhalb der Spröd-Duktil-Übergangstemperatur einen kritischen Faktor für die Zuverlässigkeit dieser plasmabelasteten Komponenten dar. Diese Arbeit zielt auf eine Prognose des thermo-mechanisches Verhaltens sowie des Bruchverhaltens von Wolfram ab - basierend auf numerischen Ansätzen unter Berücksichtigung der fusionsrelevanten thermischen Belastungen aufgrund von kurzen transienten thermischen Belastungen im Edge Localized Mode (ELM), einer langsamen hohen Energiedeposition unter thermischen Belastungen (z.B. eine schnelle vertikale Verschiebung des Plasmas / Vertical Displacement Event (VDE)) sowie des stationären Wärmeflusses. Die numerischen Vorhersagen werden entsprechenden experimentellen Beobachtungen gegenübergestellt - wobei eine gute Übereinstimmung die Gültigkeit der zugrundeliegenden Berechnungsansätze dieser Arbeit unterstreicht.

Acknowledgments

This dissertation has been carried out at the Institute of Materials Science and Mechanics of Materials at the Technische Universität München with Siemens AG and Max Planck Institute as cooperation partners.

First of all I would like to thank Prof. Ewald Werner for his guidance and for providing the opportunity to work on this topic. Furthermore, I would like to thank Prof. Rudolf Neu (Max Planck Institute) for reviewing the work. I would like to thank Prof. Rixen for being the chairman for the final defense.

I am very grateful to Prof. Jeong Ha You (Max Planck Institute) for giving me scientific supervision and for leading me to the fusion science research community.

I deeply appreciate that Prof. Hubertus von Dewitz (Siemens AG), Dr. Stefan Lampenscherf (Siemens AG) and Dr. Michael Metzger (Siemens AG) initiated this joint project and gave me support and inspiration. Furthermore, I would like to thank Dr. Philipp Wolfrum (Siemens AG) and Dr. Thorsten Steinkopff (Siemens AG) for their support and our discussions.

I would like to give many thanks to M.Sc. Mathias Sommerer for providing the experimental data and for many fruitful discussions and his valuable advice.

I acknowledge Dr. Christian Krempaszky for his helpful advice and our discussions. I would like to give special thanks to Yvonne Jahn for her support and organizational matters and Jinming Lu for his tips on writing the manuscript. I would also like to extend my thanks to colleagues at the Institute of Materials Science and Mechanics of Materials and Siemens AG, who have contributed to this work and provided a lot of help in the past four years.

This work was funded by Siemens AG. The financial support is gratefully acknowledged.

Last but not least, I would like to thank my wife Quanji, my son Dongxu and my parents, who gave me precious and constant support as well as motivation.

Muyuan Li

Garching, March 2015

List of Figures

List of Tables

List of Symbols and Abbreviations

The symbols (Latin letters and Greek letters) and abbreviations used in this dissertation are listed in the alphabetical order.

Latin letters

Symbol	
a	crack length
A	integration domain enclosed by the inner contour Γ
$\mathbf{B}$	pre-logarithmic energy factor matrix
$\mathbf{b}_i^{\alpha}$	nodal enriched degree of freedom vector
c	specific heat
C_{o}	outer contour
C_+, C_-	crack face contours
d	depth
d_{pen}	thermal penetration depth
D	scalar damage variable that represents the averaged overall damage
E	Young's modulus
E'	effective Young's modulus that equals to E for plane stress and $E/(1-\nu^2)$ for plane strain
E_{B}	energy of electron beam distributed at the sample surface
erfc	complementary error function
f	dimensionless function that depends on the load and the geometry
F	power density for the uniform loading
F_{ave}	averaged power density in the loading area
$F_{\mathrm{potential}}$	plastic potential in the sense of the associated flow rule

F_α	associated elastic asymptotic crack tip functions
G	energy release rate
G_c	critical energy release rate
G_I, G_II, G_III	energy release rates for mode I, mode II and mode III
h_{11}, h_{21}, h_{12}, h_{22}	weight functions
H	discontinuous jump function
$\mathbf{I}$	identity matrix
I_all, $I_\mathrm{Heaviside}$ and I_tip	set of nodal indices of the classical finite element method, set of node indices associated with crack separation away from the crack tip and set of node indices around crack
J	J-integral
$J^\mathrm{I}_\mathrm{aux}$	J-integral for an auxiliary, pure mode I, crack tip field
$\mathbf{J}_\mathrm{int}$	interaction integral vector
$J^\mathrm{I}_\mathrm{int}$, $J^\mathrm{II}_\mathrm{int}$, $J^\mathrm{III}_\mathrm{int}$	interaction integrals for mode I, mode II and mode III
k	thermal conductivity
K	stress intensity factor
$\mathbf{K}$	stiffness matrix
k_1	stress intensity factor in an auxiliary, pure mode I, crack tip field
K_Ic	fracture toughness
K_I, K_II, K_III	stress intensity factors for mode I, mode II and mode III
K_{nn}, K_{ss}, and K_{tt}	normal and two shear stiffnesses
M_1, M_2, M_3	coefficients in the weight functions for edge cracks in a semi-infinite space
$\mathbf{n}$	normal unit vector
N_i	nodal shape functions
P	power density
p	number of Gauss points in each element
q	heat flux
$\mathbf{q}$	crack extension vector
Q, b, C, γ	material parameters entering the Frederick-Armstrong constitutive model
q_1	any smooth function in A with the value ranging from zero on C_o to unity on Γ

R	radius of the loading area
r, θ	polar coordinates
r, φ, z	cylindrical coordinates
$\mathbf{S}$	deviatoric stress tensor
t	time
T	temperature
$\mathbf{t}$	traction vector
T_0	initial temperature
T_{base}	base temperature
t_{h}	heating time
T_{c}	temperature, below which yield stress of tungsten is not reached during cooling
T_{max}	maximum temperature
t_n, t_s, t_t	normal and two shear tractions
$\mathbf{u}_i$	nodal displacement vector
V	domain volume enclosing the crack tip or crack line
w_p	weight of the Gauss point
W	mechanical strain energy density
$\mathbf{x}$	Cartesian coordinates vector
x, y, z	Cartesian coordinates
x_1	Cartesian coordinate parallel to the crack
x_2	Cartesian coordinate perpendicular to the crack

Greek letters

Symbol	
α	coefficient of thermal expansion
$\dot{\boldsymbol{\alpha}}$	backstress rate tensor
$\boldsymbol{\alpha}'$	deviatoric backstress tensor
Γ	contour surrounding a crack tip
δ	Kronecker delta
$\boldsymbol{\delta}$	separation vector

δ_n, δ_s, δ_t	normal and two shear separations
ε	total strain
ε^0	initial strain
ε^{m}	mechanical strain
ε^{p}	total plastic strain in radial direction
$\varepsilon^{\mathrm{p}}_{\mathrm{e}}$	equivalent plastic strain
$\varepsilon^{\mathrm{e}}_{\mathrm{h}}$, $\varepsilon^{\mathrm{p}}_{\mathrm{h}}$ and $\varepsilon^{\mathrm{t}}_{\mathrm{h}}$	elastic, plastic and thermal strains in radial direction generated during heating
$\varepsilon^{\mathrm{e}}_{\mathrm{c}}$, $\varepsilon^{\mathrm{p}}_{\mathrm{c}}$ and $\varepsilon^{\mathrm{t}}_{\mathrm{c}}$	elastic, plastic and thermal strains in radial direction generated when the temperature is decreased from T_{max} to T_{c}
$\varepsilon^{\mathrm{e}}_{rr}$, $\varepsilon^{\mathrm{e}}_{\varphi\varphi}$, $\varepsilon^{\mathrm{e}}_{zz}$	elastic strains in radial, circumferential and axial directions
$\varepsilon^{\mathrm{p}}_{rr}$, $\varepsilon^{\mathrm{p}}_{\varphi\varphi}$, $\varepsilon^{\mathrm{p}}_{zz}$	plastic strains in radial, circumferential and axial directions
κ	thermal diffusivity
μ	shear modulus
ν	Poisson’s ratio
ρ	density
$\boldsymbol{\sigma}$	stress tensor
σ_0	yield stress
σ_{e}	equivalent stress
σ_{ij}	components of stress tensor
σ_{n}	normal stress
σ_{max}	maximum principal stress
σ^0_{max}	maximum allowable principal stress
$\sigma_{rr}, \sigma_{\varphi\varphi}, \sigma_{zz}$	stresses in radial, hoop and axial directions
$\varPhi, \varPsi$	level-set functions

Abbreviations

Abbreviation	
CFC	carbon fiber composite
COD	crack opening displacement
DBTT	ductile-to-brittle transition temperature
DEMO	DEMOnstration Power Plant
ELM	edge localized mode
FE	finite element
FEM	finite element method
HHF	high heat flux
H-mode	high confinement mode
ITER	International Thermonuclear Experimental Reactor
JUDITH	Jülich Divertor Test Equipment in Hot Cells
L-mode	low confinement mode
LM	light microscopic
LSM	laser scanning microscopic
MPS	maximum principal stress
OECD	Organization for Economic Co-operation and Development
PFC	plasma-facing component
PFM	plasma-facing material
RT	room temperature
SIF	stress intensity factor
SOL	Scrape-Off-Layer
TBM	test blanket modules
TZM	molybdenum alloy containing (in mass %) 0.50 titanium, 0.08 zirconium and 0.02 carbon
W-UHP	ultra-high purity tungsten

WTa1	tungsten alloy with 1 mass% tantalum
WTa5	tungsten alloy with 5 mass % tantalum
VCE	virtual crack tip extension
VDE	vertical displacement event
VT	vertical target
XFEM	extended finite element method

Contents

Chapter 1

Introduction

Secure, reliable, affordable and clean energy supplies are fundamental to global economic growth and human development. Since the beginning of industrialization, energy consumption has increased significantly. Energy demand, especially in non-OECD (Organization for Economic Co-operation and Development) countries will continue to increase, driven by the fast economic growth, as predicted in figure 1.1. At present, 80% of the world's energy consumption is based on fossil fuels, and this situation cannot be changed in the near future. The high percentage of fossil fuels in the energy consumption is not a long-term solution to the world energy problem. As fossil fuel is a limited resource, the global consumption of coal, gas and oil will have to be reduced significantly in the future. In recent years, due to environmental problems induced by the fossil fuels consumption - namely, the greenhouse effect and the effects of acidic pollution - many countries have restricted their CO_2-emissions, which exacerbates the energy problem. As a result, environmentally friendly and low cost forms of renewable energy from inexhaustible sources such as hydroelectric power have become quite common and are still spreading fast. But most supplies from renewable sources are reliant on environmental conditions and are, therefore, not guaranteed to be constant. In addition, hydroelectric power, which provides far more energy than other renewable energy sources (e.g. biomass, solar, and wind power), will lead to environmental damages, too.

Other than renewable energy, nuclear fission is a controversial option for the energy supply, and it satisfies about 5% of the world's energy demand. As it is shown in figure 1.1, a large portion of the increase in energy consumption is driven by power generation, in which nuclear fission plays a very important role. Nuclear fission provides about 11% of the world's electricity and almost 22% of the electricity in OECD countries. Greenhouse gas emissions of nuclear power plants are among the lowest of any electricity generation method, since nuclear power plants do not release any gases such as carbon dioxide or methane which are largely responsible for the greenhouse effect. Nuclear fission is reliable and efficient. Nuclear energy can be produced from nuclear power plants even under rough weather conditions - and it needs only a small amount of fuel compared to producing the same amount of energy by relying on fossil fuel. However, the disadvantages of nuclear fission are obvious as well, e.g. the safety issues during transport of nuclear materials, disposal of nuclear waste, possible leakage of radioactive material from the reactor and the potential risk of accidents occurring while operating the reactor. As a result, the use of nuclear fission is curtailed by issues of public and political acceptability, especially after the Fukushima catastrophe in 2011.

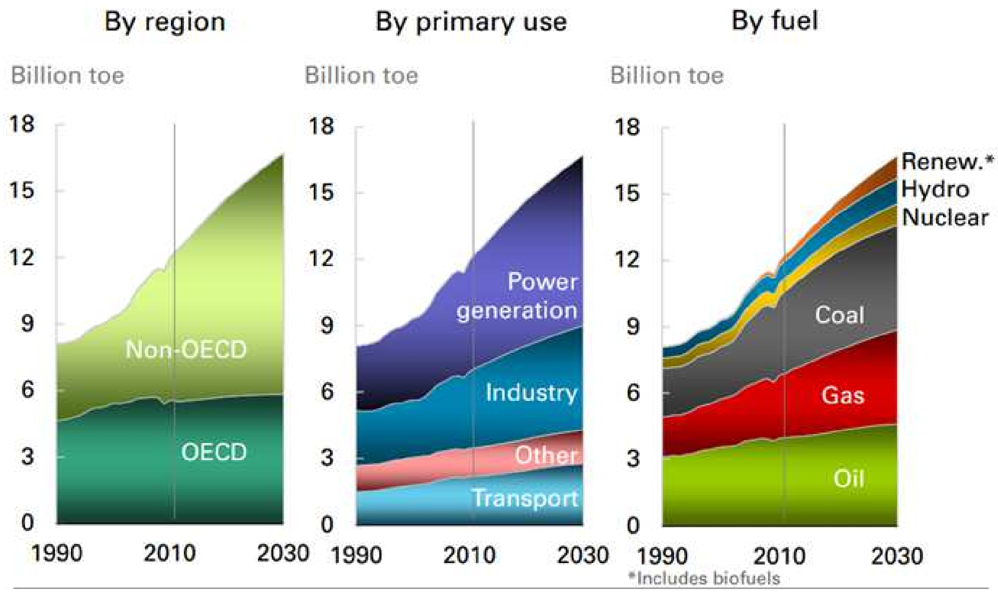

Figure 1.1: History and outlook of the world energy consumption by region, primary use and fuel [1]. The tons of oil equivalent (toe) is a unit of energy defined as the amount of energy released by burning one ton of crude oil. It is approximately 42 gigajoules.

Under these circumstances, a new, sustainable energy source must be developed to solve the world's energy crisis, and nuclear fusion is considered as a potential solution. Basically, nuclear fusion could serve to meet all energy demands. One kilogram of fusion fuel can provide the same amount of energy as 10 million kilograms of fossil fuel, and fuel supply for nuclear fusion is almost unlimited. Unlike nuclear fission, nuclear fusion is intrinsically safe: if some damage occurs in the fusion reactor or if the fusion reactor is out of control, the conditions for fusion reactions cannot be fulfilled any more, and fusion reactions and heat generation will rapidly cease. Furthermore, the fusion process does not lead to greenhouse gas emissions and leaves no long-term radioactive waste (all waste will be recyclable within 100 years).

1.1 Principle of nuclear fusion

Nuclear fusion is the process that powers the Sun and all other stars, where two or more nuclei collide and join together to form a heavier nucleus. The challenge of producing energy from nuclear fusion is to create conditions similar to those in a star here on an earthly scale. If the matter is sufficiently heated, the fusion reaction may occur due to collisions of particles with extreme kinetic energies, since the higher the temperature, the faster the nuclei move. In order to achieve a nuclear fusion reaction, it is necessary to heat up these nuclei to extremely high temperature of nearly 150 million degrees Celsius. At such extremely high temperatures, electrons are separated from nuclei, forming a hot, electrically charged gas (plasma). If this condition can be maintained long enough (e.g. a couple of seconds), the nuclei will be held together for nuclear fusion to occur. The mass of the resulting heavier nucleus is not the exact sum of the two initial nuclei, and huge energy quantities are released when the average mass of the nuclei involved in the process decreases. The quantity of released energy relates to Einstein’s famous equation, which states that the universal proportionality factor between equivalent amounts of energy and mass is equal to the speed of light squared. Usually, nuclear fusion processes involve two light nuclei. If the combined nuclear mass is larger than a threshold, a fission reaction must occur. The threshold is the most stable element in the periodic table, Iron-56, which has the largest average binding energy per nucleon, as shown in figure 1.2. If an element is significantly more massive than Iron-56, it can be broken up, producing lighter, more stable elements, and releasing energy, which is the nuclear fission process.

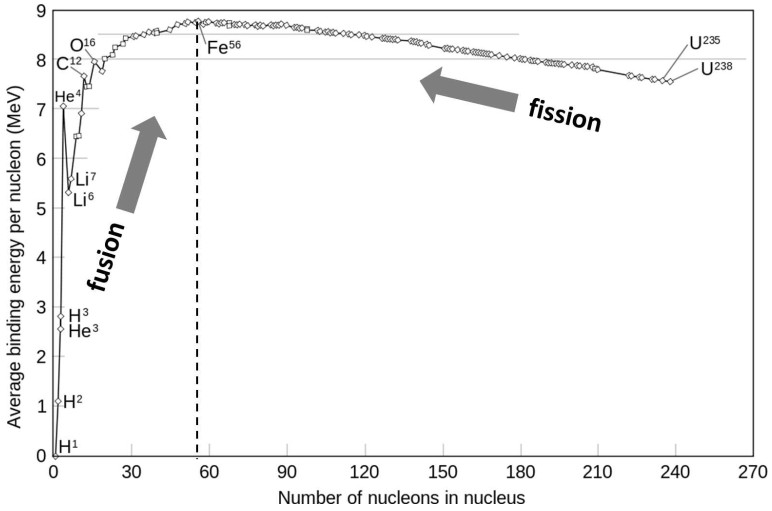

Figure 1.2: Average nuclear binding energy per nucleon as a function of number of nucleons in the atomic nucleus. Less massive elements, up to Iron-56, can participate in fusion reactions, while more massive elements than Iron-56 can participate in fission reactions. Adapted from [12].

In the fusion reaction, the nuclear force that combines together atomic nuclei (protons and neutrons) only acts over extremely small distances. Before two positive nuclei approach each other close enough to undergo a fusion reaction, they need sufficient energy to overcome a substantial energy barrier of electrostatic forces, the Coulomb barrier. The concept of a cross section is used to express the quantitative probability that a pair of nuclei cross the Coulomb barrier.

The experimentally determined cross sections are shown in figure 1.3 for the most common fusion reactions. Of the three fusion processes, the deuterium-tritium fusion reaction is the most efficient reaction in terms of energy release. It shows the lowest necessary average kinetic energy for starting fusion reactions, the highest cross section and a high energy yield. The deuterium-tritium fusion

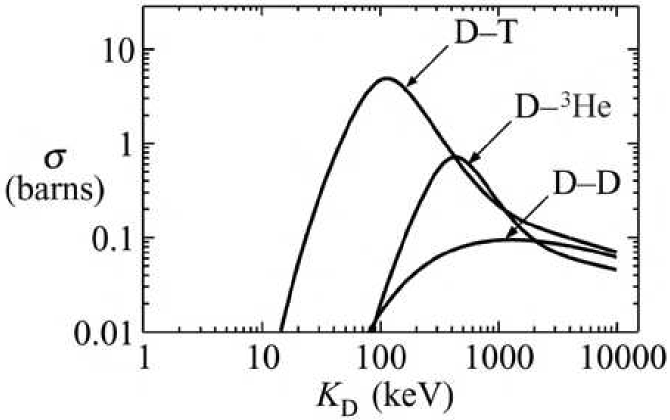

Figure 1.3: Experimentally determined cross sections for the deuterium-tritium (D-T), deuterium-^{3}He (D-^{3}He), and deuterium-deuterium (D-D) fusion reactions as a function of the deuterium average kinetic energy [13].(1 barn = 10^{-28} m^2)

reaction generates a helium (He) nucleus and a free neutron (n) and releases 17.6 MeV binding energy, see figure 1.4. Some other promising fusion reactions are

$$\mathrm{D} \quad + \quad \mathrm{D} \quad \longrightarrow \quad {}^3\mathrm{He} \quad (0.82\,\mathrm{MeV}) \quad + \quad \mathrm{n} \quad (2.45\,\mathrm{MeV}), \tag{1.1}$$

$$\mathrm{D} \quad + \quad \mathrm{D} \quad \longrightarrow \quad \mathrm{T} \quad (1.01\,\mathrm{MeV}) \quad + \quad \mathrm{H} \quad (3.02\,\mathrm{MeV}), \tag{1.2}$$

$$\mathrm{D} \quad + \quad {}^3\mathrm{He} \quad \longrightarrow \quad {}^4\mathrm{He} \quad (3.6\,\mathrm{MeV}) \quad + \quad \mathrm{H} \quad (14.7\,\mathrm{MeV}). \tag{1.3}$$

The fuel for deuterium-tritium fusion is abundant. Deuterium is available in great quantities as it can be extracted from all forms of water (10 g of deuterium can be extracted from 500 l of water). Tritium does not occur naturally since it has a half-life of 10 years. The most promising source of tritium is the breeding of tritium from lithium-6 by neutron bombardment with the reaction:

$${}^6\mathrm{Li} \quad + \quad \mathrm{n} \quad \longrightarrow \quad {}^4\mathrm{He} \quad (2.05\,\mathrm{MeV}) \quad + \quad \mathrm{T} \quad (2.73\,\mathrm{MeV}), \tag{1.4}$$

which can be archived by slow neutrons. Natural lithium contains about 7.5 percent lithium-6, the rest being lithium-7. With fast neutrons, tritium can be bred from the more abundant lithium-7:

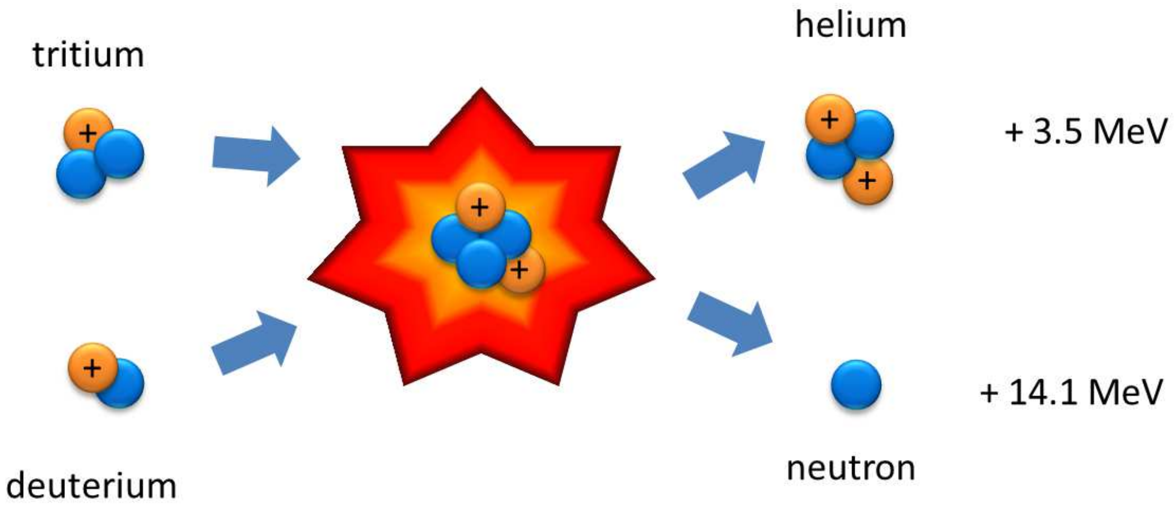

Figure 1.4: The deuterium-tritium fusion.

$$^{7}\mathrm{Li} \quad + \quad \mathrm{n} \quad \longrightarrow \quad ^{4}\mathrm{He} \quad (2.05\,\mathrm{MeV}) \quad + \quad \mathrm{T} \quad + \quad \mathrm{n} \quad - \quad (2.47\,\mathrm{MeV}). \qquad (1.5)$$

1.2 Nuclear fusion devices

Since the 1950s, nuclear fusion researchers have attempted to perform controlled thermonuclear experiments [14]. Two approaches were developed to achieve the fusion reaction: the inertial confinement and the magnetic confinement. Inertial confinement reactors serve to put a high enough energy density into a small pellet of a mixture of deuterium and tritium so that they fuse within such a short time that they cannot move appreciably. The strategy of the magnetic confinement reactor is to confine the hot plasma by means of magnetic fields, keeping it in perpetually looping paths and away from the wall of the container. The tokamak is the most developed magnetic confinement system. It was invented in the Soviet Union during the 1960s and soon became the dominant concept in nuclear fusion research. In a tokamak the plasma is held in a doughnut-shaped vessel. A magnetic field is generated by using special coils, causing the plasma particles to move around in spirals without touching the wall of the chamber, see figure 1.5.

In 1985, the International Thermonuclear Experimental Reactor (ITER) project was proposed [15]. ITER is a large-scale scientific experiment that aims to demonstrate the possibility of producing energy commercially from fusion reactions. In ITER, the fusion reaction will be achieved in a tokamak device that uses magnetic fields to contain and control the hot plasma. The fusion reaction in ITER takes place between deuterium and tritium (D-T).

ITER will pave the way for the DEMOnstration Power Plant (DEMO) that can produce electrical

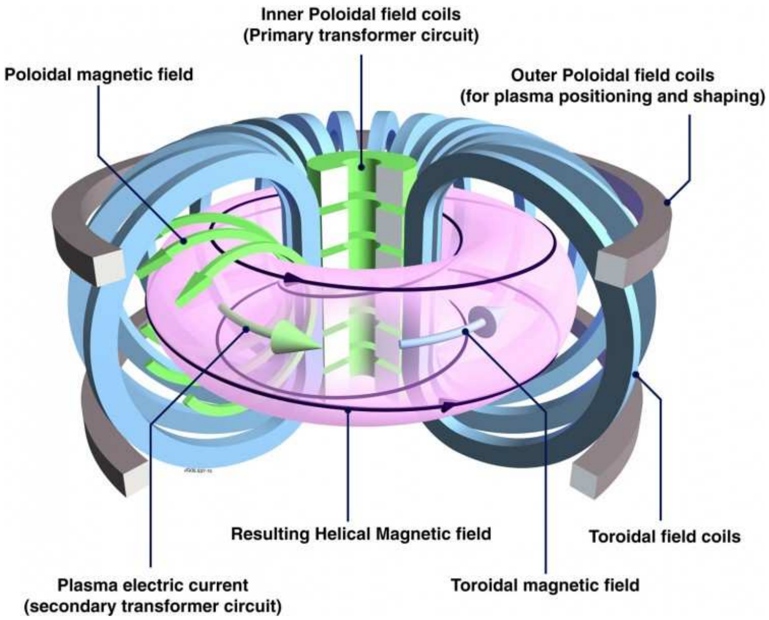

Figure 1.5: The tokamak principle enclosing the fusion plasma inside a torus with a helical magnetic field and plasma current [2].

power and can also be commercialized. DEMO is notably intended to be the first fusion reactor to generate electrical power. Earlier experiments, such as ITER, merely dissipate the thermal power they produce into the atmosphere as steam, while DEMO will use the steam to drive a turbine and thus to produce electricity, see figure 1.6.

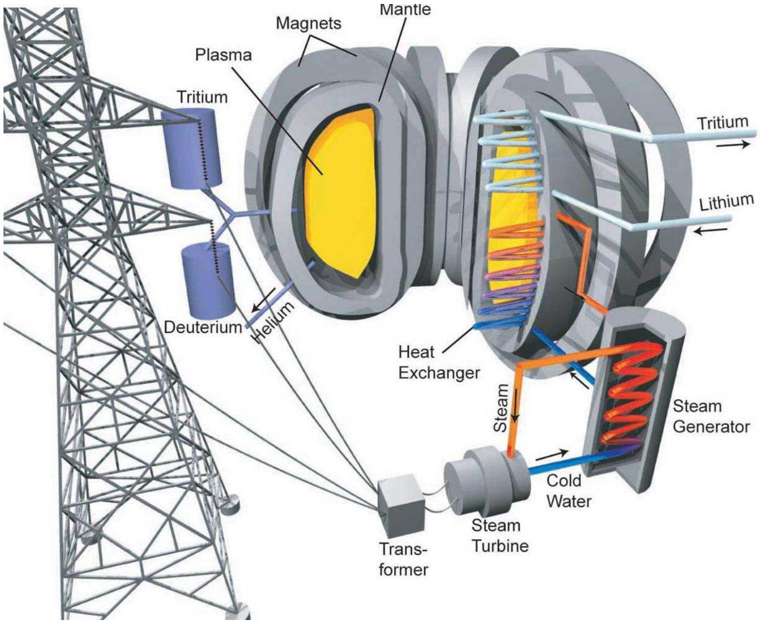

Figure 1.6: Artists impression of a fusion power plant [2].

1.3 Plasma-facing components

Although strong magnetic fields are used to keep the plasma away from the walls in the fusion reactors, the plasma-facing components (PFCs) in every fusion device are unavoidably exposed to particles with high kinetic energies from the plasma. The PFCs of ITER directly face the thermonuclear plasma and cover an area of about 850 m^2, including the divertor, the blanket and the test blanket modules (TBM) with their corresponding frames, as shown in figure 1.7. The main functions of the PFCs are [3]:

- Absorb the radiated and conducted heat from the plasma and contribute to the absorption of neutronic heating,

- Minimize the plasma impurity content,

- Provide limiting surfaces that define the plasma boundary during startup and shutdown,

- Contribute to the plasma passive stabilization.

The PFCs will be placed under extreme thermo-physical conditions, and the lifetime of the PFCs is limited mainly by thermal loads and thermally induced mechanical stresses to these components [4]. Figure 1.8 shows the ITER's relevant heat flux load conditions as a function of power density and duration. On the first wall of the blanket, the thermal load during the cyclic plasma operation reaches

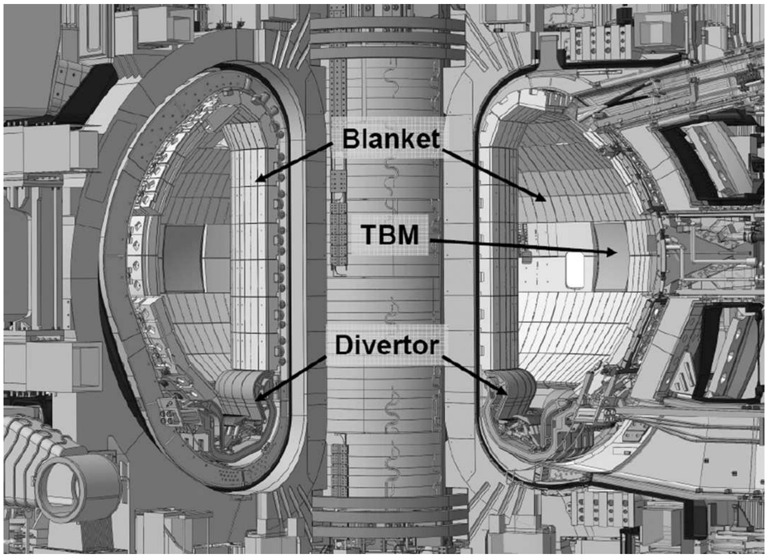

Figure 1.7: ITER plasma-facing components [3].

a power density of up to 0.5 MW/m^2. Compared to the thermal loads on the first wall, the thermal loads on the divertor are much more critical. During normal operation the maximum stationary heat flux load is assumed to be 10 MW/m^2 on the divertor. However, 20 MW/m^2 during 10 s can be reached during slow transient phase [3]. Other than the stationary heat flux load, the divertor has to withstand the transient events such as disruptions, edge localized modes (ELMs) and vertical displacement events (VDEs), which show a much higher energy deposition. Of the transient events, disruptions and VDEs are more difficult to be accommodated than ELMs, since they have a longer duration than ELMs. Therefore, to avoid or at least to mitigate disruptions and VDEs is highly suggested for fusion power plant applications. The divertor is required to withstand the stationary heat flux loads and ELMs during the normal operation.

The ITER divertor consists of 54 cassettes in a circular array [3]. The divertor cassette body is reusable to minimize activated waste, and it provides neutron shielding, routes the water coolant and supports the different PFCs, which consist of the dome, particle reflector plates, and inner and outer vertical targets (VTs), as shown in figure 1.9. The inner and outer VTs are the PFCs that intercept the magnetic field lines and consequently remove the heat load coming from the plasma via conduction, convection and radiation. The VT consists of a number of tungsten mono-blocks. The tungsten mono-block is bonded to the coolant tube via a copper interlayer (thickness range: 0.5-1.5 mm). The coolant tube is made of a CuCrZr alloy and is joined to a 316L steel pipe outside the plasma-facing region. The copper interlayer is applied to reduce the joint interface stress. In order to increase the critical heat flux limit of the water coolant, a twisted tape is inserted into the straight part of the cooling tube. The thickness of tungsten (shortest distance between the loading surface of the tungsten mono-block and the copper interlayer) needs to be large enough to resist the erosion during its lifetime. However, increasing the thickness of tungsten will also lead to an increase in the

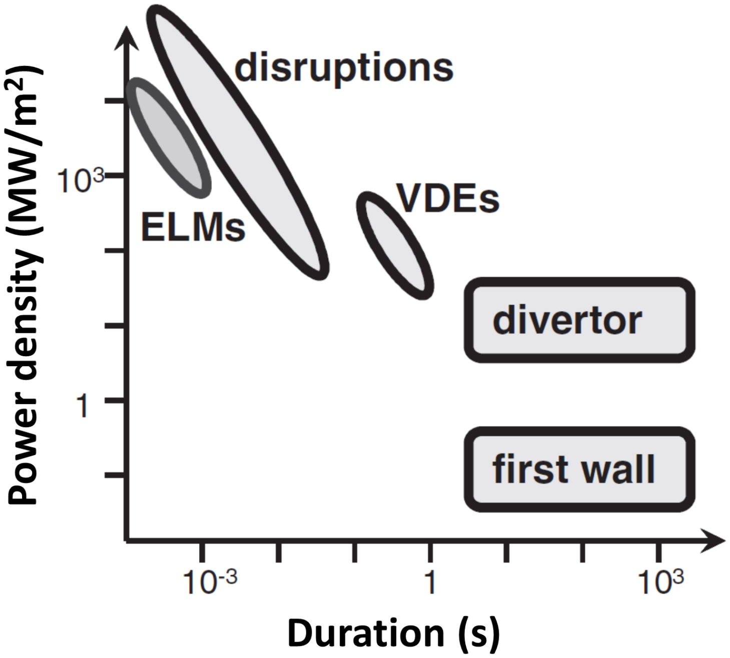

Figure 1.8: Plasma induced thermal loads on plasma facing components in ITER [4].

maximum temperature, which can activate the recrystallization process of tungsten. Therefore, the design of tungsten thickness must take both the lifetime of the divertor and the maximum temperature in the tungsten mono-block into consideration.

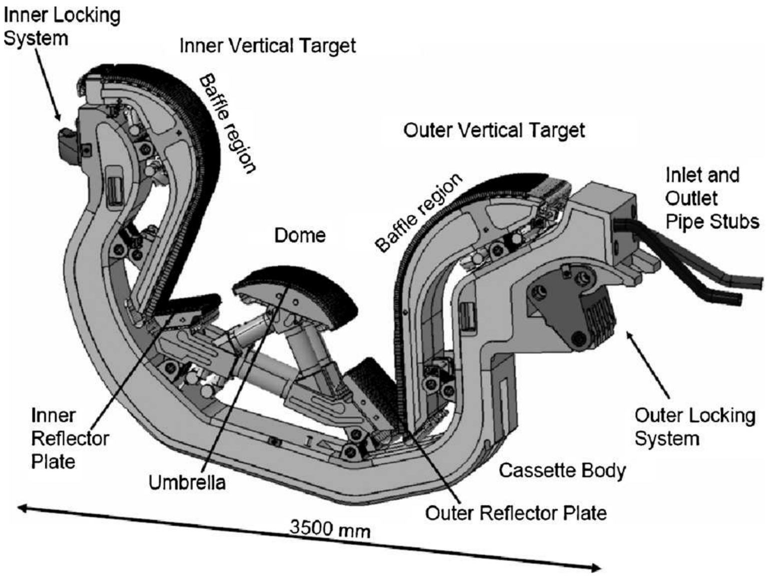

Figure 1.9: Schematic of an ITER divertor cassette [3].

1.4 Tungsten as plasma-facing material

The PFCs consist of a plasma-facing material (PFM) as armor mounted onto a heat sink and supported by a structural/shielding material. The working conditions of the PFMs are very complex, and thermal fatigue and thermal shock are considered to be the most critical issues. To select the PFM, however, not only the thermal shock and thermal fatigue resistance have to be taken into account, but also physical requirements (allowable impurity levels in the plasma), erosion lifetime, neutron radiation resistance, tritium retention, vacuum compatibility, integrity of armor and heat sink materials, possibility of the armor repairing [16]. To meet these requirements, many PFMs were tested over the last few decades, and three different PFMs - beryllium (Be) for entire main chamber wall, carbon fiber composite (CFC) at the divertor strike points and tungsten (W) on the baffles and dome - were chosen for the initial operation phase, as shown in figure 1.10.

In ITER, it was planned to begin operations with a primarily CFC-based divertor and replace it with a full tungsten divertor before the start of nuclear operation. Then, however, a new plan was proposed, and a full tungsten divertor will be employed from the very beginning [15]. This measure will serve to reduce substantial costs - but the tungsten divertor's aptness to withstand the extreme conditions in ITER needs to be assessed first, as the CFC was planned for regions of the divertor's vertical targets that are expected to be subjected to the highest heat loads.

As a PFM, tungsten has appropriate thermo-physical properties necessary for thermal shock resistance, e.g. the highest melting point of all metals, a high thermal conductivity and a low vapor pressure. Tungsten has low tritium retention, while carbon reacts chemically with the plasma fuel tritium and traps the fuel like a sponge leading to enhanced material erosion and unacceptable levels of tritium retention within the machine. Furthermore, there is sufficient tungsten available for in-

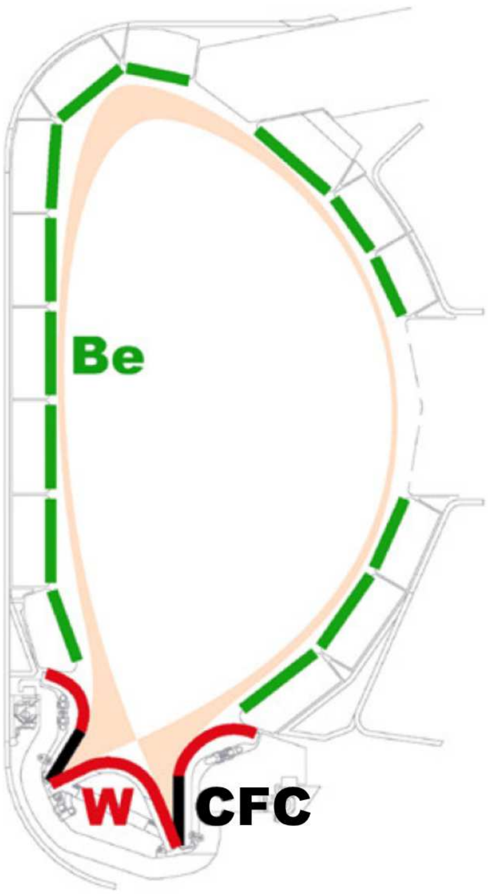

Figure 1.10: ITER plasma-facing materials for the initial operation phase with hydrogen. Adapted from [17].

dustrial applications, even if additional tungsten is needed to exchange the reactor components [18]. This is a great advantage, especially considering that the required amount of tungsten for PFCs in ITER is about 85 t.

The disadvantages of tungsten are its difficult manufacturability, high neutron activation and high volatility of its oxides. The most critical weakness of tungsten with respect to cracking is that it is very brittle under its ductile-to-brittle transition temperature (DBTT). The DBTT of a commercial tungsten grade ranges between 400 °C and 700 °C depending on the loading modes [19].

1.5 Scope of the dissertation

The performance of fusion devices is highly dependent on PFCs, the lifetime of which is limited by thermally induced damages. Thus, to assess the thermally induced damages is of great interest for the design studies for ITER and DEMO. The aim of this dissertation is to understand the mechanism of brittle cracking in the tungsten armor of the PFCs and to predict tungsten's thermo-mechanical and fracture behaviors numerically. In this dissertation a fracture mechanics analysis of tungsten failures is performed under three thermal loading scenarios - namely short transient thermal loads, slow high-energy-deposition thermal loads and stationary heat flux loads.

Short transient thermal loads

To mimic ITER-relevant short transient thermal loads (e.g. ELMs), electron beam facilities have been frequently applied, and response of tungsten under electron beams is shown in figure 1.11. When the electron beams hit a tungsten surface, massive heat is generated causing a very high temperature and a steep temperature gradient in the vicinity of the loading area. The hot material in the loading area is constrained by the surrounding bulk material. The material in the loading area is in a compressive stress state and plastic strains are readily generated, due to the low yield stress of tungsten at high temperatures. When the electron beam loading is stopped, the temperature drops drastically within a short time, and the material contracts quickly. During cooling, the material in the loading area is subjected to tensile stresses, which provide the driving force to open cracks. Thermal loads with smaller power densities merely lead to surface roughening. By increasing the power density, cracks can be generated during cooling. By further increasing the power density, surface temperature will eventually exceed the melting point of tungsten and resolidation occurs. In this dissertation, a fracture mechanics study for tungsten failure is conducted under ELM-like thermal loads that do not cause the surface of tungsten samples to melt.

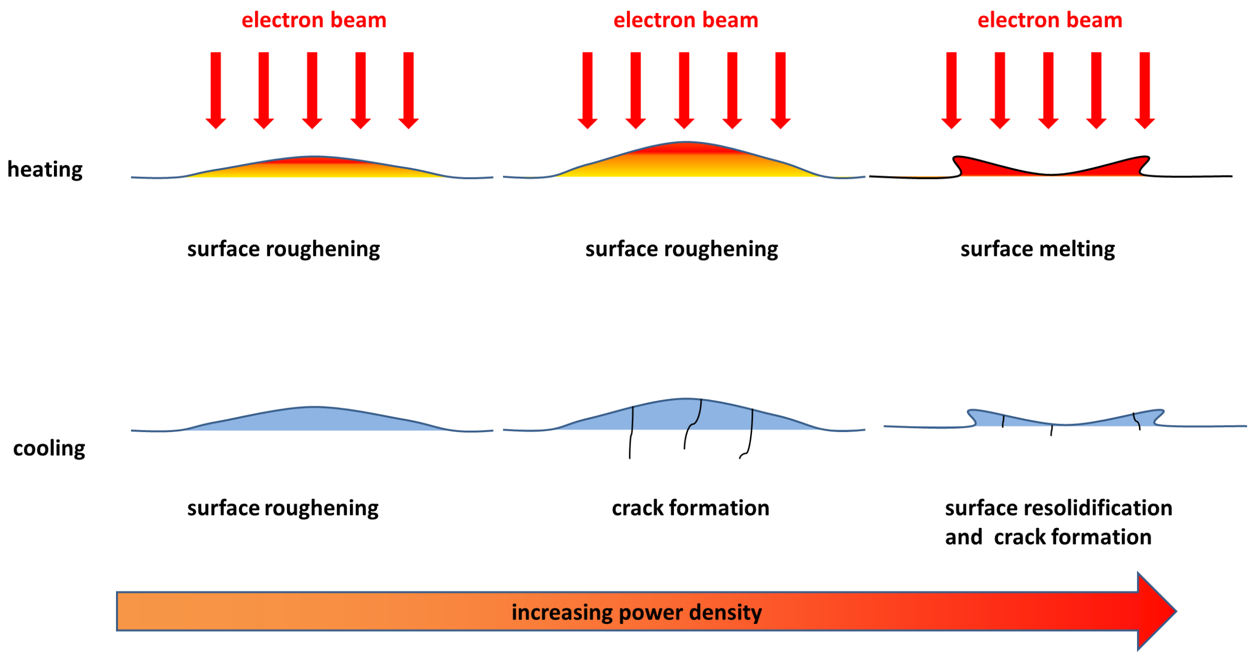

Figure 1.11: Response of tungsten under electron beams.

Slow high-energy-deposition thermal loads

Besides short transient thermal loads, the PFCs will be facing slow high-energy-deposition thermal loads, which have a much longer duration. A typical example is to be seen in the VDE. The deposited energy densities ($60\,\text{MJ/m}^2$) resulting from the VDE along with the long pulse duration, which is nearly three magnitudes higher of the pulse duration of the ELMs, usually lead to the melting of PFCs' surface and the subsequent redistribution of the PFM. Melting of tungsten is beyond the scope of this dissertation. However, the VDE is a uncontrolled scenario and its mechanism remains unclear. If the thermal loading induced by the VDEs is limited to an area that is sufficiently small, the temperature will not exceed the melting point of tungsten. In this dissertation, the behavior of tungsten is studied under VDE-like thermal loads assuming the loading area is limited so that no melting of tungsten occurs.

Stationary heat flux loads

The stationary heat flux load is not as intensive as thermal transient loads, and usually no plastic deformation is generated in tungsten during the operation purely due to the stationary heat flux load. However, the stationary heat flux loads impose a strong constraint on the structure-mechanical performance of the divertor during the operation. Thus, the combination of brittleness and the thermally induced stress fields due to the stationary heat flux loads raises a serious reliability issue concerning the structural integrity of tungsten armor. In this dissertation, the failure of a water-cooled divertor target is studied under ITER and DEMO relevant stationary heat flux loads.

1.6 Outline

This dissertation is organized as follows. Chapter 2 focuses on the theoretical background of the fracture mechanics studies conducted in this dissertation, and the methods for calculating stress intensity factors and J-integrals are presented. Also, the principle of the extended finite element method (XFEM) is introduced.

In chapter 3, a simplified analytical solution of temperature, stress and strain is derived under ELM-like transient thermal loading in a semi-infinite space. Based on the analytical stress solution, stress intensity factors are calculated by using the weight function method. In order to enable a more precise analysis, the finite element model is built according to the setup of thermal shock experiments at Forschungszentrum Jülich. The fracture behavior of tungsten is studied by means of two different types of computational approaches, namely, XFEM and the FEM-based virtual crack tip extension (VCE) method. A series of parametric simulations are conducted to study the impact of power density, base temperature and loading pattern on thermo-mechanical and fracture mechanical behaviors of tungsten.

Chapter 4 focuses on a numerical investigation of the thermo-mechanical and fracture behaviors of tungsten under slow high-energy-deposition thermal loads. The maximum temperature, surface roughness and crack occurrence are predicted and compared with the results of the thermal shock experiments undertaken at Siemens Healthcare.

In chapter 5, an extensive finite element analysis of the fracture mechanical behavior of a tungsten mono-block divertor target is carried out under consideration of ITER and DEMO relevant stationary heat flux loading conditions.

In chapter 6, the conclusions drawn from this dissertation are presented and further improvements of the current fracture mechanical simulations are proposed.

Chapter 2

Computational fracture mechanics approaches

This chapter serves to describe the research methodology of computing stress intensity factor, J-integral, crack initiation and crack propagation. In this chapter, after a brief overview of the fundamental concepts of fracture mechanics, the principle of the weight function method is introduced. The methods for computing stress intensity factor and J-integral in the commercial FEM code ABAQUS are described. In the end, the concept of XFEM to predict crack initiation and propagation is explained.

2.1 Fundamental concepts of fracture mechanics

The brittle cracking of tungsten under thermal shocks is essentially related to the brittleness of tungsten at low temperatures. Thus, the fracture behavior of tungsten below DBTT can in principle be interpreted with linear elastic fracture mechanics. The foundation of fracture mechanics, or more specifically, the foundation of linear elastic fracture mechanics was laid in the 1920s by Griffith [20]. A material fractures when sufficient stress is applied at the atomic level to break the bonds that hold atoms together. The strength is supplied by the attractive forces between atoms. In practice, however, it is found that the observed fracture strength is much smaller than the theoretical stress needed for breaking atomic bonds. Griffith explained the discrepancy between observed fracture strength and theoretical cohesive strength by inherent defects such as pre-existing micro-cracks in brittle materials leading to stress concentration. But to calculate this stress based on linear elasticity theory is problematic. Linear elasticity theory predicts that stress at the tip of a sharp flaw is infinite in a linear elastic material. To avoid this problem, Griffith developed a fracture theory based on energy rather than on local stress. The creation of a new crack surface absorbs energy that is supplied from the work done by the external force - and the failure is promoted by a release of the stored strain energy in the solid material, which is sufficient to overcome the resistance to crack propagation. This energy per unit of newly created crack surface area defines an important parameter called the energy release rate (or strain energy release rate), denoted by G in honor of Griffith. In the later computational study in this dissertation, cracks are assumed to be initiated if the stress in the continuous mechanics framework is higher than the fracture strength that is obtained from experiments. The released energy is used to determine the crack propagation. G_c is defined as the critical value of energy released per unit length of crack extension. A crack is stable as long as G is smaller than G_c.

In 1957, Irwin [21] introduced the fundamental concept of the stress intensity factor, which is used to predict the stress state near the tip of a crack. In the theory of elasticity, the stress distribution near the crack tip at the polar coordinates (r, θ) (see figure 2.1) with the origin at the crack tip, has the form [22],

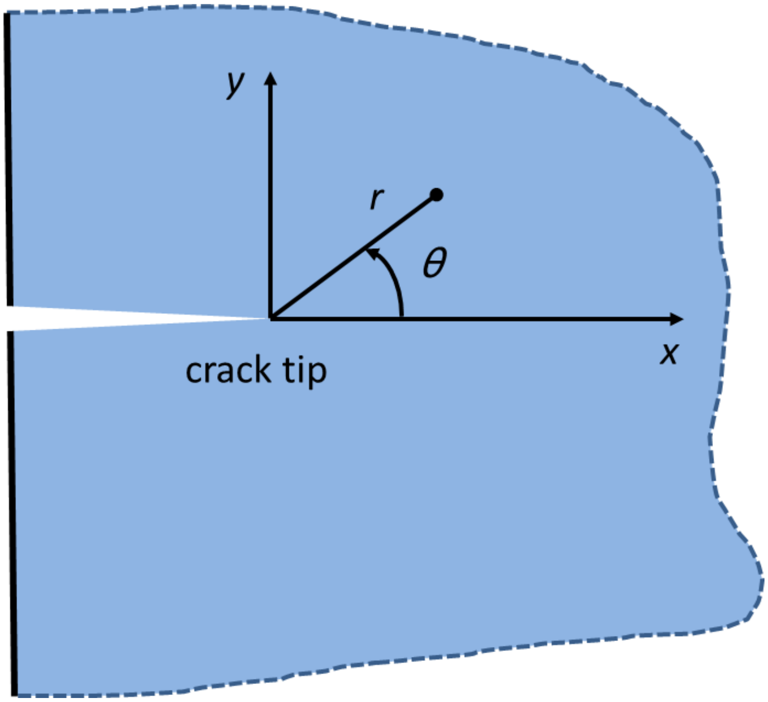

Figure 2.1: Polar coordinates at the crack tip.

$$\sigma_{ij}(r,\theta) = \frac{K}{\sqrt{2\pi r}} f(\theta) + \text{ higher order terms}, \tag{2.1}$$

where K is the stress intensity factor and $f(\theta)$ is a dimensionless function that depends on the load and the geometry.

Three linearly independent cracking modes - termed mode I, II and III, as illustrated in figure 2.2 - are employed to distinguish the different types of the crack-surface displacements in fracture mechanics. Three stress intensity factors (K_I, K_II, K_III) correspond to the three cracking modes, respectively. These factors are formally defined as [23]:

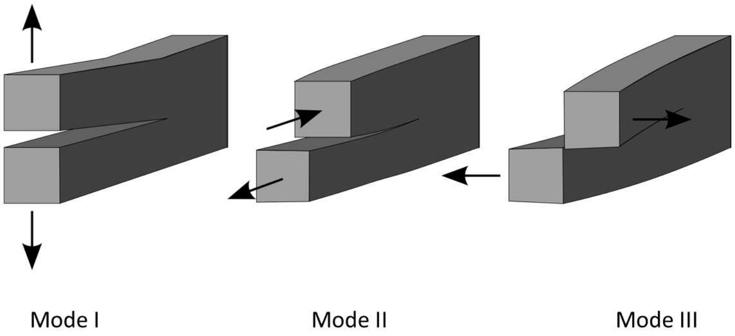

Figure 2.2: Illustration of three linearly independent cracking modes: mode I, opening; mode II, sliding; mode III, tearing.

$$K_{\mathrm{I}} = \lim_{r \to 0} \sqrt{2\pi r}\, \sigma_{yy}(r, 0), \tag{2.2}$$

$$K_{\mathrm{II}} = \lim_{r \to 0} \sqrt{2\pi r}\, \sigma_{yx}(r, 0), \tag{2.3}$$

$$K_{\mathrm{III}} = \lim_{r \to 0} \sqrt{2\pi r}\, \sigma_{yz}(r, 0), \tag{2.4}$$

where σ_{yy}, σ_{yx} and σ_{yz} are the corresponding stress components, respectively.

Just as the energy release rate G, the fracture criterion can be expressed in terms of the stress intensity factor. For a loading type of mode I, the crack will grow spontaneously when the stress intensity factor of mode I reaches its critical value. Accordingly, the stress intensity factors of modes II and III are applied for the corresponding loadings, respectively. The critical value of the stress intensity factor of mode I, K_{Ic}, is called fracture toughness as well, and it is one of the most important material properties for many design applications since most cracks tend to propagate in an opening mode.

Another significant achievement of Irwin is that he showed the relation between the energy release rate G and the stress intensity factor K in a linear elastic material:

$$G_{\mathrm{I}} = \frac{K_{\mathrm{I}}^2}{E'}, \tag{2.5}$$

$$G_{\mathrm{II}} = \frac{K_{\mathrm{II}}^2}{E'}, \tag{2.6}$$

$$G_{\mathrm{III}} = \frac{K_{\mathrm{III}}^2}{2\mu}, \tag{2.7}$$

where G_{I}, G_{II} and G_{III} are the energy release rates for mode I, mode II and mode III, respectively. E' is the effective Young's modulus, which equals to the Young's modulus, E, for plane stress and $E/(1-\nu^2)$ for plane strain, where ν is the Poisson's ratio. The shear modulus, μ, can be obtained by

$$\mu = \frac{E}{2(1+\nu)}. \tag{2.8}$$

In the mid-1960s, the concept of the J-integral was developed by James R. Rice [24]. For isotropic, linear elastic materials, the J-integral is equal to the energy release rate, which provides a way to evaluate the energy release rate for Griffith's theory. The J-integral is a contour integral around the crack tip, which is proven to be path independent in both linear elastic and non-linear elastic materials. Furthermore, the path independence of the J-integral rigorously holds in elasto-plastic materials when the monotonic loading is applied. The path independence of the J-integral avoids difficulties involved in computing the stress close to a crack in a nonlinear elastic or elasto-plastic material.

2.2 Weight function method

The weight function procedure was developed by Bückner [25] based on the superposition principle (or Bückner's principle). As long as the crack is closed, the stress intensity factor is zero - meaning that, effectively, there is no crack present. The zero stress intensity factor situation can be introduced by superposing the case of the cracked body with external loading minus the case of the same geometry of the cracked body, which is subjected to the reverse of the crack surface loading necessary to close the crack again, see figure 2.3. If a cracked body, which is subjected to an external loading at the boundary, has forces applied to the crack surfaces to close the crack, these forces must be equivalent to the stress distribution in an uncracked body of the same geometry subjected to the same external loading. As a result, the stress intensity factor in a cracked body can be calculated using the stress distribution in an uncracked body.

The weight function depends only on the geometry and boundary conditions of the cracked body.

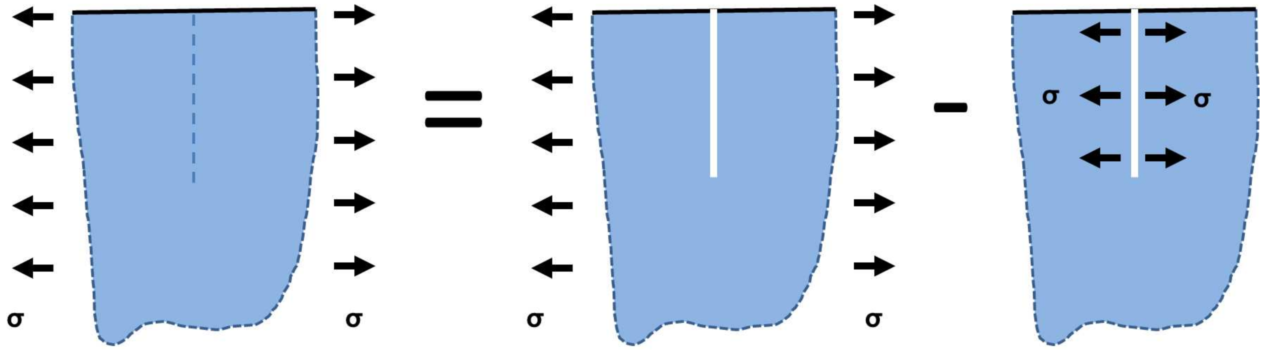

Figure 2.3: Illustration of the superposition principle used for the weight function method.

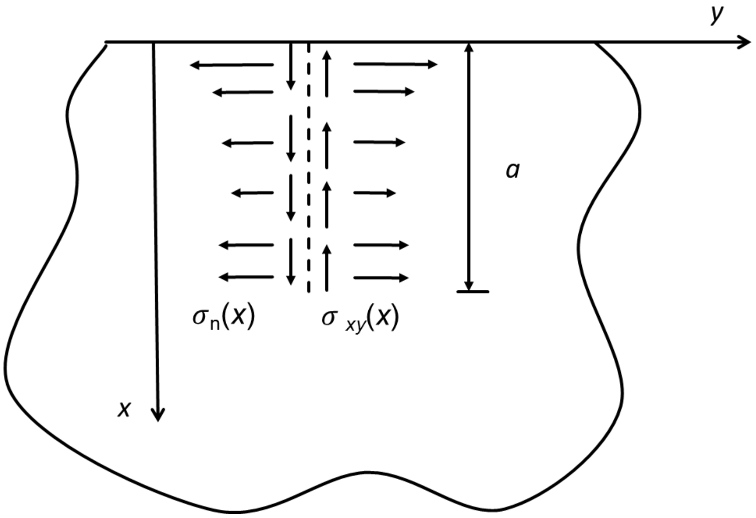

Figure 2.4: A prospective edge crack (dashed line) in a semi-infinite space.

Once the weight function is determined, the stress intensity factor for this geometry can be obtained for any stress distribution leading to a significantly simplified approach to determine stress intensity factors. The stress intensity factor for an edge crack in a semi-infinite space is shown here as an example. If $\sigma_\mathrm{n}(x)$ is the normal stress distribution, and $\sigma_{xy}(x)$ is the shear stress distribution in the uncracked domain along the prospective crack line of an edge crack, as shown in figure 2.4, the stress intensity factors are given by [26]

$$K_\mathrm{I} = \int_0^a [h_{11}(x,a)\sigma_\mathrm{n}(x) + h_{12}(x,a)\sigma_{xy}(x)]\mathrm{d}x, \tag{2.9}$$

$$K_{\mathrm{II}} = \int_0^a [h_{21}(x,a)\sigma_{\mathrm{n}}(x) + h_{22}(x,a)\sigma_{xy}(x)]\mathrm{d}x, \tag{2.10}$$

where h_{11}, h_{21}, h_{12}, h_{22} are the weight functions, and a is the crack length. In most practical cases, h_{21} and h_{12} disappear, and a simple form is obtained:

$$K_{\mathrm{I}} = \int_0^a h_{11}(x,a)\sigma_{\mathrm{n}}(x)\mathrm{d}x, \tag{2.11}$$

$$K_{\mathrm{II}} = \int_0^a h_{22}(x,a)\sigma_{xy}(x)\mathrm{d}x. \tag{2.12}$$

There are handbooks that list the according weight functions, derived analytically or numerically for cases of simple loading. The weight function $h(x,a)$ for edge cracks in a semi-infinite space with a normal stress distribution only along the prospective crack line is given by [27]

$$h(x,a) = \frac{2}{\sqrt{2\pi(a-x)}}[1 + M_1(1-\frac{x}{a})^{\frac{1}{2}} + M_2(1-\frac{x}{a})^1 + M_3(1-\frac{x}{a})^{\frac{3}{2}}], \tag{2.13}$$

where M_1 = 0.0719768, M_2 = 0.246984 and M_3 = 0.514465.

2.3 Computing J-integral and stress intensity factor [11]

2.3.1 J-integral

Under quasi-static conditions and in the absence of body forces, thermal strains and crack face traction, the path independent J-integral is written as follows [24]:

$$J = \lim_{\Gamma\to 0}\int_\Gamma [W\delta_{1i} - \sigma_{ij}\frac{\partial u_j}{\partial x_1}]n_i \mathrm{d}\Gamma, \tag{2.14}$$

where Γ is the contour surrounding a crack tip, n_i is the component of the outward normal unit vector, **n**, to Γ and W is the strain energy density. σ_{ij} and u_j denote the Cartesian components of the stress and displacement, respectively. x_1 is the Cartesian coordinate parallel to the crack and x_2 is the Cartesian coordinate perpendicular to the crack. Shih et al. extended the original contour integral formulation of the J-integral to the domain integral expression [28]. In the absence of body forces and crack face traction but in presence of thermal strains, this can be written as follows:

$$J = \int_A \{[\sigma_{ij}\frac{\partial u_j}{\partial x_1} - W\delta_{1i}]\frac{\partial q_1}{\partial x_1} + [\alpha\sigma_{ii}\frac{\partial \Delta T}{\partial x_1}]q_1\}\mathrm{d}A, \tag{2.15}$$

where A is the integration domain enclosed by the inner contour Γ, the outer contour C_{o} and the crack face contours C_+ and C_-, see figure 2.5. q_1 is any smooth function in A with a value ranging from zero on C_{o} to unity on γ. α is the coefficient of the thermal expansion and ΔT is the temperature change from a reference temperature. The domain A corresponds to the integration path of the contour integral form of the J-integral. When the domain A is discretized, the finite element formulation of the domain integral is written as follows:

$$J = \sum_{\text{all elements in } A} \sum_{p} \{[(\sigma_{ij}\frac{\partial u_j}{\partial x_1} - W\delta_{1i})\frac{\partial q_1}{\partial x_1} + (\alpha\sigma_{ii}\frac{\partial \Delta T}{\partial x_1})q_1]\mathrm{det}(\frac{\partial x_k}{\partial \eta_k})\}_p w_p, \tag{2.16}$$

where p is the number of Gauss points in each element. The quantities within $\{\}_p$ are evaluated at all gauss points in an element and w_p are the respective weights. $\partial x_k/\partial \eta_k$ is the Jacobian matrix of the coordinate transformation [28].

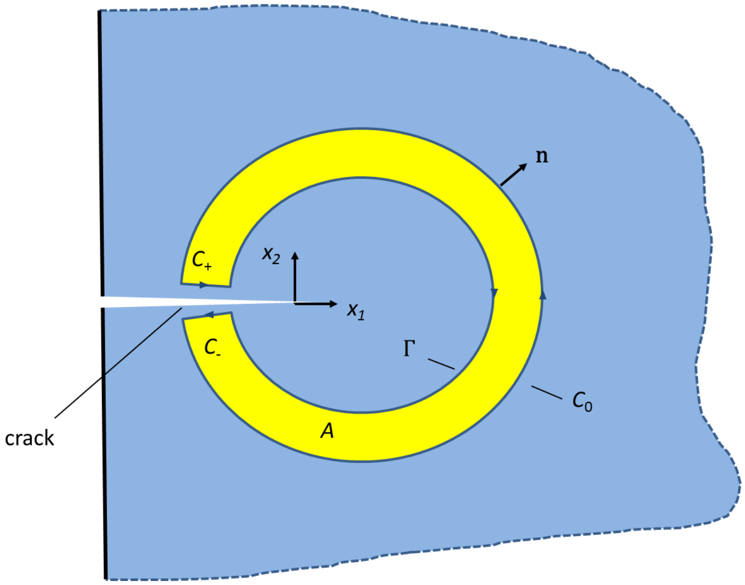

Figure 2.5: Schematic diagram for the domain integral concept to compute the J-integral of a crack.

The aforementioned definitions of the J-integral will lead to a path dependent value in a residual stress field, since the residual stress field is a self-balancing stress distribution resulting from internal strains. Such residual stress problems can then be treated as initial strain problems [29]. If the total strain is written as the sum of the mechanical strain, ε^{m} , and the initial strain, ε^0 ; i.e.,

$$\varepsilon = \varepsilon^{\mathrm{m}} + \varepsilon^{0}, \tag{2.17}$$

the path-independent J-integral in the presence of a residual stress field is given by [29]

$$J = \int_A \{[\sigma_{ij}\frac{\partial u_j}{\partial x_1} - W\delta_{1i}]\frac{\partial q_1}{\partial x_1} + \sigma_{ij}\frac{\partial \varepsilon^0_{ij}}{\partial x_1}q_1\}\mathrm{d}A, \tag{2.18}$$

where W is defined as the mechanical strain energy density:

$$W = \int_0^{\varepsilon^{\mathrm{m}}} \boldsymbol{\sigma} : \mathrm{d}\varepsilon^{\mathrm{m}}. \tag{2.19}$$

where $\boldsymbol{\sigma}$ is the stress tensor. The initial strain ε^0 remains constant during the entire deformation. Within the finite element framework, the J-integral expression is given by [29]

$$J = \sum_{\text{all elements in } A} \sum_p \{[(\sigma_{ij}\frac{\partial u_j}{\partial x_1} - W\delta_{1i})\frac{\partial q_1}{\partial x_1} + \sigma_{ij}\frac{\partial \varepsilon^0_{ij}}{\partial x_1}q_1]\mathrm{det}(\frac{\partial x_k}{\partial \eta_k})\}_p w_p. \tag{2.20}$$

2.3.2 Stress intensity factor

In ABAQUS, stress intensity factors are calculated based on the interaction integral method, which is an effective tool for calculating mixed-mode fracture parameters in homogeneous materials [30]. In general, the J-integral for a given problem can be written as

$$J = \frac{1}{8\pi}[K_{\mathrm{I}}B^{-1}_{11}K_{\mathrm{I}} + 2K_{\mathrm{I}}B^{-1}_{12}K_{\mathrm{II}} + 2K_{\mathrm{I}}B^{-1}_{13}K_{\mathrm{III}} + (\text{terms not involving } K_{\mathrm{I}})], \tag{2.21}$$

where **B** is the pre-logarithmic energy factor matrix. For an auxiliary and pure mode I specific crack tip field, the J-integral is defined by stress intensity factor k_{I} as

$$J^{\mathrm{I}}_{\mathrm{aux}} = \frac{1}{8\pi}k_{\mathrm{I}} \cdot B^{-1}_{11} \cdot k_{\mathrm{I}}. \tag{2.22}$$

Superimposing the auxiliary field onto the actual field yields

$$\begin{aligned} J^{\mathrm{I}}_{\mathrm{tot}} = \frac{1}{8\pi}[(K_{\mathrm{I}}+k_{\mathrm{I}})B^{-1}_{11}(K_{\mathrm{I}}+k_{\mathrm{I}}) + 2(K_{\mathrm{I}}+k_{\mathrm{I}})B^{-1}_{12}K_{\mathrm{II}} + 2(K_{\mathrm{I}}+k_{\mathrm{I}})B^{-1}_{13}K_{\mathrm{III}} \\ +(\text{terms not involving } K_{\mathrm{I}} \text{ or } k_{\mathrm{I}})]. \end{aligned} \tag{2.23}$$

Since the terms that do not involve K_{I} or k_{I} are identical in $J^{\mathrm{I}}_{\mathrm{tot}}$ and J, the interaction integral can be defined as

$$J^{\mathrm{I}}_{\mathrm{int}} = J^{\mathrm{I}}_{\mathrm{tot}} - J - J^{\mathrm{I}}_{\mathrm{aux}} = \frac{k_{\mathrm{I}}}{4\pi}[B^{-1}_{11}K_{\mathrm{I}} + B^{-1}_{12}K_{\mathrm{II}} + B^{-1}_{13}K_{\mathrm{III}}]. \tag{2.24}$$

If the calculations are repeated for mode II and mode III, a system of linear equations is obtained:

$$J^{\alpha}_{\mathrm{int}} = \frac{k_{\alpha}}{4\pi}B^{-1}_{\alpha\beta}K_{\beta}, \tag{2.25}$$

where α and β represent the index of I, II and III. No summation is made on α = I, II, III. I, II and III correspond to 1,2 and 3 when indicating the components of **B**.
If k_{α} are assigned the value 1, the solution of the above equations leads to

$$\boldsymbol{K} = 4\pi\mathbf{B}\cdot\boldsymbol{J}_{\mathbf{int}}, \tag{2.26}$$

where $\boldsymbol{J}_{\mathbf{int}} = [J^{\mathrm{I}}_{\mathrm{int}}, J^{\mathrm{II}}_{\mathrm{int}}, J^{\mathrm{III}}_{\mathrm{int}}]^T$. Based on the definition of the J-integral, the interaction integrals $J^{\alpha}_{\mathrm{int}}$ can be expressed as

$$J^{\alpha}_{\mathrm{int}} = \lim_{\Gamma\to 0}\int_{\Gamma}\mathbf{n}\cdot(\boldsymbol{\sigma}:\varepsilon^{\alpha}_{\mathrm{aux}}\mathbf{I} - \boldsymbol{\sigma}\cdot(\frac{\partial\mathbf{u}}{\partial\mathbf{x}})^{\alpha}_{\mathrm{aux}} - \sigma^{\alpha}_{\mathrm{aux}}\cdot\frac{\partial\mathbf{u}}{\partial\mathbf{x}})\cdot\mathbf{q}\,\mathrm{d}\Gamma, \tag{2.27}$$

where **I** is the identity matrix, **u** is the displacement vector, **x** is the coordinate vector and **q** is referred to as the crack-extension vector. The subscript aux represents three auxiliary pure mode I, mode II and mode III crack tip fields for α = I, II, III, respectively.

2.4 Extended finite element method

2.4.1 Discontinuity modeling

The extended finite element method developed by Belytschko and Black [31] is a method whereby crack initiation and growth can be modelled by the finite element method without remeshing. The essential idea of this method is to introduce enrichment functions to describe a discontinuous displacement field. It is an extension of the conventional finite element method based on the concept of partition of unity by Melenk and Babuska [32], which allows local enrichment functions to be easily incorporated into a finite element approximation. The presence of discontinuities is ensured by the special enriched functions in conjunction with additional degrees of freedom.
XFEM is implemented in ABAQUS from version 6.9 onwards. For the purpose of a fracture mechanics analysis, the enrichment functions typically consist of the near-tip asymptotic functions that

capture the singularity around the crack tip and a discontinuous function that represents the jump in displacement across the crack surfaces, see figure 2.6.

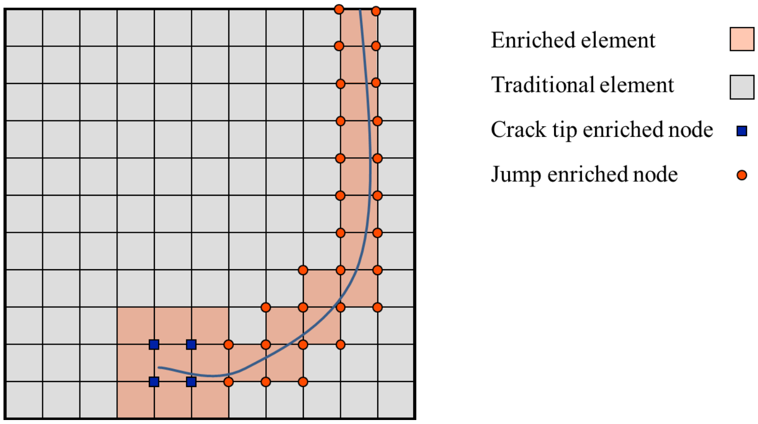

Figure 2.6: The enriching strategy near the crack. The crack tip enriched nodes for which the closure of the nodal support contains the crack tip are enriched with near-tip asymptotic functions. The jump enriched nodes whose support is intersected by the crack (excluding crack tip enriched nodes) are enriched with a discontinuous function.

In order to describe the geometry of discontinuities, the level-set method is used in the context of XFEM. This method was originally introduced by Osher and Sethian [33] for tracking the evolution of moving boundaries. In this method, the discontinuity is represented as the zero level-set of a function. Thus, the domain is divided into two subdomains on either side of the discontinuity where the level-set function is positive or negative, respectively. The method was then extended for tracking the evolution of open segments by Stolarska [34] in such a way that the evolution of a crack can be tracked by two orthogonal level-set functions, namely, $\Psi(\mathbf{x})$ and $\Phi(\mathbf{x})$. An endpoint of the crack is represented as the intersection of the zero level-set of $\Psi_i(\mathbf{x})$ with an orthogonal zero level-set of the function $\Phi_i(\mathbf{x})$, where i is the number of tips on a given crack. The initial level-set functions, $\Psi(\mathbf{x})$ and $\Phi(\mathbf{x})$, and the representation of the crack are shown in figure 2.7.

The approximation for a displacement vector function $\mathbf{u}$ with the partition of unity enrichment is given [35] as

$$\mathbf{u} = \sum_{i \in I_{\text{all}}} N_i(\mathbf{x})\mathbf{u}_i + \sum_{i \in I_{\text{Heaviside}}} N_i(\mathbf{x})H(\mathbf{x})\mathbf{a}_i + \sum_{i \in I_{\text{tip}}} N_i(\mathbf{x}) \sum_{\alpha=1}^{4} F_\alpha(\mathbf{x})\mathbf{b}_i^\alpha, \tag{2.28}$$

where $N_i(\mathbf{x})$ are the nodal shape functions in the conventional FEM. I_{all}, $I_{\text{Heaviside}}$ and I_{tip} are the set of nodal indices of the classical finite element method, the set of node indices associated with crack separation away from the crack tip and the set of node indices around crack tip, respectively. $\mathbf{u}_i$ is the nodal displacement vector associated with the continuous part of the FEM solution. $\mathbf{a}_i$ is the nodal enriched degree of freedom vector, and $H(\mathbf{x})$ is the associated discontinuous jump function

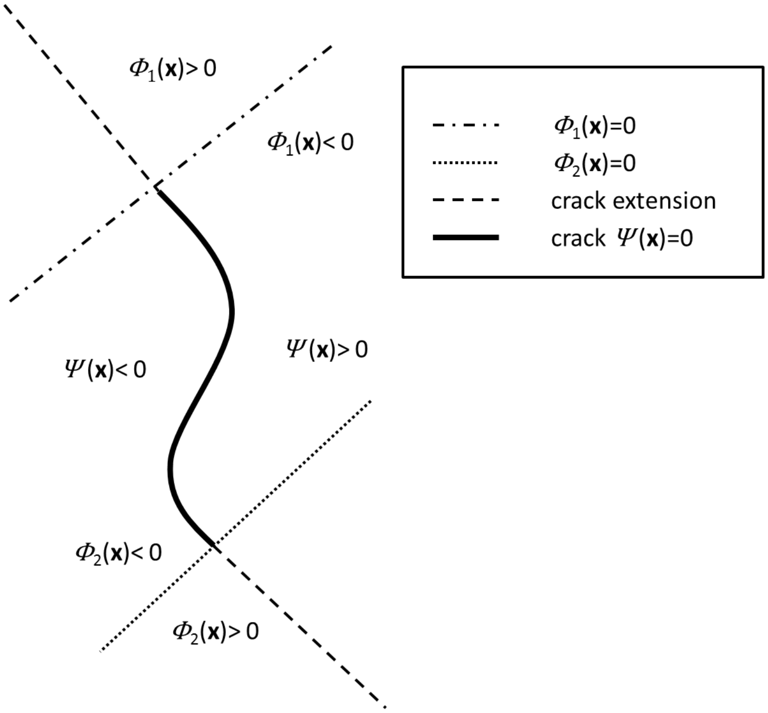

Figure 2.7: Construction of initial level-set functions. $\Psi(\mathbf{x})$ is used to divide the domain into two subdomains on either side of crack, where $\Psi(\mathbf{x})$ is positive or negative. $\Phi(\mathbf{x})$ is applied to divide the domain into subdomains that is in front of or behind crack tip, where $\Phi(\mathbf{x})$ is positive or negative.

across the crack surfaces, which is given by the form of a generalized Heaviside function,

$$H(\mathbf{x}) = \begin{cases} 1, & \Psi(\mathbf{x}) > 0, \\ -1, & \Psi(\mathbf{x}) < 0. \end{cases} \tag{2.29}$$

$\mathbf{b}_i^\alpha$ is the nodal enriched degree of freedom vector associated with near-tip displacement, and the associated elastic asymptotic crack tip functions $F_\alpha(\mathbf{x})$ given by

$$\{F_\alpha(\mathbf{x})\}_{\alpha=1,2,3,4} = \{\sqrt{r}\sin\frac{\theta}{2}, \sqrt{r}\cos\frac{\theta}{2}, \sqrt{r}\sin\theta\sin\frac{\theta}{2}, \sqrt{r}\sin\theta\cos\frac{\theta}{2}\}, \tag{2.30}$$

where $(r(\mathbf{x}), \theta(\mathbf{x}))$ is a polar coordinate system with its origin at the crack tip and $\theta(\mathbf{x}) = 0$ is tangent to the crack at the tip, see figure 2.1.

The asymptotic singularity functions are only considered for stationary cracks in ABAQUS [11]. To model progressive cracks, the XFEM-based cohesive segments method and phantom nodes, which will be introduced later, are used. The XFEM-based cohesive segments method has a very general modeling capability and can be used for modeling brittle or ductile fracture. With XFEM it is able to simulate crack initiation and propagation along an arbitrary, solution-dependent path in the bulk materials, since crack propagation is not tied to the element boundaries in a mesh. In this case, the near-tip asymptotic singularity is not needed, and only the displacement jump across a cracked element is considered. Therefore, the crack has to propagate across an entire element at a time to avoid the necessity of modeling the stress singularity.

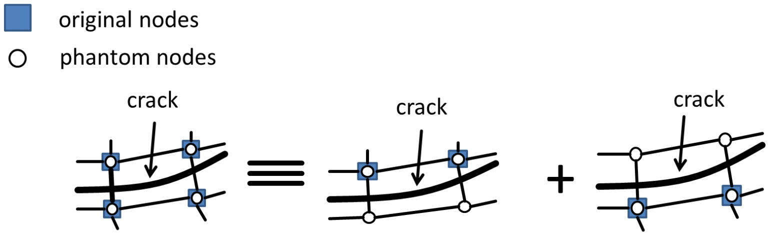

Figure 2.8: The principle of the phantom node method. Phantom nodes are superposed on the original real nodes. If the element is cut through by a crack into two parts, each part is formed by a combination of some real and phantom nodes depending on the orientation of the crack.

Phantom nodes, which are superposed on the original real nodes, are introduced to represent the discontinuity of the cracked elements, as illustrated in figure 2.8. As long as the element is intact, each phantom node is completely constrained to its corresponding real node. If the element is cut through by a crack, the cracked element splits into two parts. Each part is formed by a combination of some real and phantom nodes depending on the orientation of the crack. Each phantom node and its corresponding real node are no longer tied together and can move apart. The magnitude of the separation is governed by the cohesive law until the cohesive stiffness of the cracked element is zero, after which the phantom and the real nodes move independently.

In ABAQUS, an enriched feature is defined as a domain where crack may occur. One or multiple pre-existing cracks can be associated with an enriched feature and initiated in an enriched feature without any initial defects. However, multiple cracks can nucleate in a single enriched feature only when the damage initiation criterion is satisfied in multiple elements in the same time increment. Otherwise, additional cracks will not nucleate until all the pre-existing cracks in an enriched feature have propagated through the boundary of the given enriched feature. If nucleation of multiple cracks is expected to occur at different locations sequentially during an analysis, multiple enriched features should be specified in the model.

2.4.2 Damage modeling

Crack initiation refers to the beginning of a degradation of the cohesive response in an enriched element. The process of degradation begins when the stresses or the strains satisfy specified crack initiation criteria. Crack initiation criteria are available based on the following ABAQUS built-in models [11]:

- the maximum principal stress criterion,
- the maximum principal strain criterion,
- the maximum nominal stress criterion,
- the maximum nominal strain criterion.

In this dissertation, the maximum principal stress (MPS) criterion is applied. When the criterion is satisfied,

$$\langle \sigma_{\text{max}} \rangle \geq \sigma^0_{\text{max}}, \tag{2.31}$$

where σ^0_{max} represents the maximum allowable principal stress, the resulting crack is always orthogonal to the maximum principal stress direction. The symbol $\langle\rangle$ represents the Macaulay bracket with the usual interpretation (i.e., $\langle \sigma_{\text{max}} \rangle$ = 0 if $\sigma_{\text{max}} < 0$, and $\langle \sigma_{\text{max}} \rangle$ = σ_{max} if $\sigma_{\text{max}} \geq 0$). The enriched elements do not, therefore, undergo damage under pure compression.

The cohesive material behavior is applied to the cracked domain in XFEM simulations. The elastic behavior is written in terms of an elastic constitutive matrix that relates the normal and shear stresses to the normal and shear separations of a cracked element. The elastic behavior can then be written as

$$\mathbf{t} = \left\{ \begin{array}{c} t_n \\ t_s \\ t_t \end{array} \right\} = \left[\begin{array}{ccc} K_{nn} & 0 & 0 \\ 0 & K_{ss} & 0 \\ 0 & 0 & K_{tt} \end{array} \right] \left\{ \begin{array}{c} \delta_n \\ \delta_s \\ \delta_t \end{array} \right\} = \mathbf{K}\boldsymbol{\delta}, \tag{2.32}$$

where the nominal traction stress vector, **t**, consists of the components: t_n, t_s and (in three-dimensional problems) t_t, which represent the normal and the two shear tractions, respectively. δ_n, δ_s, and δ_t denote the corresponding separations. The terms K_{nn}, K_{ss} and K_{tt} are stiffnesses calculated for an enriched element based on the elastic properties.

The normal and tangential stiffness components will not be coupled, since pure normal separation by itself does not give rise to cohesive forces in the shear directions, and pure shear slip with zero normal separation does not give rise to any cohesive forces in the normal direction. Once a damage initiation criterion is met, damage can occur according to a user-defined damage evolution law, as shown in figure 2.9.

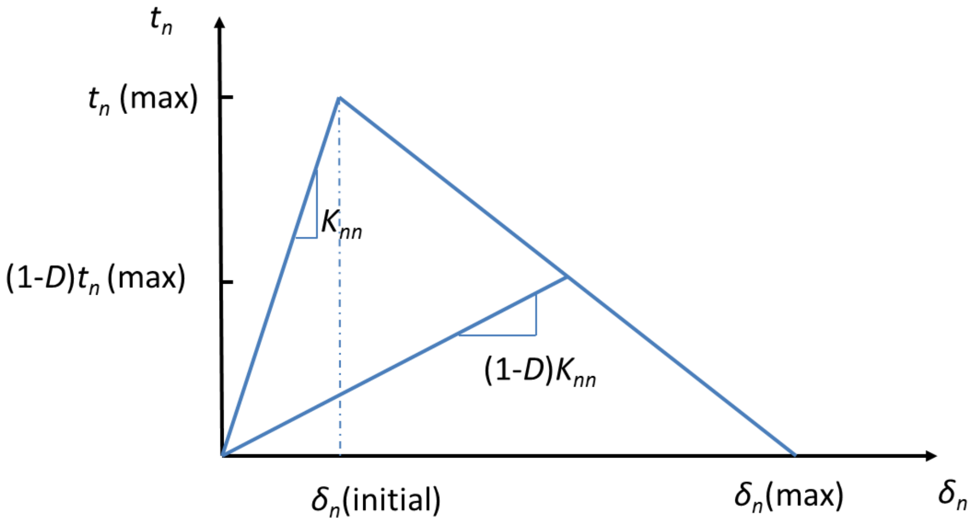

Figure 2.9: Linear traction-separation response with a failure mechanism. As a scalar damage variable, D represents the averaged overall damage. Its initial value is 0. If a crack is initiated, D monotonically evolves from 0 to 1 upon further loading. When the energy dissipation associated with the crack extension equals the fracture energy, the crack is fully opened, and D is equal to 1.

Chapter 3

Fracture mechanics analysis of tungsten under short transient thermal loads by ELMs

3.1 Edge localized modes

Fortunately, it was discovered during the ASDEX tokamak experiments at Max Planck Institute for Plasma Physics in Garching, Germany, that certain conditions during the application of neutral beam injection heating lead to a transition to a high confinement mode (H-mode) [36]. The plasma energy confinement time of the H-mode is nearly twice that of the low confinement mode (L-mode). This discovery is to be seen as an important step to reaching higher temperatures and pressures in tokamaks. Today, almost all tokamaks, including the tokamaks in ITER and DEMO, are designed to operate in H-mode. However, in addition to the increase in confinement time, a new type of instability, called edge localized mode (ELM), was found. As a consequence of the ELM instability, a steep plasma pressure gradient is formed at the edge of the plasma. Figure 3.1 shows the magnetic geometry of a divertor tokamak and pressure profiles of L- and H-mode plasmas. The plasma pressure profile at the plasma edge relaxes periodically towards less steep slopes (ELM crash). Then, it steepens again before collapsing at the following ELM (ELM recovery). As a consequence, energy and particles are released into the Scrape-Off-Layer (SOL) in a very short timescale, <1 ms [37]. In a standard H-mode plasma, ELMs occur repetitively, and the energy lost from inside the separatrix that flows along field lines into the divertor results in an ELM heat flux pulse. Regarding the heating power dependence of the ELM frequency and the theoretical peeling-ballooning stability limit, three types of ELMs (type-I, type-II and type-III) were classified and are commonly accepted [37]. Of the three modes, the type I ELMs can cause the most significant damage in PFMs. Although several methods (e.g. radiating divertors [38], magnetic triggering [39], pellet pace-making of ELMs [40], edge ergodisation [41, 42]) have been applied to control ELMs, some unexpected ELMs can still occur. The maximum energy density on the divertor target for the controlled ELMs is 0.5 MJ/m^2 in the inner plate and 0.3 MJ/m^2 in the outer plate [43]. The maximum energy density on the divertor target for uncontrolled ELMs is 10 MJ/m^2 in the inner plate and 6 MJ/m^2 in the outer plate [43]. The erosion threshold corresponds to energy densities in the range of 0.7-1.0 MJ/m^2, while for energy densities of $\sim$0.5 MJ/m^2 erosion-effects are found to be negligible [44]. The energy density for the uncontrolled ELMs is much higher than the erosion threshold for PFCs and will result in the reduction of the divertor lifetime to few full performance discharges in ITER [45]. Therefore, the strategy is to find mitigation or suppression solutions for uncontrolled ELMs and to develop or enhance materials for the PFC for controlled ELMs. This chapter focuses on a fracture mechanics analysis of tungsten under short transient thermal loadings for controlled ELMs.

There are plenty of experimental reports on the detrimental impact of ELM-like thermal transients on the microstructural integrity of tungsten-based materials [46–50]. However, one finds only few computational studies on this topic. An analytical modeling was carried out for tungsten surface cracking under the action of the thermal stress arising in the thin resolidified surface layer induced by thermal shocks [51]. Hirai and Pintsuk [52] studied thermo-mechanical behavior of tungsten under thermal shocks by means of finite element calculations. To the author's knowledge, numerical fracture mechanics analyses focusing on cracking induced by residual stress resulting from the ELMs appear to be lacking.

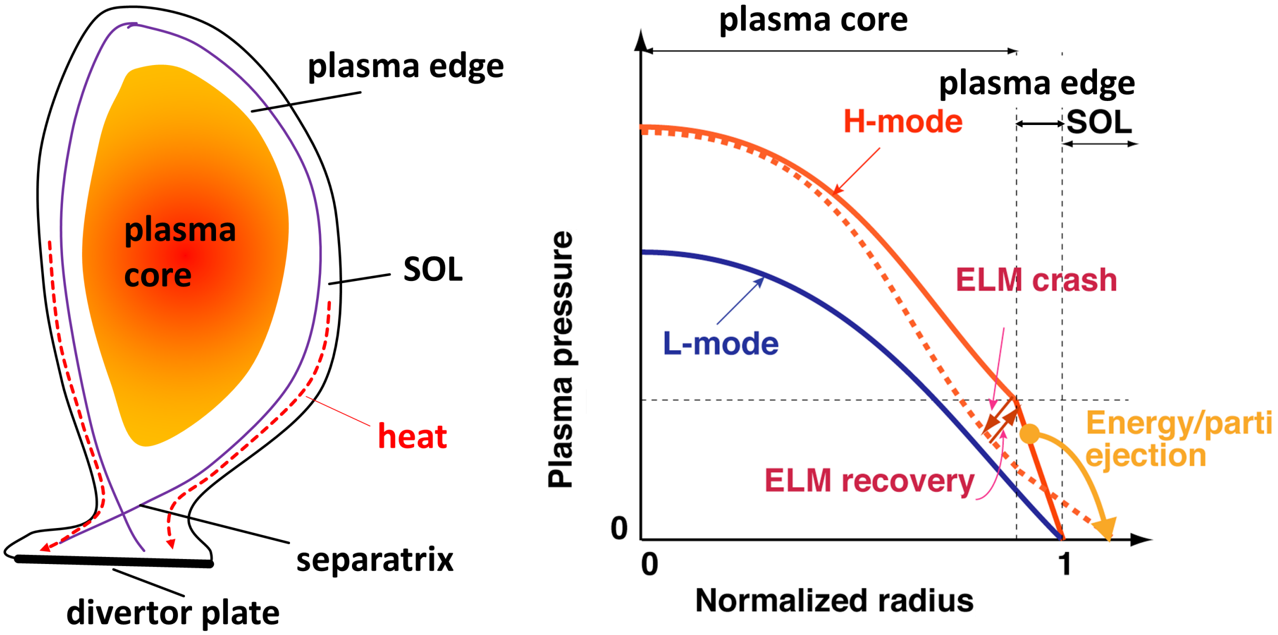

Figure 3.1: The magnetic geometry of a divertor tokamak (left) and pressure profiles of L- and H-mode plasmas as a function of normalized radius for the different confinement regimes (right, adapted from [53]). In H-mode, the periodical ELM crash and recovery lead to energy ejection in the Scrape-Off-Layer (SOL), where the thermal energy flows along the open field lines to divertor targets.

3.2 Review of experimental results

To mimic the ELM-like transient thermal loads, thermal shock experiments were performed frequently with an electron beam test facility. The advantages of an electron beam test facility are the flexible operation time (pulse length, 1 ms up to continuous work) and homogeneous heat loading on large areas. A number of electron beam test facilities have been constructed [4], such as JUDITH at Forschungszentrum Jülich (Germany), JEBIS, OHBIS at Japan Atomic Energy Research Institute (Japan), ACT at National Institute for Fusion Science (Japan), EBHT at Kyushu University (Japan), FE200 at French Alternative Energies and Atomic Energy Commission (France), TSEFFY at Efremov Institute (Russia), EB1200 at Sandia National Laboratories (USA) and an electron beam test facility at Southwestern Institute of Physics (China). In this chapter, the fracture analysis is based on the setup of the thermal shock experiments with JUDITH at Forschungszentrum Jülich.

The electron beam test facility JUDITH (Jülich Divertor Test Equipment in Hot Cells) located at the Hot Cells Laboratory of the Forschungszentrum Jülich [54] consists of an electron beam unit with a beam power of 60 kW, a stainless steel vacuum chamber of $800 \times 600 \times 900\,\mathrm{mm}^3$ and a number of diagnostic devices. The electron gun is placed on the top of the vacuum chamber, and the beam is discharged downward to the surface of the test sample. The focused electron beam with a diameter of 1 mm and typical energies of 120 keV can be swept across the surface of the test sample in two directions at frequencies of up to 100 kHz.

At Forschungszentrum Jülich, several thermal shock experiments were performed on a number of different tungsten grades. The thermal shock experiments employed power densities of 0.15-1.3 $\mathrm{GW/m}^2$ to simulate ELM transient thermal loads. The base temperature, to which the samples were preheated before the experiments, was adjusted between room temperature and 800 °C. The ITER reference tungsten grade was tested in the course of a cracking failure study under a single thermal shock [46]. Microstructures of the testing samples were observed for different power densities and base temperatures, see figure 3.3. In addition to micro-cracks, macro-cracks surrounding the loading area were found for the recrystallized sintered tungsten [55], see figure 3.4. A thermal shock characterization of tungsten that was forged in two orthogonal directions was made under thermal shocks [47, 56], where cracking thresholds were investigated for tungsten under thermal shock loads at different base temperatures, as shown in figure 3.5. The performance of different tungsten grades (e.g. ultra-high purity tungsten (W-UHP), tungsten alloys containing 1 (WTa1) and 5 (WTa5) mass % tantalum) was studied in [48, 49]. Although the experiments were performed with different tungsten grades, two common features were observed. First, cracks are related to the brittleness of tungsten at low temperatures. Cracking thresholds show that surface modification occurs instead of cracking, the higher the applied base temperature is. Second, cracks are in general perpendicular to the loading surface, while crack formation parallel to the loading surface is found at a certain distance from the surface (200-600 μm), which is observed in cross-sections of the samples [47, 48], see figures 3.6 and 3.7.

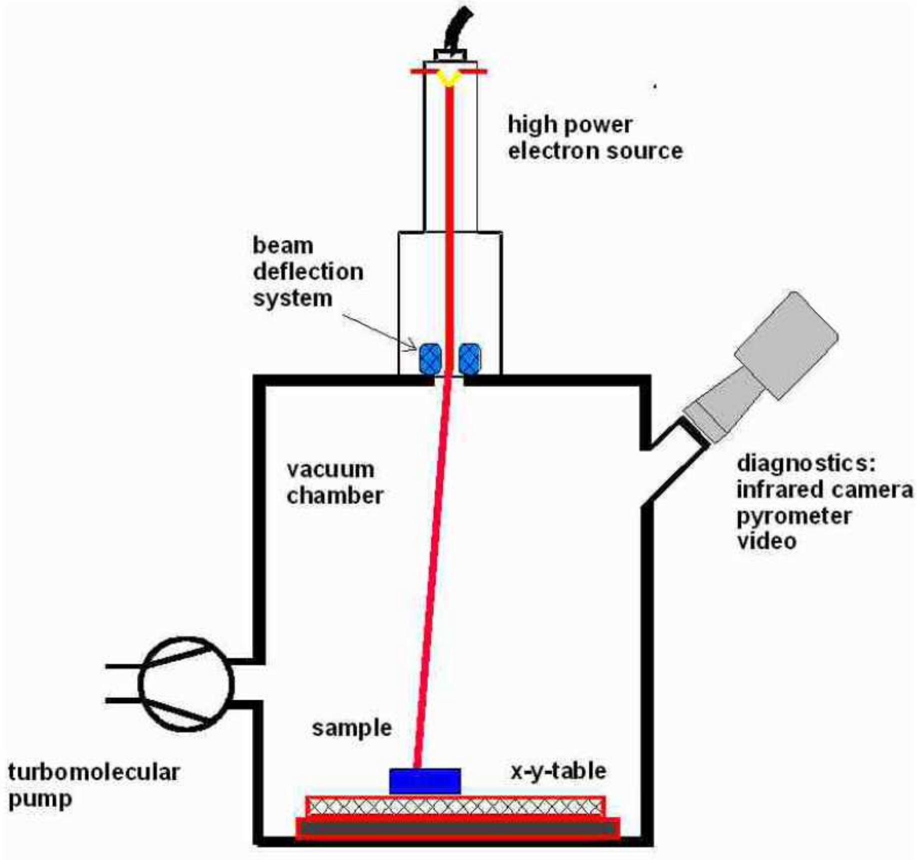

Figure 3.2: Electron beam test facility working principle [5].

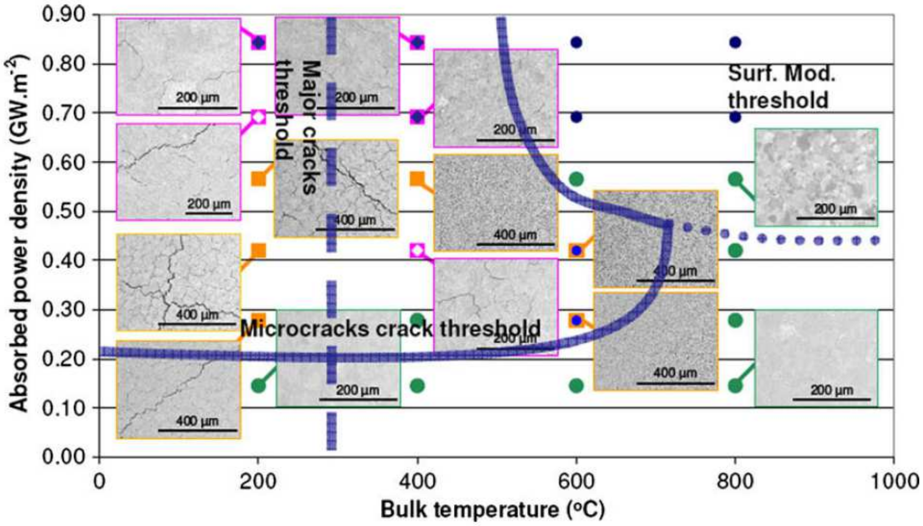

Figure 3.3: Microstructures in a diagram of power density as a function of bulk temperature (base temperature). The pulse duration is 5 ms. The solid line indicates the boundary of micro-crack occurrence, the dashed line represents the threshold of major crack (macro-crack) generation, and the dotted line indicates the threshold of surface modification [46].

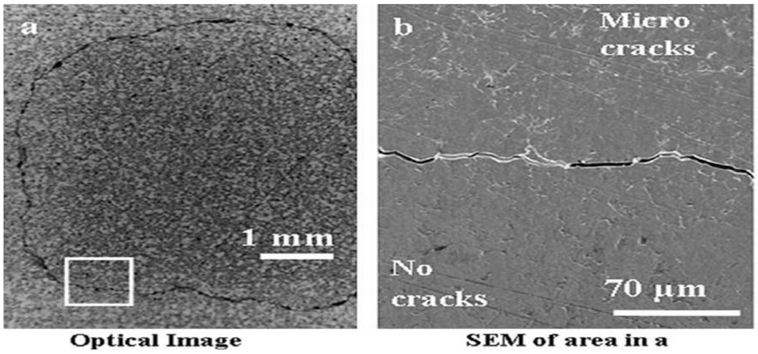

Figure 3.4: Surface morphology (a) and microstructures (b) of loaded areas of recrystallized sintered tungsten by a single pulse of 0.55 GW/m^2 for 5 ms [55] (base temperature = room temperature).

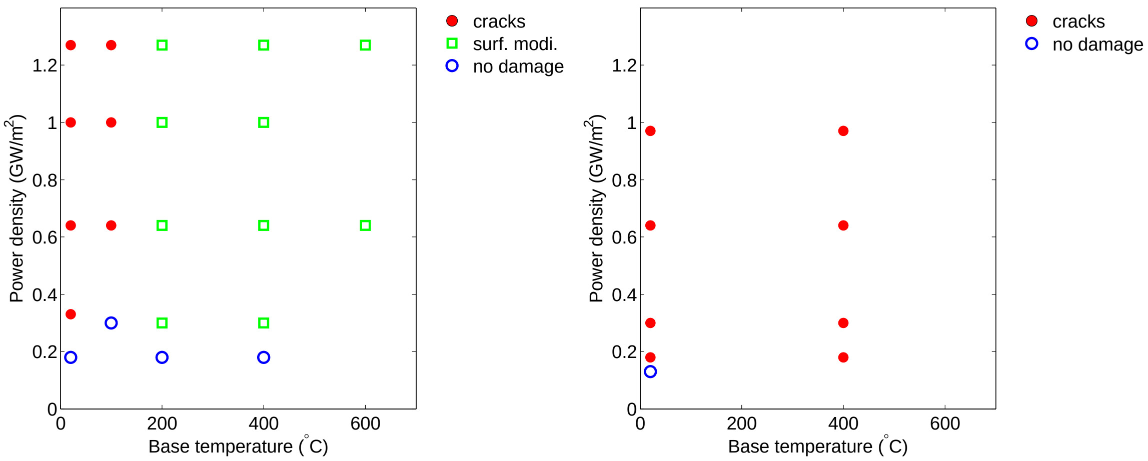

Figure 3.5: Thermal shock behavior of pure tungsten in reference (left) and orthogonal (right) directions for 100 cycles with a pulse duration of 1 ms, replotted based on the data listed in [56]. The reference direction is parallel to the preferential orientation of the grains, and the orthogonal direction is orthogonal to the preferential orientation of the grains.

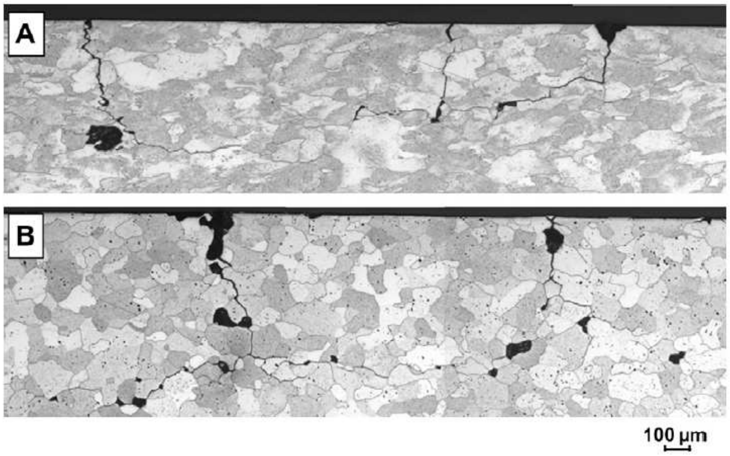

Figure 3.6: Light microscopic (LM) images of the materials crack patterns under 100 thermal shocks with a pulse duration of 1 ms [47], A: stress relieved tungsten and B: the recrystallized tungsten. Power density = 1.3 GW/m^2, base temperature = room temperature.

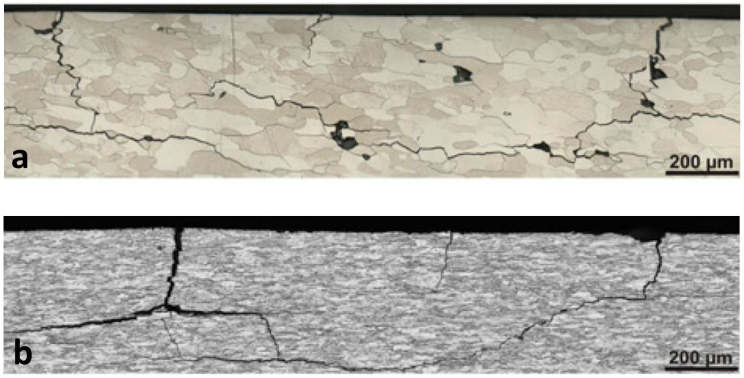

Figure 3.7: Crack patterns at cross-section of W-UHP (a) and WTa5 (b) under 100 thermal shocks with a pulse duration of 1 ms [48]. Power density = 1.27 GW/m^2, base temperature = room temperature.

3.3 Materials

The calculations in this chapter were performed in a continuum mechanics framework, and the material was assumed to be homogeneous and isotropic for simplicity. It should be noted that industrially manufactured tungsten products often show significant anisotropy in material properties due to strongly textured microstructure produced by rolling. Isotropic material properties may be achieved by specific production methods such as powder injection molding. During the thermal shock experiments, the tungsten samples were subjected to a wide range of temperatures - from room temperature to the material's melting point. It is therefore essential to choose the appropriate material data to cover the whole temperature range. The thermal material parameters of tungsten, such as thermal conductivity, coefficient of thermal expansion and specific heat, as well as its mechanical material parameters, such as Young's modulus and yield stress, used in this chapter refer to the temperature dependent data presented in literature sources [7, 8]. The thermal and mechanical material parameters of tungsten at selected temperatures are listed in tables 3.1 and 3.2.

Table 3.1: Thermal material parameters of tungsten at selected temperatures [7].

Temperature (°C)	Thermal conductivity (W/mK)	Density (kg/m^3)	Specific heat (J/kgK)	Coefficient of thermal expansion (10^{-6}/K)
27	176	19299	133	4.74
927	114	19051	155	5.06
1927	99	18725	180	6.77
2727	92	18379	218	9.19

Table 3.2: Mechanical material parameters of tungsten at selected temperatures [8].

Temperature (°C)	Young's modulus (GPa)	Yield stress (MPa)
20	399	infinite[a]
200	391	1221
600	375	724
1000	356	467
1600	321	64
2000	278	42

[a] No value is reported in [8]. Here, it is assumed that tungsten behaves purely elastic at this temperature.

The values of the yield stress and the ultimate tensile strength of tungsten are nearly equivalent at the same temperature [8]. Therefore, tungsten is assumed to behave elastic-ideally plastic in the simulations conducted in this chapter.

3.4 Simplified analytical solution

Numerical methods, such as the finite element method, are widely used in many engineering fields to capture the complex geometrical and loading conditions. However, an analytical solution can provide a deeper understanding of the key physical features - and under certain conditions, the analytical approach can even provide quantitative predictions. In this part, a simplified analytical solution is derived to estimate the temperature, strain and stress responses of tungsten to homogeneous thermal loadings.

3.4.1 Temperature calculation

By means of fast scanning of the sample surface with the electron beam, an almost homogeneous ELM-like transient thermal loading was achieved at the top surface of the tungsten samples [47]. Due to the homogeneity of the thermal loading, the heat conduction in the central part of the loading area can be assumed to occur only in depth direction.

The energy input induced by the ELMs is much larger than the energy loss due to radiation. When the thermal loading stops, the decrease of temperature in the surface layer of the tungsten is dominated by heat conduction rather than thermal radiation at the surface. As a result, the radiation effect can be neglected in the temperature calculation.

In thermal shock experiments, the thermal penetration depth, beyond which the temperature of the solid is not affected by the surface temperature, can be calculated as follows [57],

$$d_{\text{pen}} = \sqrt{8\frac{k}{\rho c}t}, \tag{3.1}$$

where d_{pen} is the thermal penetration depth, k is the thermal conductivity, ρ is the density, c is the specific heat, and t denotes time.

Calculations based on the thermal simulations using FEM showed that the surface temperature dropped below DBTT for typical loading conditions within 5 ms, which indicates that if the temperature at the bottom of the sample is not affected by the surface temperature within 5 ms, the cooling devices do not play an important role for the temperature evolution at the surface. Substituting the thermal properties listed in table 3.1 into equation (3.1), d_{pen} at t = 5 ms is smaller than the sample thickness (5 mm). Based on this result, the heat transfer between the bottom of the sample and the cooling device can be neglected in a rough temperature calculation.

Considering the above reasons, the solution of a semi-infinite surface heat transfer problem without considering the radiation effect can provide a fair estimate of the temperature in the central part of the loading area in thermal shock experiments at Forschungszentrum Jülich. H. S. Carslaw and J. C. Jaeger [58] gave a solution for the temperature of a semi-infinite solid for a heat flux at $x = 0$ in a prescribed time with zero initial temperature as follows:

(i) $0< \ t \ \leq t_{\mathrm{h}}$

$$T - T_0 = \frac{2q}{k}\{(\frac{\kappa t^{\frac{1}{2}}}{\pi})e^{-\frac{x^2}{4\kappa t}} - \frac{x}{2}\mathrm{erfc}(\frac{x}{2\sqrt{\kappa t}})\}, \tag{3.2}$$

(ii) $t > t_{\mathrm{h}}$

$$T - T_0 = \frac{2q\kappa^{\frac{1}{2}}}{k}\{t^{\frac{1}{2}}\mathrm{ierfc}(\frac{x}{2\kappa^{\frac{1}{2}}t^{\frac{1}{2}}}) - (t-t_{\mathrm{h}})^{\frac{1}{2}}\mathrm{ierfc}(\frac{x}{2\kappa^{\frac{1}{2}}(t-t_{\mathrm{h}})^{\frac{1}{2}}})\}, \tag{3.3}$$

where T is temperature, T_0 is the initial temperature, q is the heat flux, t is time, t_{h} is the heating time, κ is the thermal diffusivity, which is equal to $k/\rho c$, erfc is the complementary error function given by

$$\mathrm{erfc}(x) = \frac{2}{\sqrt{\pi}}\int_x^\infty e^{-t^2}\mathrm{d}t. \tag{3.4}$$

The iterated integrals of the complementary error function are defined by

$$\mathrm{i}^n\mathrm{erfc}(z) = \int_z^\infty \mathrm{i}^{n-1}\mathrm{erfc}(\zeta)\mathrm{d}\zeta. \tag{3.5}$$

To verify the analytical results, thermal simulations using the commercial finite element code ABAQUS were performed. A heat flux load of 1.27 GW/m^2 was applied at the top surface for 1 ms. Two thermal simulations were carried out with constant thermal material parameters at room temperature and temperature dependent thermal material parameters, respectively. The analytical solution was obtained from equations (3.2) and (3.3). The analytically calculated temperature curve fits very well with the numerical solution with constant thermal material parameters, see figure 3.8. Figure 3.9 shows the maximum temperatures at various depths, which differ from the temperatures at the end of heating. When heating stops, the temperature at the top surface drops immediately, but the temperature in the deeper parts continuously increases shortly after, since the heat conduction into the material needs some time.

In order to predict more precise temperature profiles, the constant thermal material parameters at an elevated temperature - which is set to be half of the maximum temperature at the top surface - is applied in the analytical formula. The analytical temperature prediction using the constant thermal material parameters at the elevated temperature fits quite well with the thermal simulation based on the fully temperature dependent thermal material parameters, see figure 3.10.

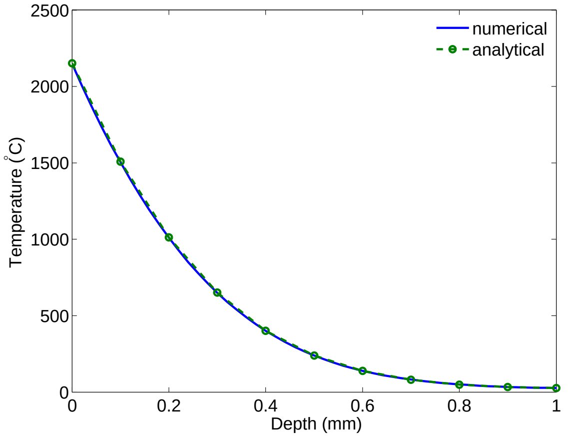

Figure 3.8: Temperature along depth predicted using analytical and numerical (ABAQUS) methods with constant thermal material parameters at room temperature.

3.4.2 Stress and strain calculations

Compared to the heat conduction problem, the thermo-elasto-plastic problem is more complex to derive an analytical solution. A number of analytical solutions have been carried out for one-dimensional thermo-elasticity and thermo-elasto-plastic problems, but there are only few existing studies concerning two-dimensional thermo-elasto-plastic problems. However, most of these studies are either dependent on numerical methods or on assumptions under which the geometry can be treated as a one-dimensional case. W. Mack and U. Gamer [59] studied thermal stress in an elasto-plastic disk exposed to a circular heat source, where the disk was assumed to be thin enough so that there was no temperature variation along the thickness direction. A transient thermo-elasto-plastic bending problem was solved by Ishihara [60] based on the strain increment theorem. In his work, temperatures and elasto-plastic deformations for the heating and cooling processes in a thin circular plate, which was subjected to partially distributed and axisymmetric heat supply on the upper face, were determined with the help of the generalized integral transforms and the finite difference method.

In this dissertation, for a rough estimation, the samples were assumed to consist of many thin disks that have no mechanical influence on each other. The assumption was based on the fact that, due to the free surface boundary conditions, there is nearly no out-of-plane stress in the vicinity of the central loading area in the thermal shock experiments - and plane stress was therefore assumed for the mechanical calculation in each thin disk. For simplicity, the outer edge is assumed to be fixed in the calculation. It is acceptable, since the heated material is constrained by cold bulk material outside the loading area. Thus, the problem is reduced to a thin disk with fixed ends under a homogeneous temperature loading, see figure 3.11. The temperature variation in each thin disk can be easily obtained by solving the transient heat conduction problem, as mentioned above.

If the temperature variation cannot generate the plastic strain, the stress will be zero at the end of

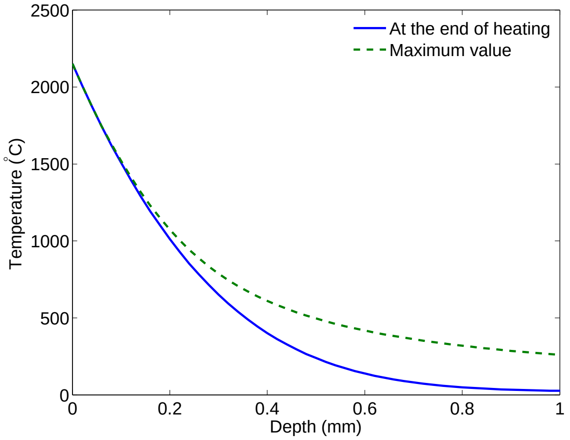

Figure 3.9: Temperature along depth at the end of heating and the maximum temperature at different depths predicted using analytical methods with constant thermal material parameters at room temperature.

cooling. The thin disk near the surface, where the residual stress occurs at the end of cooling, should be in the plastic regime at the end of heating. Using the Tresca criterion

$$\sigma_{zz} - \sigma_{rr} - \sigma_0 = 0, \tag{3.6}$$

$$\sigma_{zz} - \sigma_{\varphi\varphi} - \sigma_0 = 0, \tag{3.7}$$

and assuming plane stress (σ_{zz} = 0, σ_{zz} is stress in axial direction), the stresses can be calculated at the end of heating as follows:

$$\sigma_{\varphi\varphi} = \sigma_{rr} = -\sigma_0, \tag{3.8}$$

where σ_0 is the yield stress, while $\sigma_{\varphi\varphi}$ and σ_{rr} are the stresses in radial and hoop directions, respectively.

The plastic strains in radial direction are obtained using the fixed boundary condition at the outer edge by

$$\varepsilon_{\mathrm{h}}^{\mathrm{e}} + \varepsilon_{\mathrm{h}}^{\mathrm{p}} + \varepsilon_{\mathrm{h}}^{\mathrm{t}} = 0, \tag{3.9}$$

where $\varepsilon_{\mathrm{h}}^{\mathrm{e}} = -\frac{(1-\nu)\sigma_0}{E}$, $\varepsilon_{\mathrm{h}}^{\mathrm{t}} = \alpha(T_{\mathrm{max}} - T_0)$, T_0 is the initial temperature, and T_{max} is the maximum

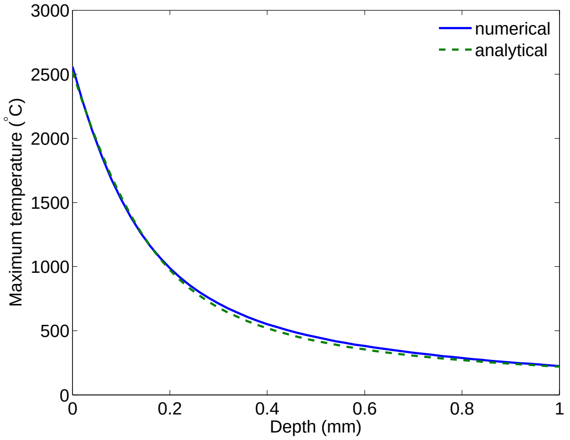

Figure 3.10: Maximum temperature as a function of depth predicted using analytical methods with constant thermal material parameters (obtained at elevated temperature) and numerical methods using temperature dependent parameters.

temperature. $\varepsilon_{\mathrm{h}}^{\mathrm{e}}$ and $\varepsilon_{\mathrm{h}}^{\mathrm{p}}$ are the elastic and plastic strains in radial direction generated during heating, respectively. $\varepsilon_{\mathrm{h}}^{\mathrm{t}}$ is the thermal strain in radial direction generated during heating.

During cooling, as the temperature is reduced to T_{c} - below which, according to the Tresca criterion, yield stress is not reached - the plastic strain in radial direction can be obtained by

$$\varepsilon_{\mathrm{c}}^{\mathrm{e}} - \varepsilon_{\mathrm{h}}^{\mathrm{e}} + \varepsilon_{\mathrm{c}}^{\mathrm{p}} + \varepsilon_{\mathrm{c}}^{\mathrm{t}} = 0, \tag{3.10}$$

where $\varepsilon_{\mathrm{c}}^{\mathrm{e}}$ and $\varepsilon_{\mathrm{c}}^{\mathrm{p}}$ are the elastic and plastic strains in radial direction generated as the temperature is decreased from T_{max} to T_{c}. The corresponding thermal strain, $\varepsilon_{\mathrm{c}}^{\mathrm{t}}$, equals to $\alpha(T_{\mathrm{c}} - T_{\mathrm{max}})$.

Combining equations (3.9) and (3.10), the total plastic strain in radial direction is obtained by

$$\varepsilon^{\mathrm{p}} = -\alpha(T_{\mathrm{c}} - T_0) - \varepsilon_{\mathrm{c}}^{\mathrm{e}}, \tag{3.11}$$

where $\varepsilon^{\mathrm{p}} = \varepsilon_{\mathrm{h}}^{\mathrm{p}} + \varepsilon_{\mathrm{c}}^{\mathrm{p}}$.

The plastic strains are identical in radial and hoop directions according to the Prandtl-Reuss flow rule. Due to the plastic volume constancy, the plastic strain in axial direction is obtained by

$$\varepsilon_{rr}^{\mathrm{p}} = \varepsilon_{\varphi\varphi}^{\mathrm{p}} = -\frac{1}{2}\varepsilon_{zz}^{\mathrm{p}}. \tag{3.12}$$

At the end of cooling, elastic strains in radial and hoop directions can be calculated by

$$\varepsilon_{rr}^{\mathrm{p}} + \varepsilon_{rr}^{\mathrm{e}} = 0, \tag{3.13}$$

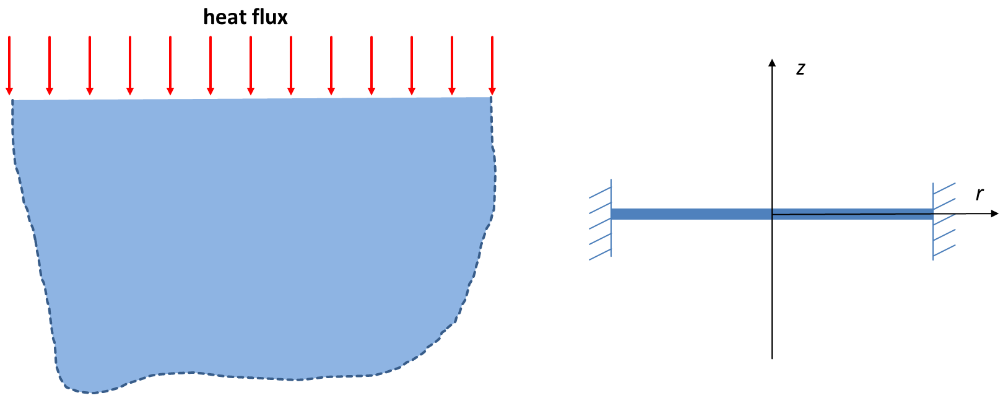

model for temperature calculation (a semi-infinite space)

model for stress and strain calculation at different depth (a thin disk with fixed ends)

Figure 3.11: A schematic drawing of the simplified models.

$$\varepsilon^{\mathrm{p}}_{\varphi\varphi} + \varepsilon^{\mathrm{e}}_{\varphi\varphi} = 0. \tag{3.14}$$

The elastic strain in axial direction is obtained from the plane stress assumption ($\sigma_{zz} = 0$):

$$\nu\varepsilon^{\mathrm{e}}_{rr} + \nu\varepsilon^{\mathrm{e}}_{\varphi\varphi} + (1-\nu)\varepsilon^{\mathrm{e}}_{zz} = 0. \tag{3.15}$$

According to Hooke's law, stresses in radial and hoop directions at the end of cooling are obtained by

$$\sigma_{rr} = \frac{E}{(1+\nu)(1-2\nu)}[(1-\nu)\varepsilon^{\mathrm{e}}_{rr} + \nu\varepsilon^{\mathrm{e}}_{\varphi\varphi} + \nu\varepsilon^{\mathrm{e}}_{zz}], \tag{3.16}$$

$$\sigma_{\varphi\varphi} = \frac{E}{(1+\nu)(1-2\nu)}[(1-\nu)\varepsilon^{\mathrm{e}}_{\varphi\varphi} + \nu\varepsilon^{\mathrm{e}}_{rr} + \nu\varepsilon^{\mathrm{e}}_{zz}]. \tag{3.17}$$

In the analytical calculation of stresses and strains, the temperature dependent yield stress and Young's modulus are considered.

To verify the analytical solution of stresses and strains, a reference mechanical simulation is performed using ABAQUS with temperature dependent parameters, and the predefined temperature field is calculated using ABAQUS as well. The finite element model is axisymmetric, see figure 3.12. In figures 3.13 and 3.14, a comparison is shown for residual stresses and plastic strains calculated

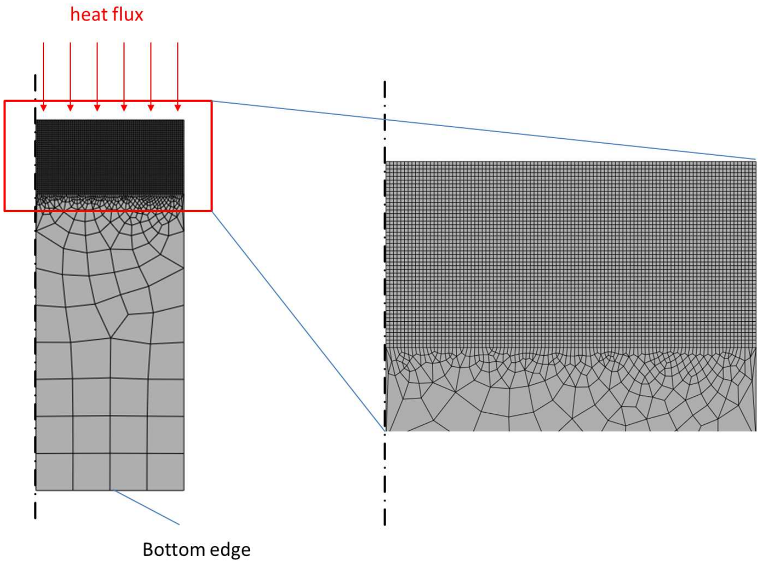

Figure 3.12: Meshes of axisymmetric model (left) and a zoom-in of the upper part (right). The bottom edge of the model and right edge are constrained in vertical direction and radial direction, respectively, assuming a semi-infinite space. The left edge is the axis of symmetry.

by analytical and numerical methods. The analytical solution agrees with the numerical solution quite well for both stress and plastic strain in radial direction. The minor deviation may result from the difference of temperature calculation, see figure 3.10, and the simplification in the mechanical model.

In figure 3.13, the magnitude of plastic strain in radial direction remains constant within a small depth. In the simplified model, different depths mean different thermal loadings for the thin disk. Figure 3.15 shows a schematic drawing of stress-strain curves for a thin disk with fixed boundaries under different loadings. The threshold load for plastic unloading is a thermal load with the minimum power density to generate plastic deformation during cooling. If the loading is large enough for plastic unloading, plastic strains are identical at the end of cooling. Therefore, the constant plastic strain within a small depth indicates that the temperature variation within this depth can cause plastic unloading.

As in the thermal shock experiments, parametric studies of power density and base temperature were performed using the simplified analytical solutions. For analytical solutions, see figure 3.16, plastic strains in radial direction at the top surface do not change with increasing the power density. As a result, the stresses in radial direction at the top surface for the three loadings are identical, see figure 3.17. The difference is that, for a larger power density, the plastic strain and the stress can occur at a larger depth. Figure 3.18 shows the influence of base temperature on plastic strains in radial direction. A higher base temperature leads to a smaller plastic strain at the top surface, but the plastic zone extends to a larger depth. In consequence of the smaller plastic strain at a higher base

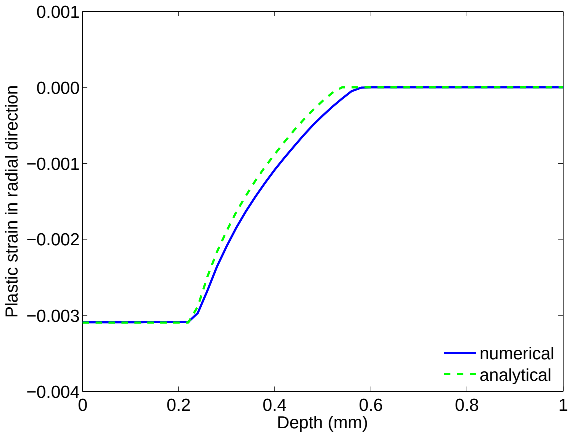

Figure 3.13: Plastic strain in radial direction at the end of cooling calculated by analytical and numerical methods.

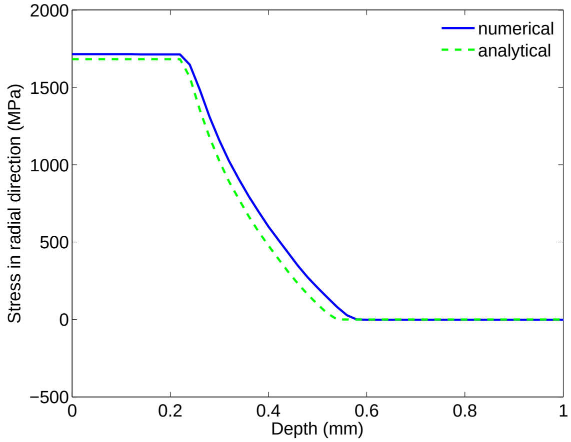

Figure 3.14: Stress in radial direction at the end of cooling calculated by analytical and numerical methods.

temperature, the stress is smaller than that at a lower base temperature, see figure 3.19.

3.4.3 Stress intensity factor calculation

With the stresses derived from the simplified analytical model, the stress intensity factor can be calculated with proper weight functions. In this part, a weight function $h(x, a)$ is used for edge cracks in a semi-infinite space with only the normal stress distribution along the prospective crack line [27], see equation (2.13). Stress intensity factor K_I is calculated for different power densities and base temperatures, see figure 3.21. First, the stress intensity factor increases rapidly together with increasing crack length, since the residual stress remains constant in the top surface layer, see figure 3.19. Then the stress intensity factor decreases with a further increasing crack length, since the stress decreases with growing depth. The fracture toughness, which is the critical value of the stress

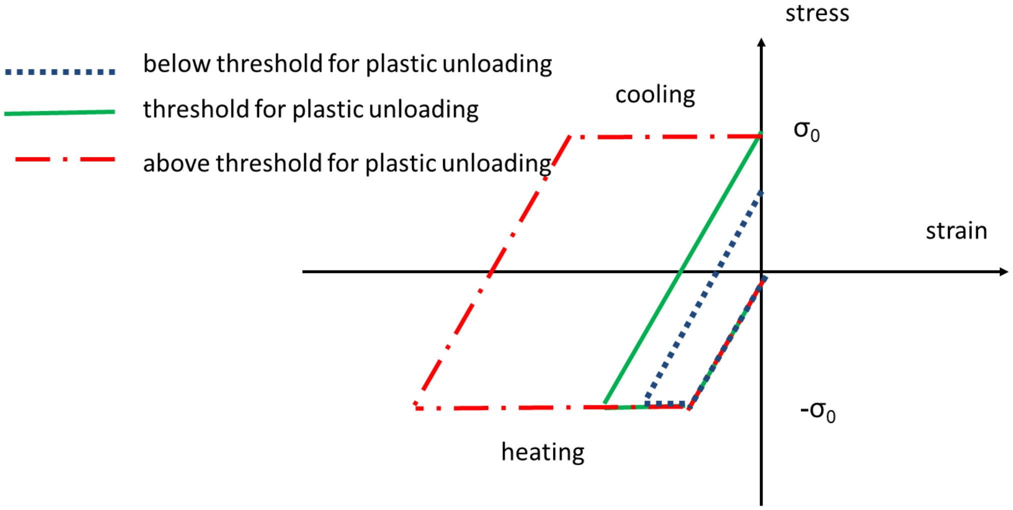

Figure 3.15: A schematic drawing of stress-strain curves in a thin disk with fixed ends for different loadings.

intensity factor of mode I, increases as the temperature increases. The experimentally determined fracture toughness is shown in figure 3.20 as a function of temperature. As a result, the crack has much more difficulties to propagate at a high base temperature than at a low one.

Compared to the interior of grain the grain boundaries are weaker areas in tungsten, and crack formation in general follows the grain boundaries [47]. The average grain diameter in the thermal shock experiments [47] ranges from 25 µm to 64 µm. 20 µm is assumed to be the precrack length, which can be developed from the initial defects along the grain boundary at the sample surface. When the stress intensity factor for a crack of 20 µm is larger than the critical value, it is assumed that cracking occurs. Figure 3.22 shows a failure map obtained by comparing the stress intensity factor for precracks with the fracture toughness at different temperatures.

The failure map shows that cracking occurs only at low base temperatures, which indicates that cracking is related to the brittleness of tungsten below DBTT. The predicted failure map agrees with the experimental observations put down in figure 3.5. However, it should be noted that the calculation of stress intensity factors is conducted under the assumption of a semi-infinite space, which results in some discrepancies with the experimental results in both stress and stress intensity factor calculations.

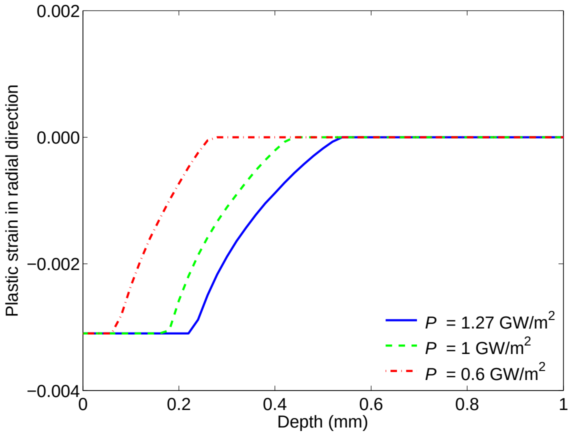

Figure 3.16: Plastic strain in radial direction along the depth at the end of cooling for different power densities, P, and a base temperature of 20 °C.

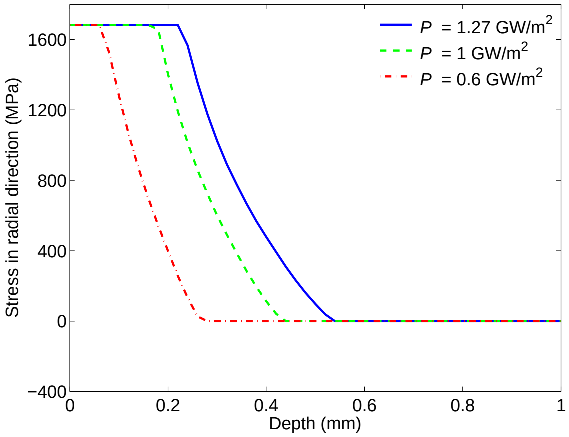

Figure 3.17: Stress in radial direction along the depth at the end of cooling for different power densities, P, and a base temperature of 20 °C.

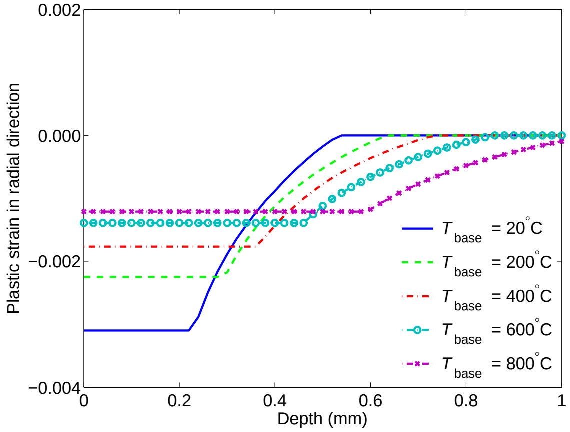

Figure 3.18: Plastic strain in radial direction along the depth at the end of cooling for different base temperatures, T_{base}, and a power density of 1.27 GW/m^2.

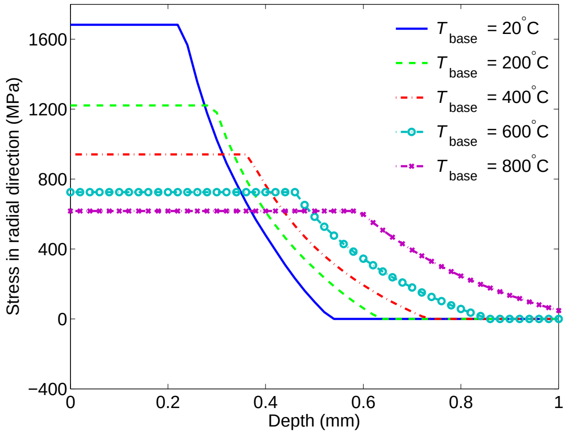

Figure 3.19: Stress in radial direction along the depth at the end of cooling for different base temperatures, T_{base}, and a power density of 1.27 GW/m^2.

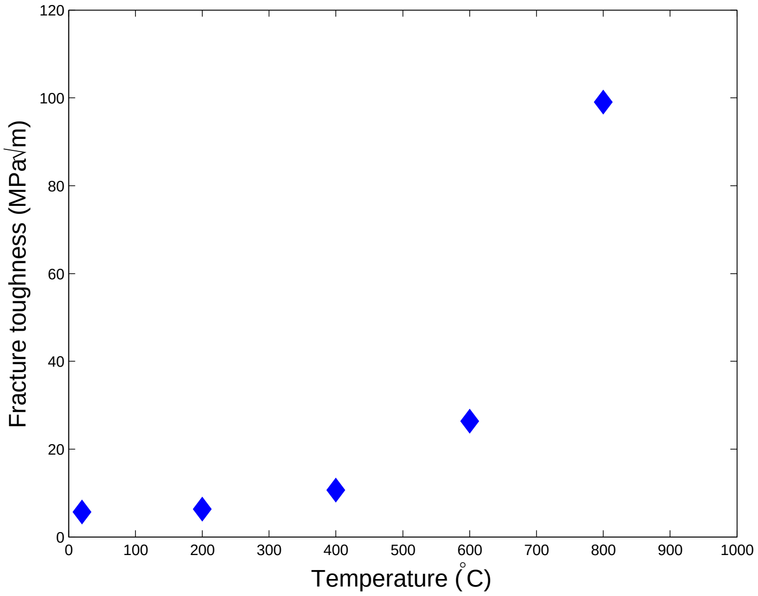

Figure 3.20: Fracture toughness, K_{IC}, of tungsten as a function of temperature based on the data listed in [61].

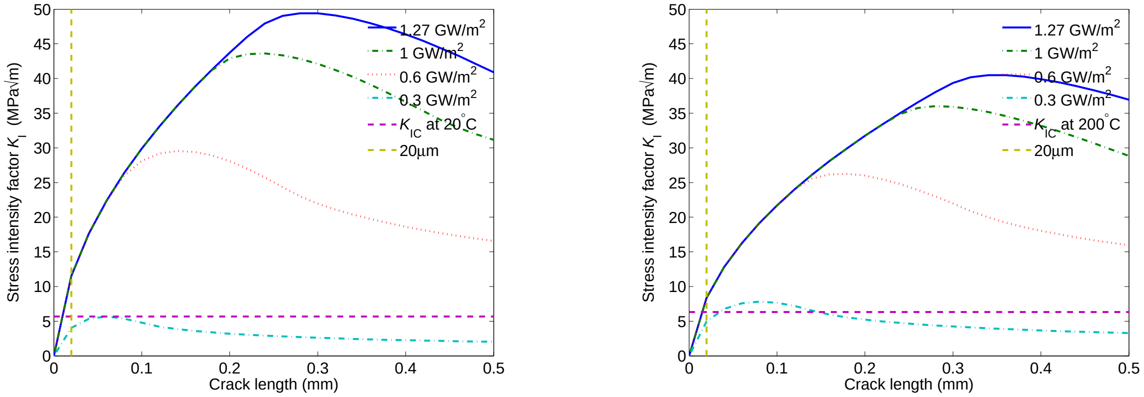

(a) base temperature 20°C (b) base temperature 200°C

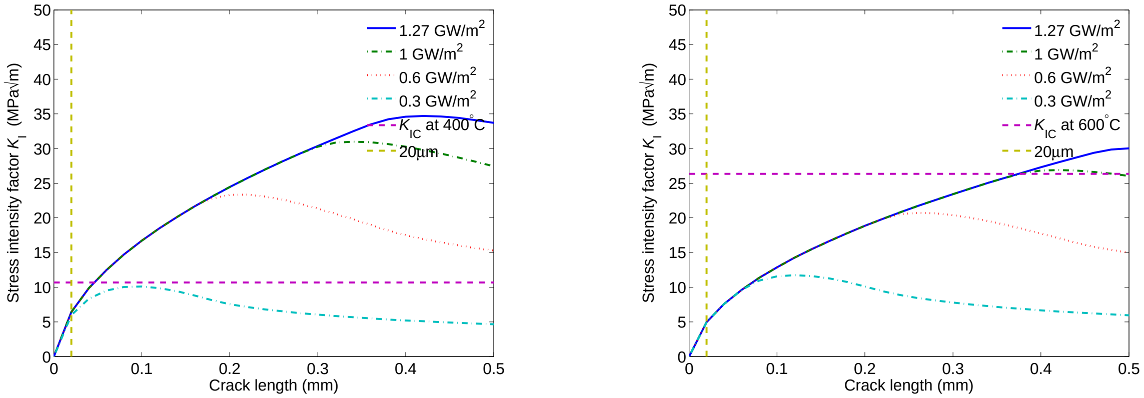

(c) base temperature 400°C (d) base temperature 600°C

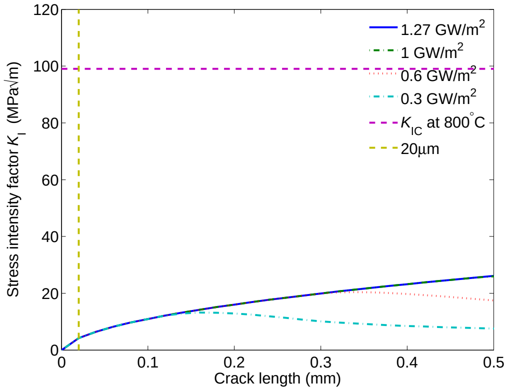

(e) base temperature 800°C

Figure 3.21: Stress intensity factors calculated for loadings with 0.3-1.27 GW/m^2 and base temperature 20 °C-800 °C. Fracture toughness of tungsten, K_{Ic}, and the assumed precrack length, 20 μm, for determining the failure map are marked in the plot.

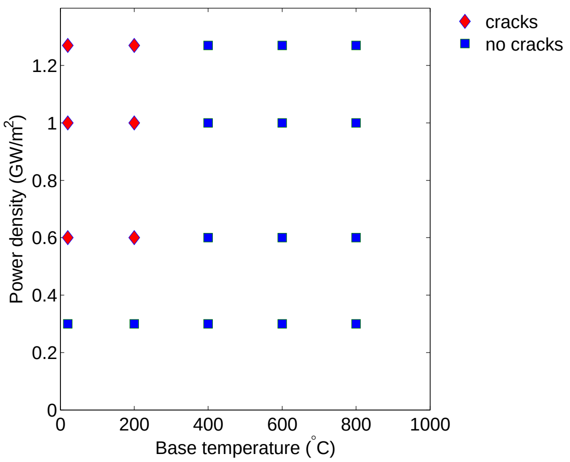

Figure 3.22: The failure map calculated by comparing the stress intensity factor for a crack of 20 μm with the fracture toughness of tungsten listed in [61].

3.5 FEM simulation of thermal shock experiments at Forschungszentrum Jülich

3.5.1 Model geometry

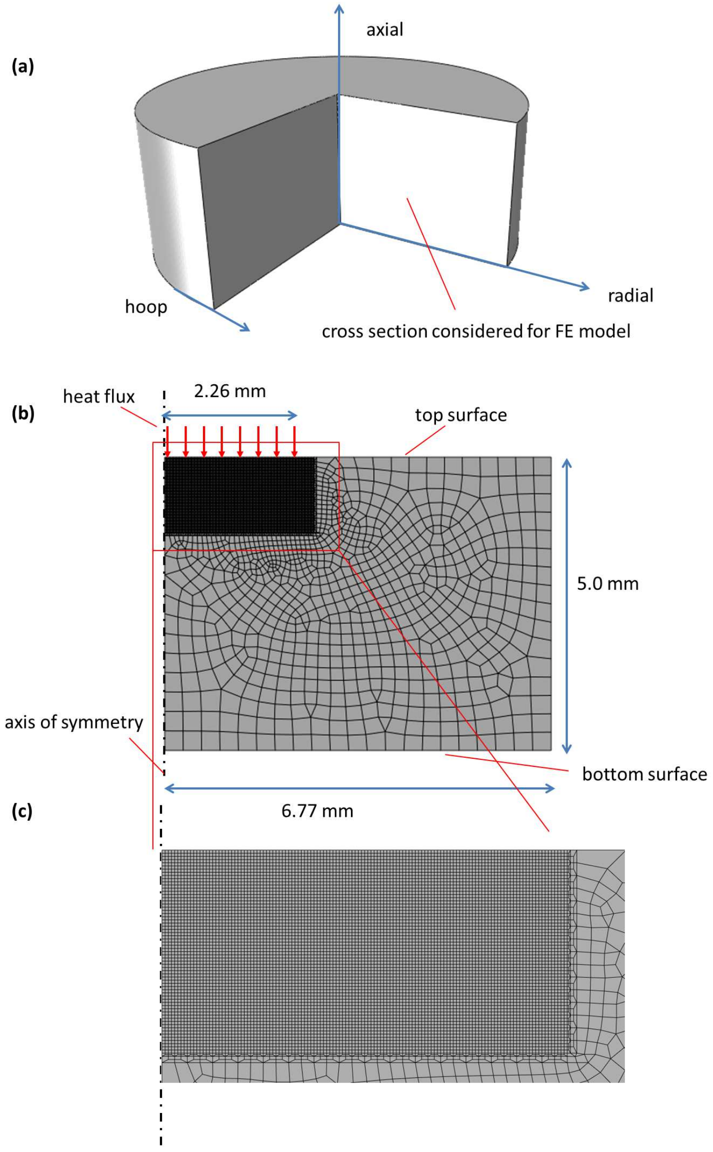

Figure 3.23: (a) A schematic drawing of the model geometry, (b) two-dimensional FE model created for the right half of the vertical cross section. The mesh consists of axisymmetric elements reflecting the rotational symmetry of the model, (c) finer mesh in the vicinity of the region of heat flux loading.

The finite element (FE) model was built according to typical settings realized in thermal shock experiments at Forschungszentrum Jülich. Tungsten samples with dimensions of 12 mm × 12 mm

× 5 mm are mounted on a heated sample holder, so that the base temperature of the samples can be adjusted between room temperature and 800 °C. A nearly homogeneous heat flux load is achieved in a square of 4 × 4 mm^2 at the top surface of the sample by fast scanning of the surface with an electron beam.

In the FE model, a disk shaped sample was considered instead of the real dimensions of the tungsten sample (see figure 3.23 a). The area of the top surface and the height of the disk model were the same as those of the tungsten sample. The loading area was assumed to be a circle with an area of 16 mm^2 instead of a square. As a consequence of these simplifications, a two-dimensional axisymmetric model was set up for the right half of the vertical cross section considering the rotational symmetry of the model geometry, see figure 3.23 b. The advantage of the simplified model is that one can save computational efforts by reducing the dimension of the FE model, and one can avoid convergence problems possibly encountered in three-dimensional fracture simulations. The simulation tool for the computation was the commercial FEM code ABAQUS [11]. The finite element used in the simulations was a four-node axisymmetric quadrilateral element. To avoid mesh sensitive results, it is necessary to build a sufficiently fine mesh in the vicinity of the region of heat flux loading and the element edge size there was 20 μm (see figure 3.23 c).

3.5.2 Loads and boundary conditions

The heat flux load ranging from 0.15 $\mathrm{GW/m}^2$ to 1.3 $\mathrm{GW/m}^2$ was applied at the top surface of the tungsten sample to simulate the electron beam loading. The heat flux load was applied at the top surface of the tungsten sample to simulate the electron beam loading. When the electron beam is focused on a small spot at the sample surface, a very high power density is generated. The kinetic energy of incident electrons is dissipated not only at the top surface but also deeper in the material. The electron beam penetration depth is dependent mainly on the energy of the electrons and the target material. For the loadings and material relevant for this study, the penetration depth is less than 5 μm [46]. Therefore, the penetration of the electron beam was not considered in this chapter. The heat flux load was applied to the heating area at the top surface of the sample for 1 ms. According to the thermal calculation, the heat transfer between the bottom surface of tungsten and the sample holder has nearly no impact on the temperature at the top surface. For simplicity, a convective boundary condition was applied at the bottom surface. The power density of the electron beam loading is much larger than the energy loss due to radiation. As a result, the radiation effect can be neglected when calculating the temperature. To prevent rigid body movement, one node was fixed at the right corner of the model. In the simulation, the thermal excursion of tungsten consists of two steps, namely, 1 ms of heat flux loading and 10 s of cooling.

Cracking of tungsten was observed in single thermal shock experiments as well as multiple thermal shocks experiments [46, 47]. In experiments comprising up to 100 thermal shocks, the minimum crack distance was found to be larger than the maximum grain diameter. This indicates a brittle crack formation, since in thermal fatigue induced crack formation, the crack distances were not related to the grain diameter [48]. However, increasing the cycle number from 1 to 100 can cause the formation of numerous micro-cracks [62], which can lead to macro-cracks during further cycles. In this chapter, the numerical simulations aim at simulating cracking induced by the brittleness of tungsten, whereas thermal fatigue damage was not considered. Furthermore, only one thermal cycle was simulated, for the reason mentioned above.

3.5.3 Thermal simulation

The heat transfer problem was solved first. After that, the solution was read into the corresponding mechanical simulation as a predefined temperature field.

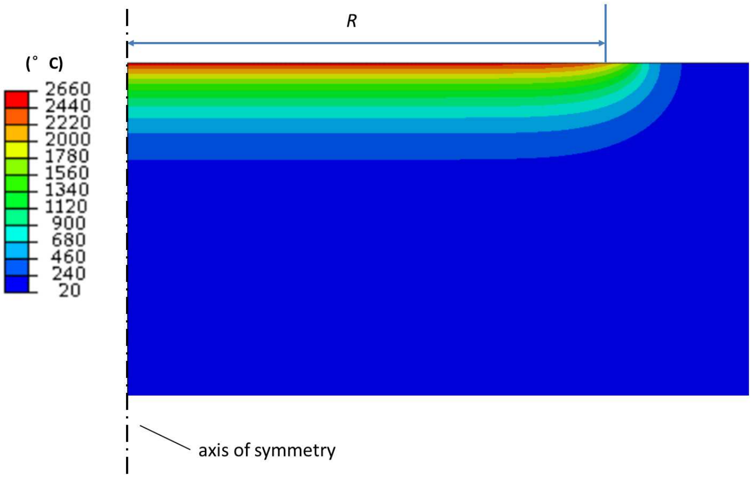

Figure 3.24: Temperature distribution at the end of heating for a power density of 1.27 GW/m^2 and a base temperature of 20 °C. R = the radius of the loading area.

Figure 3.24 shows the temperature distribution at the end of heating for a power density of 1.27 GW/m^2. As the loading is homogeneous, the temperature changes only with respect to depth direction, which confirms the assumption in the previous analytical solution. Figure 3.25 shows the surface temperatures as a function of time for a power density of 1.27 GW/m^2 and a base temperature of 20 °C. The top surface is heated up to over 2500 °C within 1 ms, and after heating stops, the surface temperature is reduced to 1000 °C within 1 ms. This extreme temperature variation within several milliseconds was confirmed by surface temperature measurements by fast infrared and visible imaging in ELM simulation experiments [63]. Figure 3.26 shows the sample temperature at different depths at the end of heating. Only the surface layer experiences a temperature above DBTT. At a depth of 480 μm, the temperature is below 400 °C.

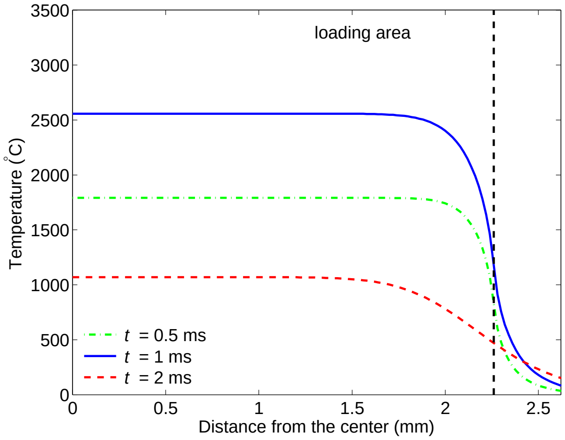

Figure 3.25: Surface temperature at various times, t, for a power density of 1.27 GW/m^2 and a base temperature of 20 °C.

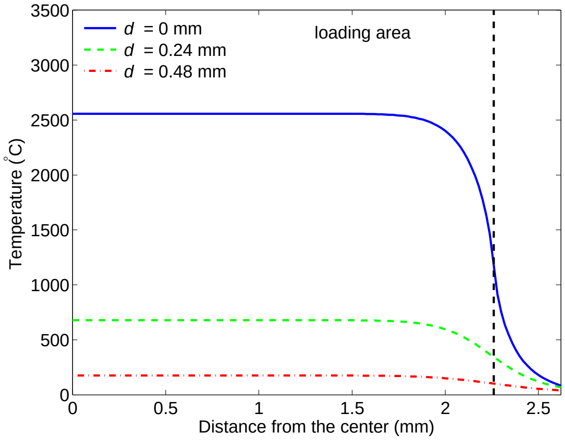

Figure 3.26: Temperature at different depths, d, at the end of heating for a power density of 1.27 GW/m^2 and a base temperature of 20 °C.

3.5.4 Mechanical simulation

Plastic strains are generated by the marked temperature variations in the loading area. Figures 3.27 and 3.28 show the distributions of plastic strain in radial direction for a power density of 1.27 GW/m^2 and a base temperature of 20 °C. During heating, the material in the loading area tends to expand due to the temperature increase, but it is constrained by the cold and rigid bulk material outside the loading area. Thus, the material in the loading area is in a compressive stress state, and compressive plastic strains are generated, see figure 3.27. During cooling, the material in the loading area shrinks rapidly due to the fast decrease of temperature. Shrinkage is constrained by the bulk material surrounding the loading area. As a result, the material in the loading area is subjected to tensile stresses. However, plastic stains resulting from the tensile stresses cannot compensate the plastic strains generated during heating. Plastic strains are found at the end of cooling, see figure 3.28.

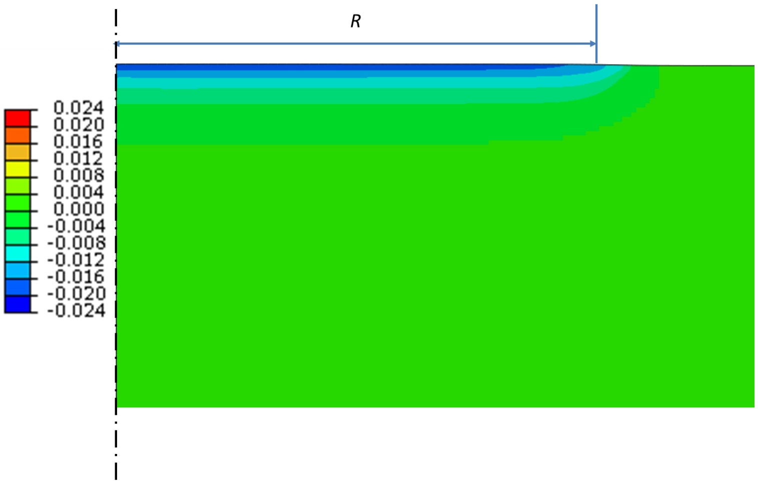

Figure 3.27: Distribution of plastic strain in radial direction at the end of heating for a power density of 1.27 GW/m^2 and a base temperature of 20 °C.

Figure 3.29 shows surface plastic strain in radial direction for a power density of 1.27 GW/m^2 and a base temperature of 20 °C at various moments. In the central part of the loading area, plastic strains generated by compressive stresses during heating are significantly reduced when the tungsten sample is cooled down. At the beginning of cooling, thermal stresses surpass tungsten's yield stress, and plastic strains are generated by tensile stresses. Since the yield stress increases with decreasing temperature, tungsten behaves purely elastic upon further cooling. Plastic strains resulting from the tensile stresses cannot completely compensate plastic strains generated during heating, which indicates that tensile residual stress will be present. During cooling, much smaller plastic deformation is generated by tensile stresses near the edge of the loading area than in the center. As a result, the magnitude of the plastic strain near the edge of the loading area is larger than in the central part of the loading area at the end of cooling. At the edge of the loading area, a trough can be observed in the plastic strain distribution. Material that is subjected to less intensive temperature variations (e.g. deeper beneath the heat flux loading) will experience less or no plastic strain generated by tensile stresses during cooling. No trough exists in the plastic strain distribution (see the plastic strain at depths of 0.24 mm and 0.48 mm in figure 3.30).

Figures 3.31 and 3.32 show the stress distributions for a power density of 1.27 GW/m^2 and a base temperature of 20 °C. In the loading area, the surface stress in radial direction is compressive during heating ($t \leq 1$ ms) and tensile during cooling ($t > 1$ ms). Figure 3.33 shows surface stress in radial direction as a function of the distance from the loading center. Since tungsten is assumed to behave ideally plastic, the stress near the top surface during heating is limited by the small yield stress of tungsten at high temperature.

The temperature dependent physical properties of tungsten have a large impact on stresses. The stress in radial direction is compressive during heating and tensile during cooling in the loading

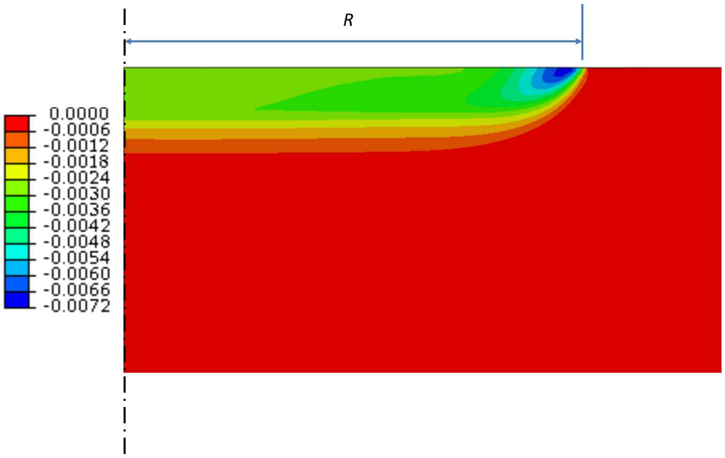

Figure 3.28: Distribution of plastic strain in radial direction at the end of cooling for a power density of 1.27 GW/m^2 and a base temperature of 20 °C.

area. Figure 3.33 shows the surface stresses in radial direction at various times. During heating, the stress at the top surface is limited by the small yield stress of tungsten at high temperatures. After the sample is cooled down, high tensile residual stress is generated near the top surface. The peak stress in radial direction is observed near the edge of the loading area at the top surface. An out of surface deformation in the loading area is predicted at end of cooling, as shown in figure 3.34. The vertical displacement is qualitatively in good agreement with the results of a profilometry scan converted into a depth profile along the middle of the loading area in the thermal shock experiments [62]. Due to incompressibility of the material during plastic deformation, the region outside the loading area sinks down. The out of surface deformation and the sinking of material result in a tensile stress near the edge of the loading area. Furthermore, the compressive plastic deformation near the edge of the loading area is larger than in the central part of it. As a result, the stress in radial direction is larger near the edge of the loading area.

In figure 3.35, stress in radial direction is shown for a power density of 1.27 GW/m^2 and a base temperature of 20 °C at different depths at the end of cooling. The profile of stress in radial direction along the depth direction leads to bending of the sample. As a result, a compressive stress state can be observed at a depth of 0.48 mm, see figure 3.35.

Figure 3.36 shows curves of stress-mechanical strain in radial direction at three positions, which are located at different depths along the axis of symmetry. The three curves represent three types of loading and unloading: purely elastic loading and unloading, plastic loading and elastic unloading, and plastic loading and unloading. Purely elastic loading and unloading occur if no plastic deformation is generated in the whole loading history, as represented by the stress-mechanical strain curve for a depth of 0.48 mm. Plastic loading and elastic unloading are defined when there is plastic behavior during heating but no plastic deformation is generated during cooling, see the stress-mechanical strain curve at a depth of 0.24 mm. If plastic deformation occurs both in the heating and the cooling

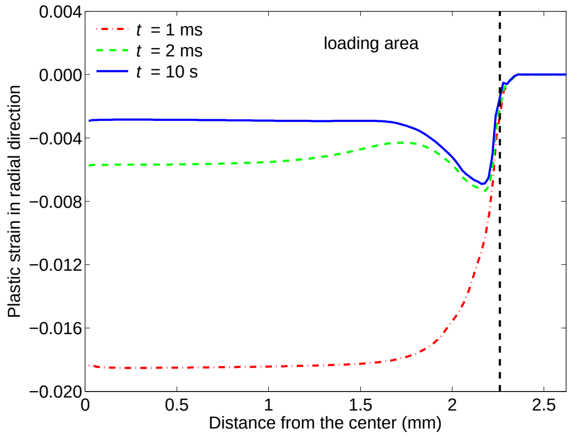

Figure 3.29: Surface plastic strain in radial direction at various times, t, for a power density of 1.27 GW/m^2 and a base temperature of 20 °C.

parts, the resulting behavior is termed as plastic loading and unloading, see the stress-mechanical strain curve predicted for the top surface.

3.5.5 Effect of power density

To study the effect of power density on the behavior of tungsten, different power densities ranging from 0.3 GW/m^2 to 1.27 GW/m^2 were applied in the simulations. Figure 3.37 shows surface temperature at the end of heating for several power densities and a base temperature of 20 °C. The maximum temperature is proportional to the power density. When the power density is larger than 0.6 GW/m^2, the maximum temperature is above DBTT of tungsten. Figure 3.38 shows plastic strain in radial direction for different power densities. When the power density is large enough for plastic unloading, additional plastic strains resulting from an increase of power density are nearly the same in the heating and the cooling periods. As long as plastic unloading occurs at the top surface, plastic strains in the central part of the loading area will therefore be identical. For power densities between 0.6 GW/m^2 and 1.27 GW/m^2, nearly identical plastic strains in radial direction are found in the central part of the loading area. When loading with 0.3 GW/m^2, plastic strain in radial direction is much smaller. Thus, the threshold power density for plastic unloading lies between 0.3 GW/m^2 and 0.6 GW/m^2. The trough in the plastic strain distribution curve becomes deeper as power density increases.

Figure 3.39 shows surface stress in radial direction at the end of cooling for different power densities and a base temperature of 20 °C. For a power density of 0.3 GW/m^2, the stress in radial direction is much smaller than for the loadings above the threshold power density for plastic unloading. For loadings between 0.6 GW/m^2 and 1.27 GW/m^2 peak stress increases as power density increases. However, tensile stress in the central part of the loading area decreases slightly as power density

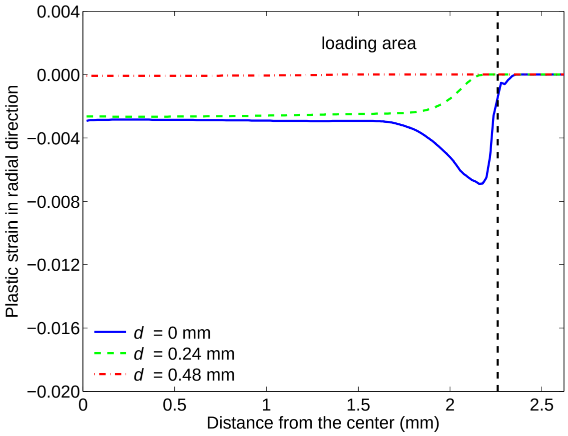

Figure 3.30: Plastic strain in radial direction at different depths, d, at the end of cooling for a power density of 1.27 GW/m^2 and a base temperature of 20 °C.

increases.

3.5.6 Effect of base temperature

Due to the strong temperature dependence of tungsten's physical properties, base temperature of the sample plays an important role for the behavior of tungsten under heat flux loadings. In the course of chapter, base temperatures ranging from 20 °C to 800 °C were applied. The base temperatures are used to mimic the temperature induced by the stationary thermal loading. Thus, the simulations under short transient thermal loads with a high base temperature serve to estimate the conditions of tungsten being exposed to both stationary and transient thermal loads. Figure 3.40 shows the surface temperature at the end of heating for different base temperatures. The surface temperature increases as base temperature increases. When the base temperature reaches 800 °C, the maximum temperature is close to the melting point of tungsten (3422 °C) for a power density of 1.27 GW/m^2. In figure 3.41, surface plastic strain in radial direction is shown at the end of cooling for different base temperatures. In the central part of the loading area, the magnitude of plastic strain in radial direction decreases as base temperature increases. The reason for this is that by increasing base temperature, the increase of plastic formation during heating is smaller than during cooling. The plastic strain in radial direction occurs outside the loading area, when the base temperature is above 400 °C. The trough in the plastic strain distribution curve is deeper for a higher base temperature. Figure 3.42 shows the equivalent plastic strain at the top surface at the end of cooling for different base temperatures. The equivalent plastic strain increases as base temperature increases, which indicates that thermal fatigue damage is more likely to occur for a higher base temperature under repeated heat flux loads. Surface stress in radial direction at the end of cooling is plotted in figure 3.43 for different base temperatures. The stress level is significantly reduced as base temperature becomes higher.

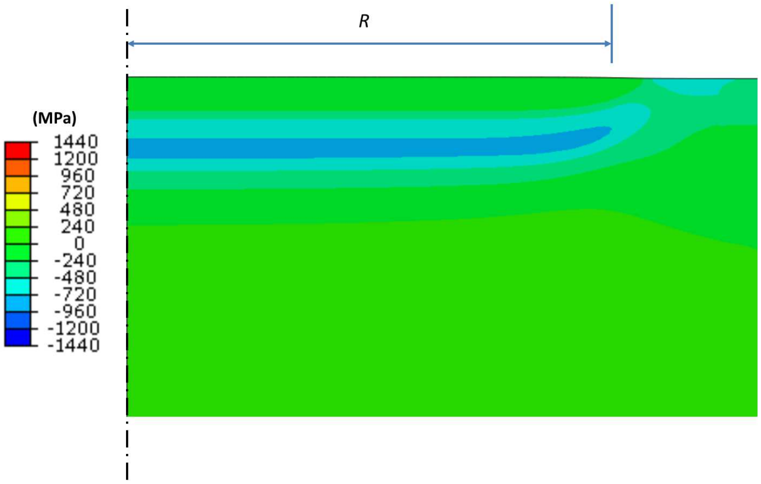

Figure 3.31: Distribution of stress in radial direction at the end of heating for a power density of 1.27 GW/m^2 and a base temperature of 20 °C.

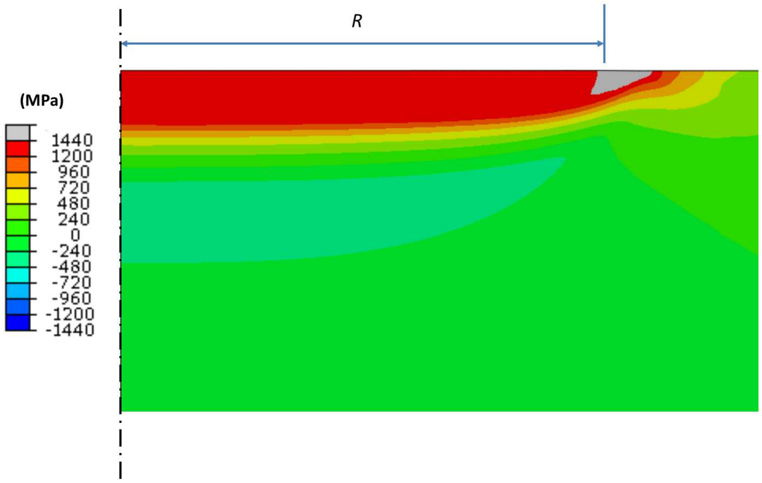

Figure 3.32: Distribution of stress in radial direction at the end of cooling for a power density of 1.27 GW/m^2 and a base temperature of 20 °C.

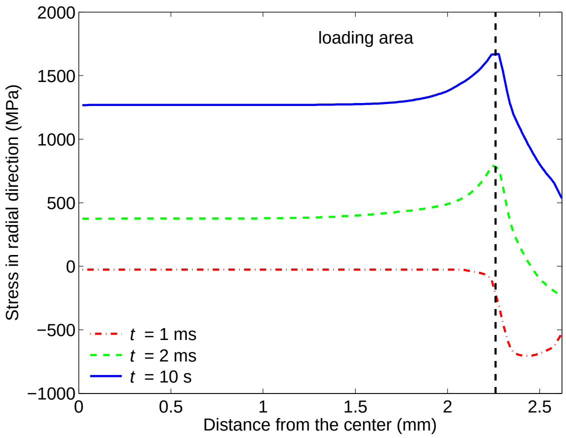

Figure 3.33: Surface stress in radial direction at various times, t, for a power density of 1.27 GW/m^2 and a base temperature of 20 °C.

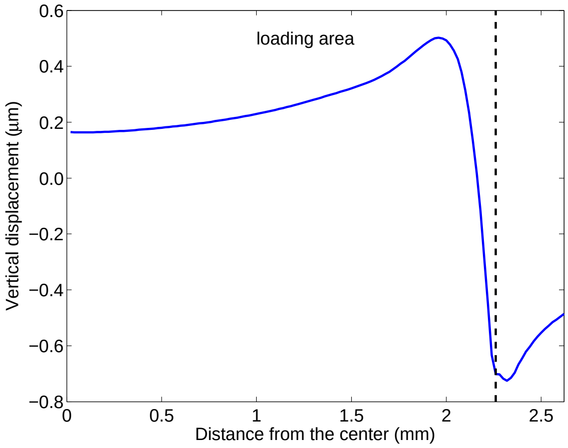

Figure 3.34: Surface vertical displacement at the end of cooling for a power density of 1.27 GW/m^2 and a base temperature of 20 °C.

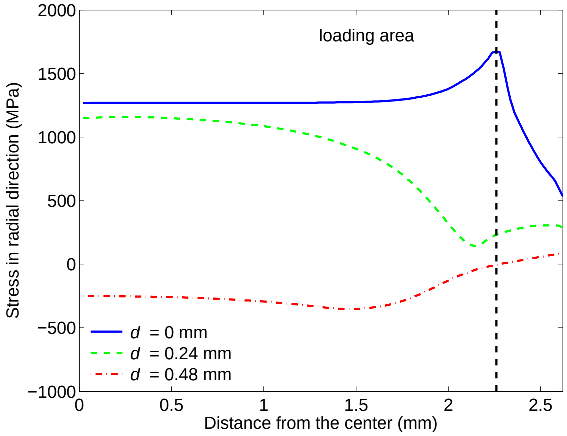

Figure 3.35: Stress in radial direction at different depths, d, at the end of cooling for a power density of 1.27GW/m^2.

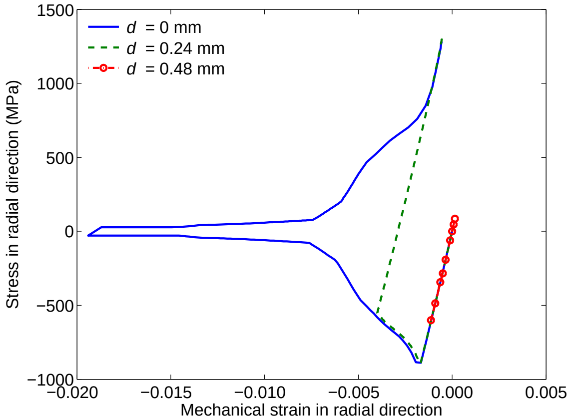

Figure 3.36: Stress-mechanical strain in radial direction at different depths, d, for a power density of 1.27 GW/m^2 and a base temperature of 20 °C.

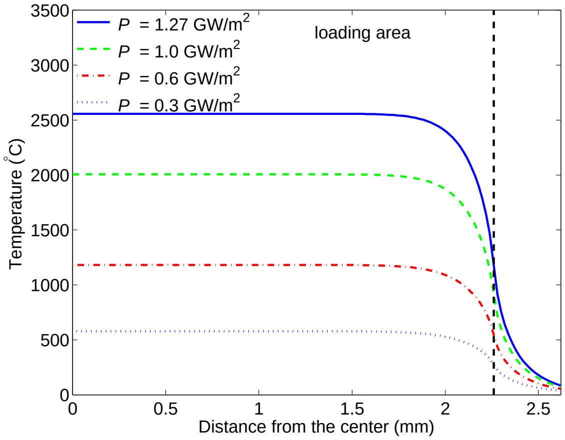

Figure 3.37: Surface temperature at the end of heating for different power densities, P, and a base temperature of 20 °C.

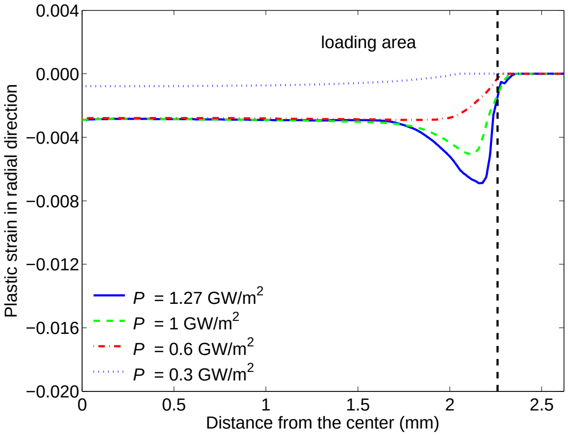

Figure 3.38: Surface plastic strain in radial direction at the end of cooling for different power densities, P, and a base temperature of 20 °C.

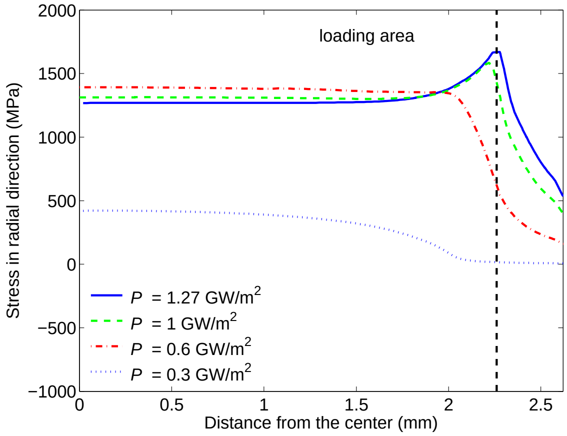

Figure 3.39: Surface stress in radial direction at the end of cooling for different power densities, P, and a base temperature of 20 °C.

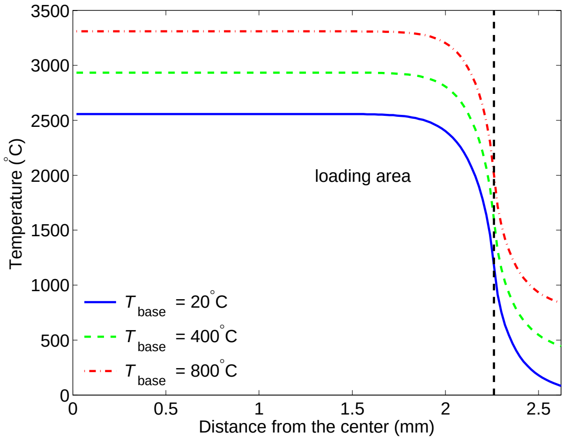

Figure 3.40: Surface temperature at the end of heating for different base temperatures, T_{base}, and a power density of 1.27 GW/m^2.

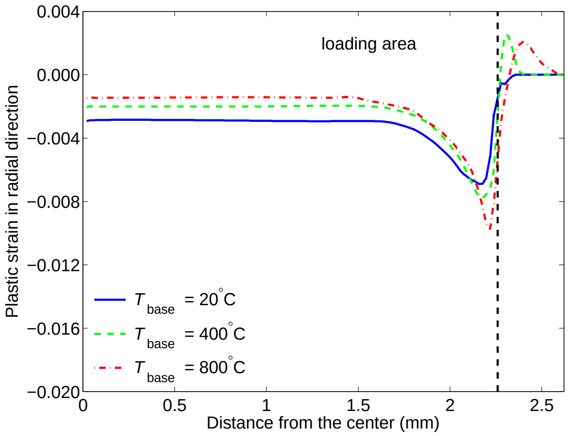

Figure 3.41: Surface plastic strain in radial direction at the end of cooling for different base temperatures, T_{base}, and a power density of 1.27 GW/m^2.

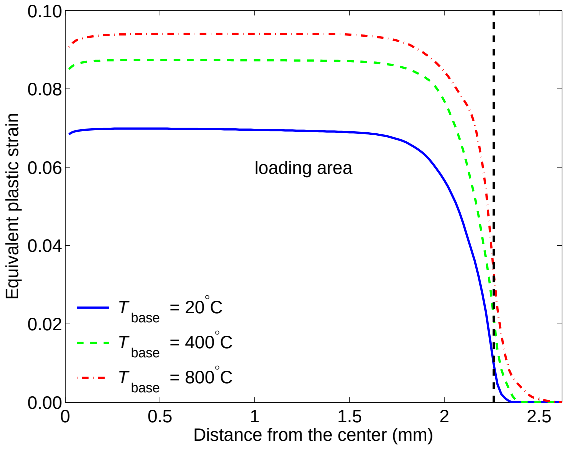

Figure 3.42: Equivalent plastic strain at the top surface at the end of cooling for different base temperatures, T_{base}, and a power density of 1.27 GW/m^2.

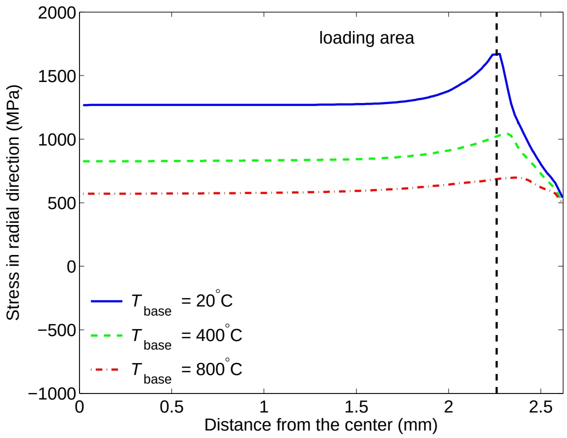

Figure 3.43: Surface stress in radial direction at the end of cooling for different base temperatures, T_{base}, and a power density of 1.27 GW/m^2.

3.6 Fracture simulation of thermal shock experiments at Forschungszentrum Jülich

3.6.1 XFEM simulation

To simulate crack initiation and propagation using XFEM, a maximum principal stress (MPS) criterion and an energy based damage evolution law are needed. Once the principal stress exceeds the maximum allowable value, a crack is initiated. At the same time, there is a degradation of the cohesive stiffness in the elements in which the crack formation occurs, which can be described by the energy based damage evolution law. If the energy dissipation associated with crack extension is larger than the fracture energy, the cohesive stiffness becomes zero, and the crack opens up completely. The value of the ultimate tensile strength can in principle be used as an estimate for the MPS. The ultimate tensile strength of tungsten in the vicinity of DBTT (400 °C-700 °C) is about 900 MPa-700 MPa [8]. Considering that crack formation is mainly due to the brittleness of tungsten below DBTT, the MPS is defined to be 900 MPa. For the fracture energy in the course of damage evolution, 0.25 mJ/mm^2 is used, which is transferred from the fracture toughness obtained from the test performed at 400 °C by Gludovatz et al. [61] applying the concept of linear elastic fracture mechanics.

To avoid a possible influence by multiple cracks, the XFEM simulations were first carried out by introducing a single precrack of 20 μm length, and no other crack initiation was allowed. Figure 3.44 shows the crack propagation predicted by introducing the precrack at different positions for a power density of 1.27 GW/m^2. Precracks positioned in the central part of the loading area propagate perpendicularly to the loading surface, while a precrack near the edge of the loading area grows parallel to the loading surface at a depth of about 500 μm, which coincides well with experimental findings [47]. A precrack near the edge of the loading area grows towards the center of the loading area because it experiences both tensile and shear loads, while in the central part of loading the stress is near purely tensile. When multiple thermal shocks are applied, the crack opening resulting from the previous thermal shock will change the stress and strain distributions, so that the stress may not be purely tensile in the central part of the loading area. As a result, crack growth parallel to the loading surface may also occur in the central part of the loading area.

XFEM models a crack as an enriched feature by adding degrees of freedom in elements with special displacement functions, and one or multiple pre-existing cracks can be associated with an enriched feature. In addition, during the simulation one or multiple cracks can initiate in an enriched feature without any initial defects. However, multiple cracks can nucleate in a single enriched feature only when the damage initiation criterion is satisfied in multiple elements in the same time increment. Otherwise, there will be no additional cracks until all pre-existing cracks in an enriched feature have propagated through the boundary of the given enriched feature.

For XFEM simulations with multiple cracks, multiple enriched features were applied (see figure 3.45)

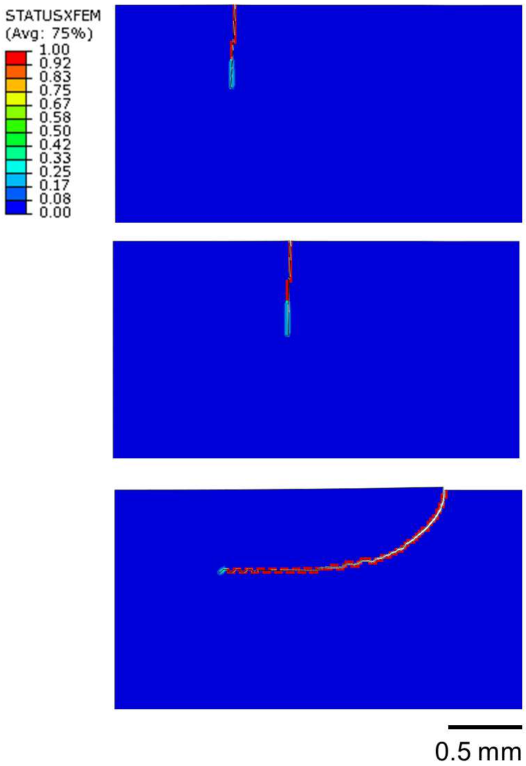

Figure 3.44: Cracks predicted using XFEM with a global enriched feature and precracks at different locations (top: 0.8 mm away from the center, middle: 1.2 mm away from the center, bottom: 2.24 mm away from the center) for a power density of 1.27 GW/m^2 and a base temperature of 20 °C. The quantity STATUSXFEM characterizes damage evolution. A value of 1.0 characterizes an opened crack. Positive values smaller than 1.0 stand for cracks that require additional energy to be opened.

so that cracks can nucleate without waiting for the pre-existing cracks to propagate in other enriched features. Figure 3.46 shows the cracks predicted using XFEM for loadings of different power densities. Cracks are initiated near the top surface perpendicularly to the loading surface and are not fully opened. However, in the XFEM simulations with a single crack, the crack in central part of the loading area is much longer and fully opened (see figure 3.44), since when multiple cracks are initiated in the central part of the loading area, the stiffness is degraded in such a way that the stress concentration at the crack tips is not as intensive as in the XFEM simulations with a single crack. For the loadings with 1.27 GW/m^2 and 1 GW/m^2, cracks are generated near the edge of the loading area and propagate parallel to the loading surface. For a power density of 0.6 GW/m^2, no crack is formed near the edge of the loading area, as there is no stress concentration, see figure 3.39. No crack initiation is found for the loading with 0.3 GW/m^2, since the stress is much smaller than the MPS. The XFEM results are capable of reproducing the main cracking features observed in the experiments [47].

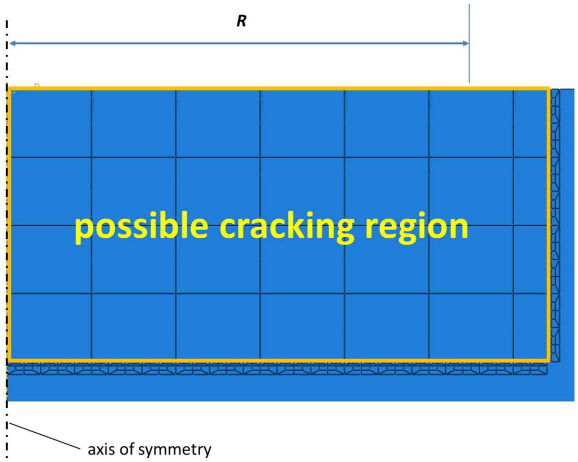

Figure 3.45: Enriched features defined in each small domain in the possible cracking region for XFEM simulations, R = the radius of the loading area.

3.6.2 J-integral calculation

In both the thermal shock experiments and the XFEM simulations, most cracks are perpendicular to the loading surface. To calculate J-integrals for these cracks, precracks are defined to be perpendicular to the loading surface. J-integrals are calculated at the end of cooling, and plastic strains at the end of cooling are considered to be initial strains. The direction of the virtual crack tip extension points into the sample. Length and location of precracks (see figure 3.47) are variables for a parametric study. To avoid the influence from other cracks, only one precrack is allowed in each calculation.

Figure 3.48 shows J-integral for precracks at different positions. At first J-integrals increase with the crack length up to a crack length of 0.1 mm, because stress does not decrease with increasing depth within a depth of 0.1 mm. Then, J-integrals decrease with increasing crack length due to the decrease of stress. The J-integral is smaller when the precrack is close to the axis of symmetry, since the driving force for crack opening is reduced at the crack surface close to the center due to axisymmetric modeling. Table 3.3 lists the crack opening displacement (COD) of precracks of 0.08 mm length. The COD shows the same tendency as the J-integral. In the thermo-mechanical simulations it is shown that a peak stress occurs near the edge of the loading area. However, there is no peak value of the J-integral near the edge of the loading area to be seen in figure 3.48, since the stress concentration is relaxed when a precrack is inserted near the edge of the loading area, and almost no stress is generated at the crack surface close to the bulk material outside the loading area, as the material is separated from the loading area by the precrack.

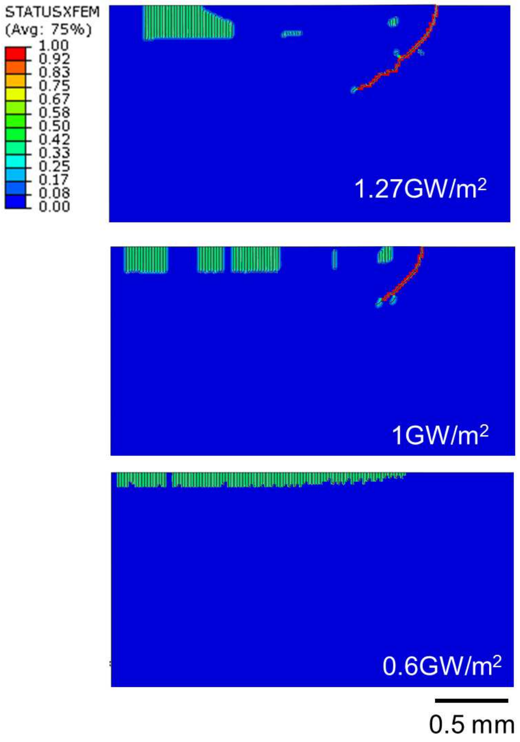

Figure 3.46: Cracks predicted using XFEM with multiple enriched features for different power densities and a base temperature of 20 °C.

Table 3.3: Crack opening displacement of precracks of 0.08 mm length.

Distance from the center (mm)	0.4	0.8	1.2	1.6	2.0	2.4
Crack opening displacement(µm)	7.5	7.78	7.69	7.41	5.42	1.03

Effects of power density and base temperature on J-integrals

In this part, a parametric study of base temperatures (20 °C to 800 °C) and power densities (0.3 GW/m^2 to 1.27 GW/m^2) serves to study their effects on the value of the J-integral. In order to predict cracking at different base temperatures, a temperature dependent critical value of the J-integral (J_c) is needed. Gludovatz et al. [61] measured the fracture toughness (K_{Ic}) of tungsten. However, at room temperature, the fracture toughness of rolled tungsten determined by Gludovatz et al. varies from 4.69 MPa$\sqrt{\mathrm{m}}$ to 9.08 MPa$\sqrt{\mathrm{m}}$ by changing the compact tension specimens to 3-point bending specimens [61]. As-sintered tungsten exhibits a fracture toughness of 5.1 MPa$\sqrt{\mathrm{m}}$ using compact tension specimens. The fracture toughness of polycrystalline tungsten rods at room temperature is 8.0±0.2 MPa$\sqrt{\mathrm{m}}$ for transverse and 12.6±1.3 MPa$\sqrt{\mathrm{m}}$ for longitudinal specimens[1] [64]. Hence, the fracture toughness of tungsten varies by at least a factor of two depending on both manufacturing

---

[1] For transverse specimens, the long axis is parallel to the swaging direction, while the long axis of longitudinal specimens is perpendicular to the swaging direction.

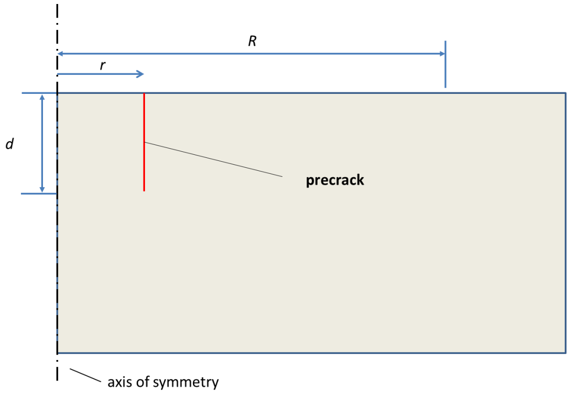

Figure 3.47: Precrack for the calculation of the J-integral.

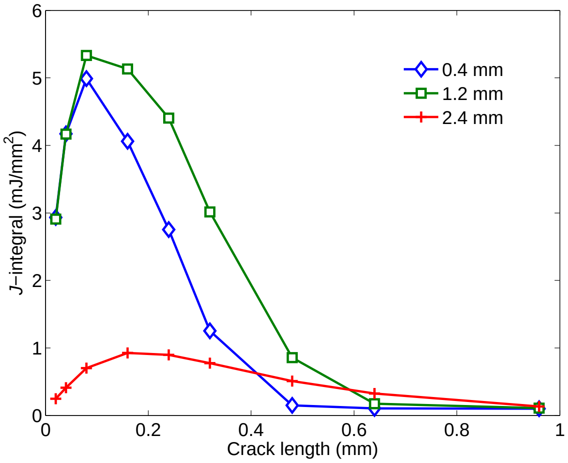

Figure 3.48: J-integral for a power density of 1.27 GW/m^2 and a base temperature of 20 °C. Different distances (0.4 mm, 1.2 mm and 2.4 mm) of the precrack from the center of the loading area are considered.

method of the tungsten samples and the testing procedure. Taking this span of values into account when deriving the critical value of J_c from the temperature dependent fracture toughness data determined by Gludovatz et al. [61] allows studying the impact of reported fracture toughness values and temperature on the cracking behavior.

Figure 3.49 shows values of the J-integral for different power densities and base temperatures. In these studies a precrack positioned 1.2 mm away from the loading center is chosen to represent a general situation in the central part of the loading area, because the precrack is situated far enough from both the axis of symmetry and the edge of the loading area. In general, the J-integral increases as power density increases. Higher base temperatures lead to smaller stresses. As a consequence, J-integrals are smaller, too. At low base temperatures (e.g. below 200 °C) and for power densities larger than 0.6 GW/m^2, the J-integrals are much larger than both values of J_c, which indicates that cracking can be hardly avoided at low base temperatures. However, since the fracture toughness of tungsten increases with increasing the temperature, the J-integrals calculated for a base temperature of 800 °C are much smaller than the critical value. Thus, high base temperatures are suitable to prevent crack opening. Nevertheless, one must keep in mind that increasing the base temperature will also lead to an increase in the equivalent plastic strain that describes the plastic deformation history. This in turn may cause material degradation and thermal fatigue failure. Other than that, a high base temperature might lead to a surface temperature that is close to or even higher than the melting point of tungsten so significantly degrading the structural integrity of the component.

Figure 3.50 shows the thermal shock behavior based on J_c gained from both the fracture toughness obtained by Gludovatz et al. [61]. 20 μm is assumed to be the crack length that can be developed from the initial defects along the grain boundaries without reaching the critical value of the energy release rate, since grain boundaries are more vulnerable than the grain interior. This assumption yields a slightly conservative estimation in cases that there are very few initial defects at the top surface of the tungsten sample near a stress concentration or the initial defects cannot grow to become a crack of 20 μm length. In figure 3.50, there are no essential changes concerning the cracking threshold even if the value of the fracture toughness assumed for computing J_c is doubled. This indicates that in order to avoid cracking of tungsten at low temperatures, the fracture toughness of tungsten needs to be improved significantly. The threshold power density is between 0.3 $\mathrm{GW/m^2}$ and 0.6 $\mathrm{GW/m^2}$, and the threshold base temperature is between 400 °C and 600 °C. The numerically predicted thresholds coincide roughly with the experimental observations [49], where the experimentally determined threshold power density is between 0.16 $\mathrm{GW/m^2}$ and 0.4 $\mathrm{GW/m^2}$ and the threshold base temperature is between 100 °C and 400 °C depending on the tungsten grade tested.

Deviations between the cracking thresholds obtained from the experiments and the J-integral calculations are to be expected, since the material data used in chapter may differ from the tungsten properties after thermal loadings - and also because the difference of material properties resulting from different fabrication processes is not included in the calculations. Furthermore, it should be noted that the thermal shock behavior obtained from the experiments considers 100 thermal shocks. The evolutions of microstructure and material parameters with the thermal cycles, which are not taken into consideration in the J-integral calculation, may also influence the results.

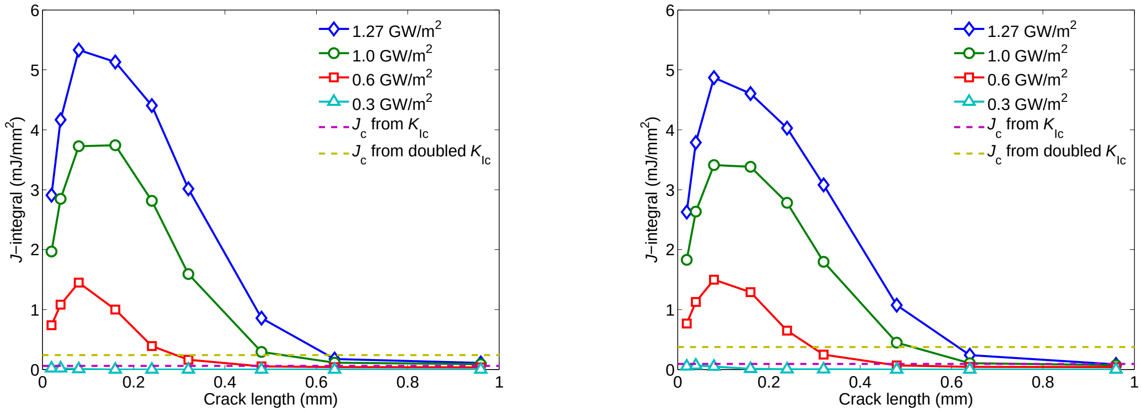

(a) base temperature 20 °C (b) base temperature 200 °C

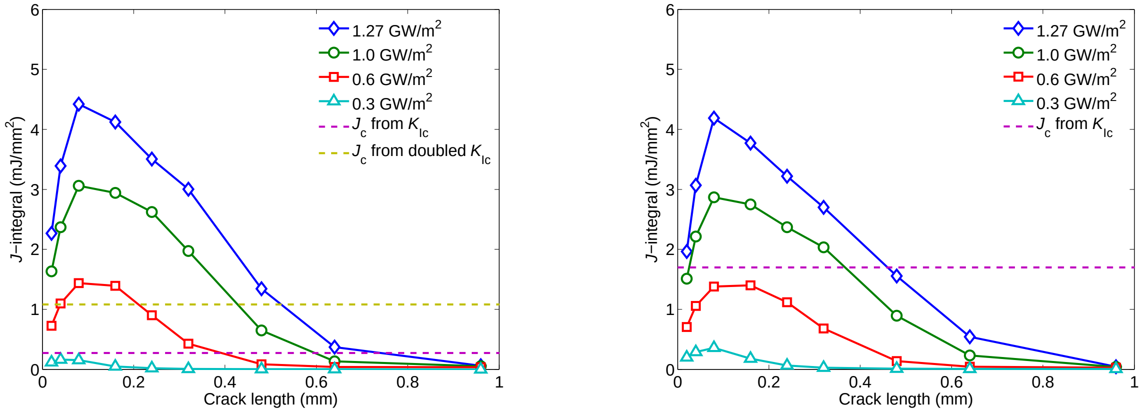

(c) base temperature 400 °C (d) base temperature 600 °C

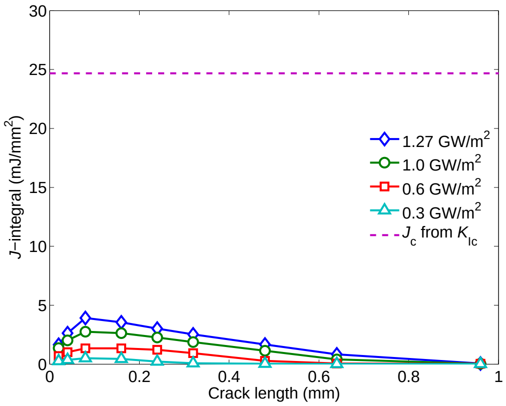

(e) base temperature 800 °C

Figure 3.49: J-integral for power densities of 0.3-1.27 GW/m^2 and base temperatures of 20 °C-800 °C. The precrack is set 1.2 mm away from the center. The value of J_c determined from the doubled fracture toughness are larger than the upper scale of the plots for base temperatures of 600 °C and 800 °C, and are, therefore, not shown in plots (d) and (e).

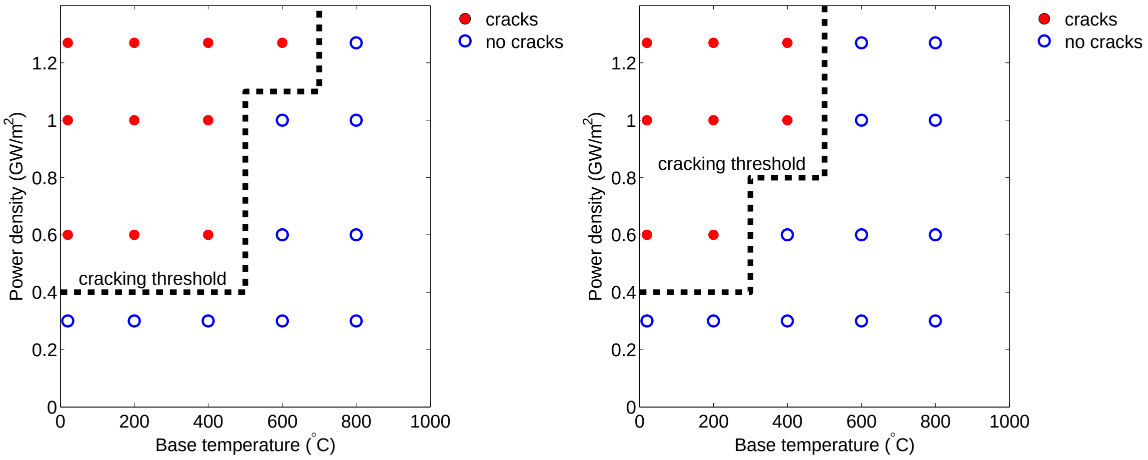

Figure 3.50: Thermal shock behavior of tungsten samples calculated by comparing J-integrals with J_c gained from both the fracture toughness obtained by Gludovatz et al. [61] (left) and its doubled value (right).

3.7 Effect of high heat flux loading pattern

Numerical investigations were conducted based on the thermal shock experiments at Forschungszentrum Jülich in which a homogenous thermal loading was achieved by fast scanning of the sample surface with the electron beam. Other than thermal shock experiments using electron beam, in the literature there are ample experimental reports on the damage behavior of tungsten under ELM-like thermal loads where thermal loads were simulated using various kinds of energy sources (plasma, laser) [65, 66]. In these thermal shock experiments or actual divertor operation, the pulse of a heat flux load can have different temporal and/or spatial profiles for a given energy deposit. In this regard, there is still open question as to how the high heat flux loading pattern affects cracking feature under ELM-like loading conditions, and this is the topic of the this section.

3.7.1 Loading patterns

Six HHF loading patterns are considered as combinations of three spatial profiles and two different temporal scenarios. The different spatial profiles are uniform, a triangle with a steep slope and a triangle with a gradual slope (see figure 3.51). The triangular energy distribution is used as a rough estimate of a Gaussian profile, which is the typical energy distribution on the target material for a static electron beam. The power density of the uniform loading, F, is 0.8 GW/m^2. The two temporal scenarios are either a constant or a ramp loading (see figure 3.52). For the constant loading, the power density is constant throughout the loading time, while for the ramp loading, the power density starts from zero and keeps increasing to the same power density of the constant loading at the end of the loading time. When the power is turned off, the power density is assumed to be reduced to zero immediately for both temporal scenarios. The duration of the constant loading is 1 ms, and the duration of the ramp loading is 2 ms. The base temperature is 20 °C. All six HHF loading patterns employ the same total energy input within the corresponding loading time.

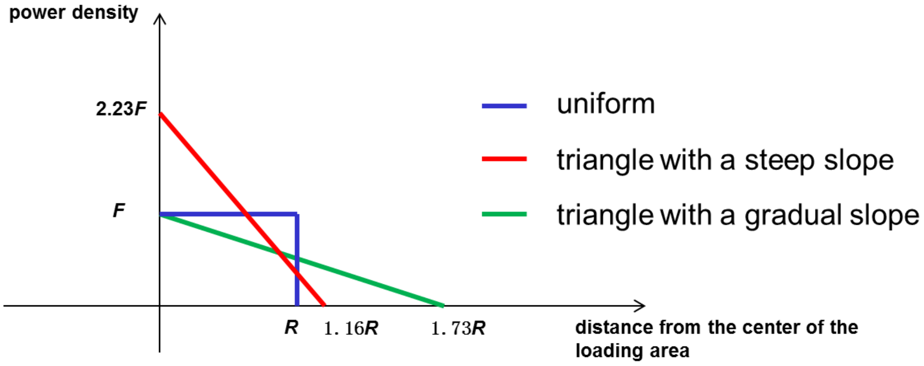

Figure 3.51: Considered spatial profiles of the power density at the surface of the axisymmetric model, F: the power density for the uniform loading, R: the radius of the loading area for the uniform loading.

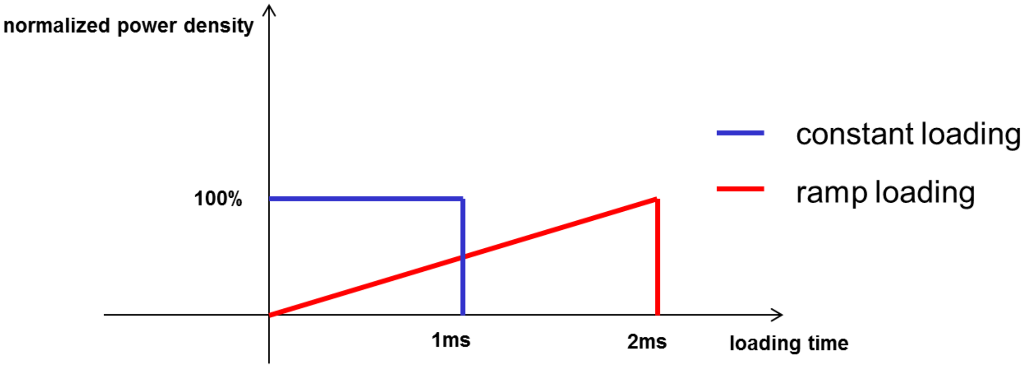

Figure 3.52: Different temporal scenarios considered.

3.7.2 Effect on temperature distribution

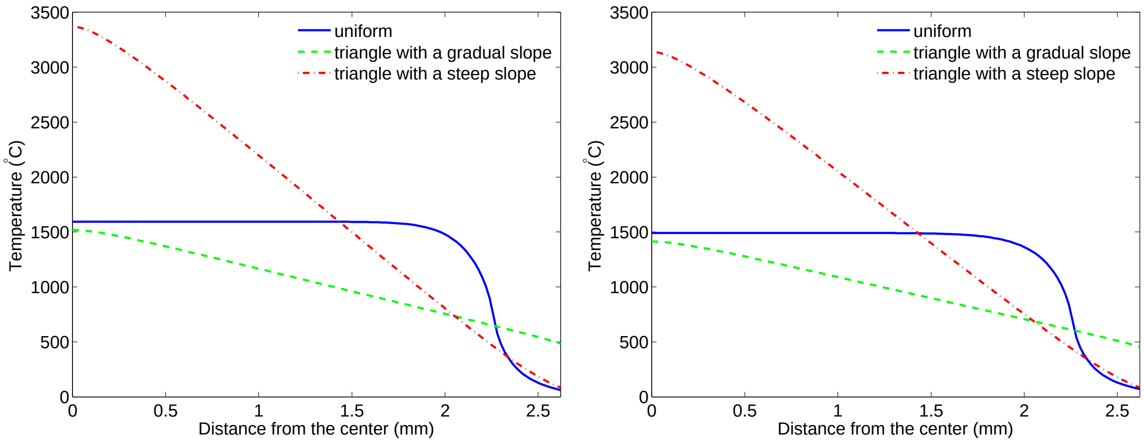

Figure 3.53: Surface temperature at the end of heating for the constant (left) and the ramp (right) loadings for three energy distributions.

Figure 3.53 shows the surface temperature for different loadings at the end of heating. The surface temperature profile is similar to the energy distribution at the surface, which indicates that the surface temperature is proportional to the power density. The triangular loading with a steep slope generates the largest peak temperature at the surface in comparison to the other two energy distributions. In general, the surface temperature for the ramp loading scenario is slightly smaller than what is predicted for the constant loading. This is due to the fact that the ramp loading entails longer loading times, so more energy is dissipated into the bulk material during heating. The difference in peak temperature between the constant and the ramp loading scenarios is the largest for the triangular loading with a steep slope. With this energy distribution, the peak temperature is 3142 °C for the ramp loading scenario, while the peak temperature for the constant loading scenario is 3371 °C. The difference is reduced with decreasing power density. For the triangular loading with a gradual slope or the uniform loading, the difference of the peak temperatures is less than 100 °C between the constant and the ramp loading scenarios.

3.7.3 Effect on stress and strain distribution

In figure 3.54, surface plastic strain in radial direction is shown at the end of heating. The distribution of plastic strains at the surface is similar to the corresponding energy distribution. The maximum magnitude of plastic strain in radial direction for the triangular loading with a steep slope is approximately four times that for the uniform loading and the triangular loading with a gradual slope, while the peak temperature is only about two times as high, see figure 3.53. This is because the coefficient of thermal expansion is larger at higher temperatures. Thus, larger plastic deformation is generated for the same temperature increase at a higher temperature.

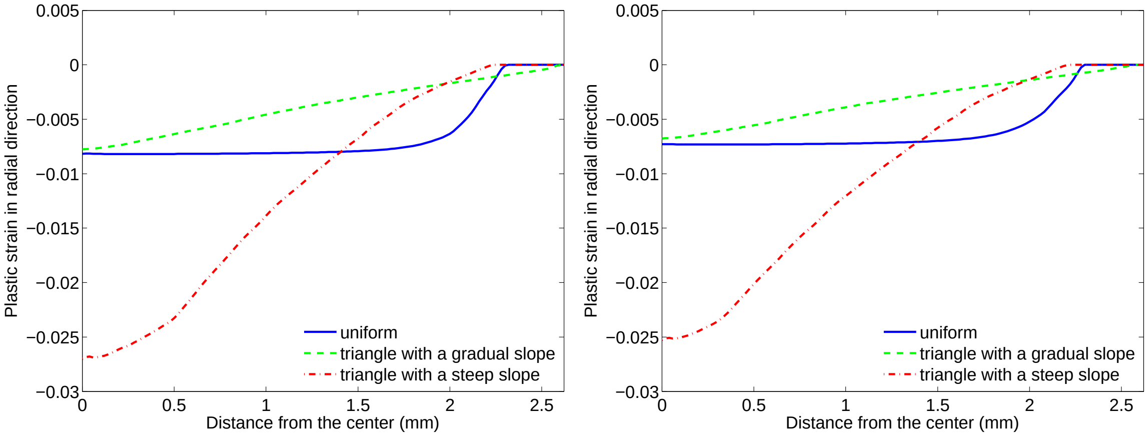

Figure 3.54: Surface plastic strain in radial direction at the end of heating for the constant (left) and the ramp (right) loadings for three energy distributions.

Figure 3.55 shows the surface plastic strain in radial direction at the end of cooling. The magnitude of plastic strain for different loadings is reduced to a similar level in the central part of the loading area during cooling.

In figure 3.56, surface stress in radial direction is shown at the end of cooling. For all six cases, the distributions of the surface stresses in radial direction are also similar, alike to the plastic strains. The peak stress in radial direction appears 1.5 to 2.3 mm away from the center of the loading area depending on the energy distribution. Of all energy distributions, the triangular loading with a steep slope results in the largest peak stress in radial direction. At the center of the loading area the stress in radial direction is slightly larger for the triangular loading with a gradual slope than for the other two energy distributions. For ramp loading scenarios, the peak stress in radial direction of the triangular loadings occurs closer to the center of the loading area than for the constant loading scenarios. Figure 3.57 shows the stress in radial direction at a depth of 0.2 mm at the end of cooling.

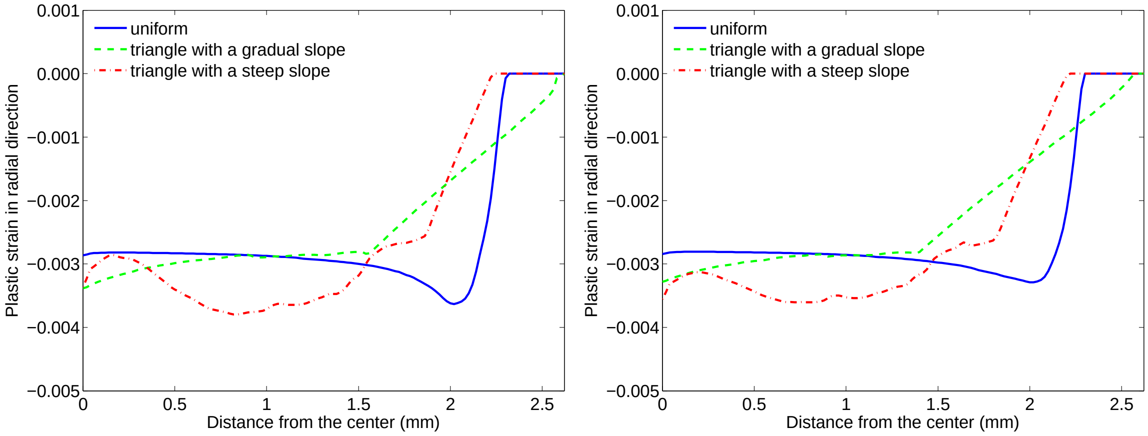

Figure 3.55: Surface plastic strain in radial direction at the end of cooling for the constant (left) and the ramp (right) loadings for three energy distributions.

Although the stresses in radial direction for the six HHF loading patterns are similar at the surface, the stress in radial direction for the triangular loading with a steep slope is much larger than for loadings with the other two energy distributions at a depth of 0.2 mm.

As for the thermal distribution, the difference of stress and strain distributions between the constant and the ramp loading scenarios is moderate. If a strain rate dependent yield stress is considered in the calculation, the results may be influenced. However, considering that the difference of the loading duration and the similarity of the plastic strain distribution at the end of heating, the strain rate for the constant scenarios is roughly twice the strain rate for the ramp loading scenarios, which indicates that the difference of the yield stress resulting from the difference of strain rate is negligible. This finding is based on the data listed in literature [67].

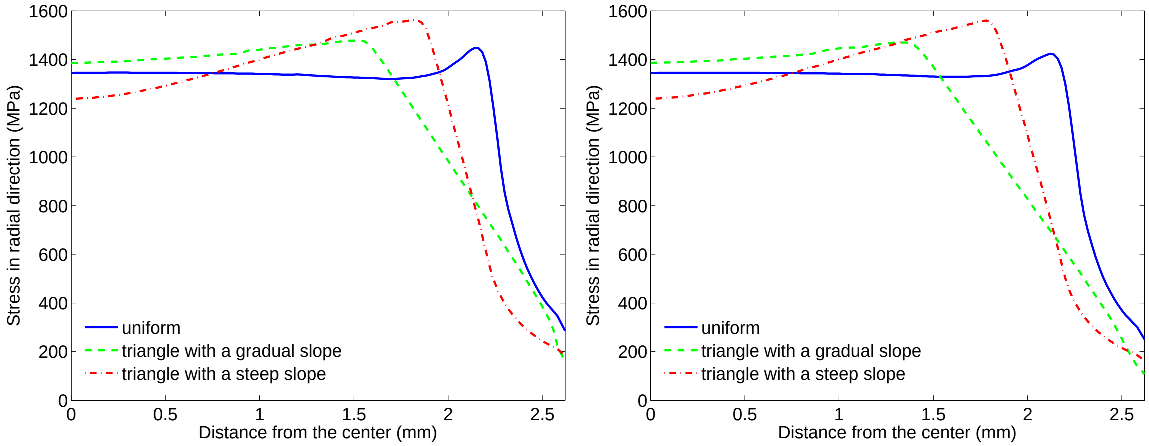

Figure 3.56: Surface stress in radial direction at the end of cooling for the constant (left) and the ramp (right) loadings for three energy distributions.

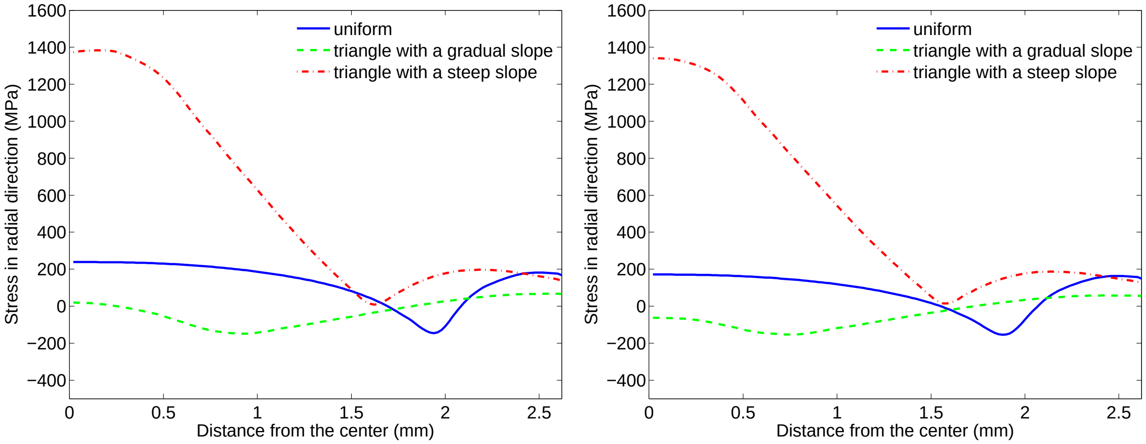

Figure 3.57: Stress in radial direction at a depth of 0.2 mm at the end of cooling for the constant (left) and the ramp (right) loadings for three energy distributions.

3.7.4 Effect on fracture behavior

XFEM simulation

To compare the fracture behavior of tungsten for different HHF loading patterns, XFEM simulations of six HHF loading patterns were performed.

In figure 3.58, cracks are predicted using XFEM for different loadings. In these XFEM simulations, no precracks are assumed, and multiple crack initiation is allowed. Cracking patterns resulting from the constant and the ramp loadings are similar, while the cracking patterns resulting from the uniform and the triangular loadings differ. For the uniform loading, there are many short cracks that appear in the loading area at the top surface and which propagate perpendicularly to the loading surface. Near the edge of the loading area, a crack is generated which propagates parallel to the loading surface. For the triangular loading, cracks mainly propagate perpendicularly to the loading surface, while the cracks resulting from the triangular loading with a steep slope are much longer than those resulting from the triangular loading with a gradual slope.

The occurrence of multiple cracks can influence the initiation of other potential cracks by relaxing the stress concentration. In order to study a crack initiated at a specific position without any influence from other cracks, XFEM simulations were conducted with a single precrack, and no other crack initiation was allowed. As the constant and the ramp loading scenarios result in similar cracking patterns, only the constant loadings were studied here. Figure 3.59 shows results of these XFEM simulations with a single precrack at different positions for three energy distributions. In each simulation, a precrack of 40 μm was assumed be oriented perpendicular to the loading surface. In the central part of the loading area, the precracks generally propagate perpendicularly to the loading surface for all three energy distributions. The crack length resulting from the triangular loading with a steep slope is the largest, due to the fact that its maximum power density is the largest. For the triangular loading with a steep slope and a precrack positioned 2.01 mm from the center of the loading area makes it propagate parallel to the loading surface, i.e. deviate from its initial vertical path. A similar crack is found 2.23 mm away from the center of the loading area for the uniform loading. For the triangular loading with a gradual slope, the precrack 1.61 mm away from the center of the loading area tends to propagate towards the center of the loading area, but the driving force is not large enough for significant crack growth.

As shown in figure 3.59, cracks are found near the position where the peak stress occurs for the uniform and triangular loadings with a steep slope (XFEM simulations with a single precrack). These cracks propagate parallel to the loading surface. However, cracks do not propagate parallel to the loading surface for the triangular loading with a steep slope, if multiple crack initiations are allowed, see figure 3.58. This is due to the stress relaxation resulting from the crack opening in the central part of the loading area. To confirm this conclusion, the XFEM simulations were made with two precracks at specific positions. One precrack was defined in the central part of the loading area (d = 0.81 mm) while the other precrack was defined near the position where the peak stress occurs. The results of these calculations are shown in figure 3.60. Crack propagation parallel to the loading surface is hindered as crack opening occurs in the central part of the loading area. This indicates that for power densities sufficiently large to induce cracking in the central part of the loading area, crack growth parallel to the loading surface will be impeded. If the power density is too small, no cracking will occur. For the aforementioned reasons the cracking pattern predicted for the uniform loading in figure 3.58 occurs within a certain range of the power density, which allows the occurrence of the cracks near the edge of the loading area but does not lead to serious cracking in the central part of the loading area. This cracking pattern should be avoided, since it may lead an undesired concentration of thermal energy at the top surface and subsequent melting or erosion of surface material.

Compared to the triangular loading, the uniform loading is more likely to cause a crack near the position where the peak stress occurs and which will grow parallel to the loading surface. On one hand, the distance between the position of peak stress and the loading center is larger for the uniform loading than for the triangular loading, which indicates that the growth of cracks near the edge of the loading area is less influenced by cracking in the central part, see figure 3.60. On the other hand, the uniformly distributed stress distribution under the uniform loading can create many short cracks in the central part of the loading area at the same time, which reduces the driving force for a long crack, see figure 3.58.

J-integral calculation

The J-integral is calculated for precracks of various lengths at different positions in order to compile a parametric study, see figure 3.61. In each calculation, a single precrack is defined with a fixed length. The critical value of the J-integral (J_c) is assumed to be the same as the fracture energy used in the XFEM simulations. The direction of the virtual crack tip extension is downwards and perpendicular to the loading surface.

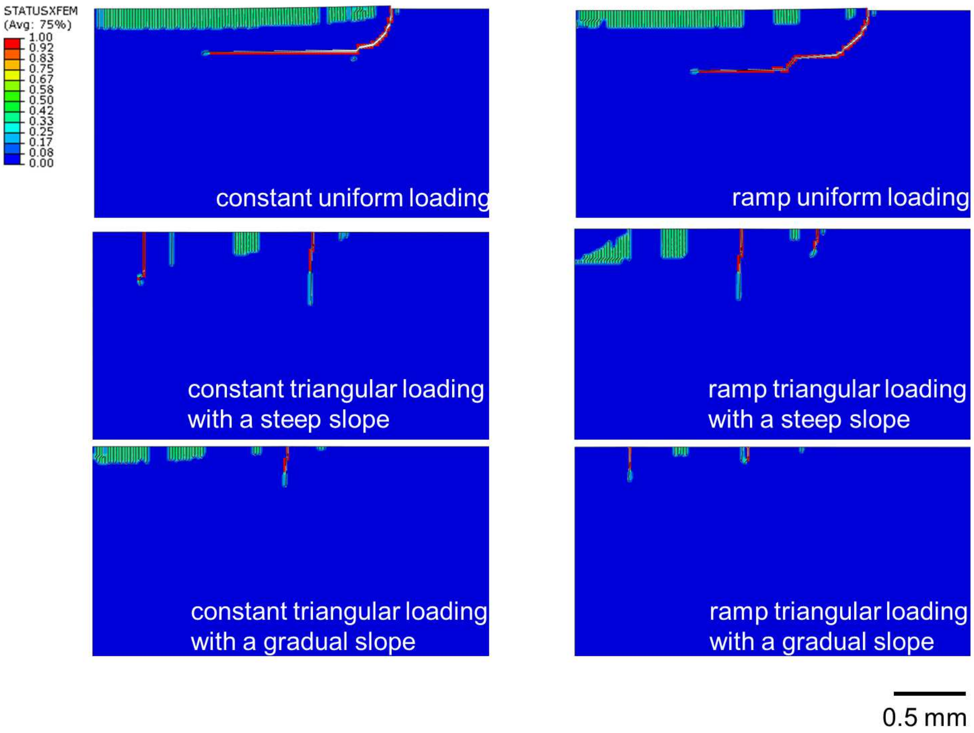

Figure 3.58: Cracks predicted using XFEM without any precracks for six HHF loading patterns.

In figures 3.62, 3.63 and 3.64 J-integrals are shown for the six HHF loading patterns. In all six loading cases, the J-integrals for precracks in the central part of the loading area (d = 0.81 mm) are larger than the critical value, which coincides with the XFEM prediction. The J-integrals for the ramp loading scenarios are slightly smaller than for the constant loading scenarios. For the triangular loading with a steep slope, the J-integrals for precracks in the central part of the loading area are much larger than for the uniform and the triangular loading with a gradual slope. The crack length of the longest precrack, for which the J-integral is larger than its critical value, is defined as the maximum crack length. The maximum crack length for the triangular loading with a steep slope is the largest (approx. 0.6 mm), while the maximum crack length for the triangular loading with a gradual slope is less than 0.3 mm. For the uniform loading and the triangular loading with a steep slope the J-integral for the precrack - which is 2.0 mm away from the center of the loading area - is larger than the critical value and thus a sufficient driving force is provided for crack propagation. For the triangular loading with a gradual slope, J-integrals for precracks 2.0 mm away from the center of the loading area are smaller than the critical value. This result coincides with the XFEM prediction that no crack growth occurs 2.0 mm away from the center of the loading area for the triangular loading with a gradual slope.

The most probable crack propagation direction is the direction in which the energy release rate is the largest. In figures 3.65, 3.66 and 3.67, the direction of the maximum energy release rate (indicated

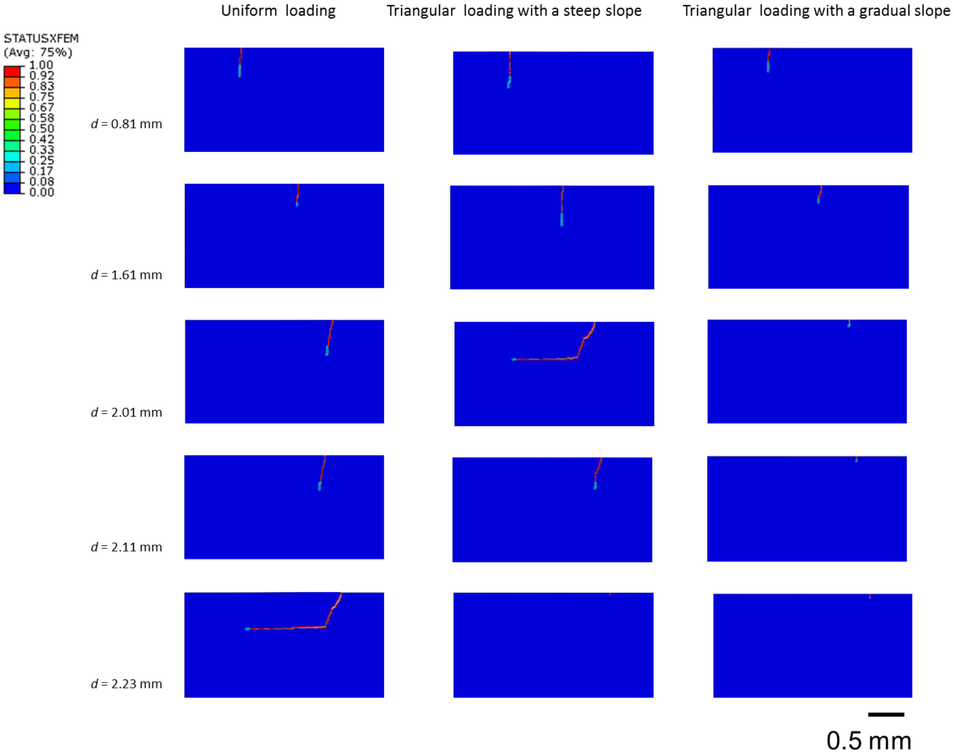

Figure 3.59: Crack predicted using XFEM assuming a single precrack at different locations for three energy distributions.

by the angle φ in figure 3.61) of precracks of different lengths are shown for constant loadings with different energy distributions. In general, for a small crack length (0.04 mm), the angle is smaller than 10 °. This is due to the fact that within the surface layer the tensile stress is much larger than the shear stress. The angle increases as crack length increases. For the uniform loading, the angle increases significantly as the precrack is closer to the edge of the loading area. For the triangular loading with a steep slope, the maximum value of the angle occurs for a precrack about 2.0 mm away from the center of the loading area, where the crack propagates parallel to the loading surface (see the XFEM simulations in figure 3.59). For the triangular loading with a gradual slope, the energy release rate is smaller than its critical value, even though the angle of a crack of 0.32 mm length is about 40 °. As a result, no crack parallel to the loading surface can be found for the triangular loading with a gradual slope, while the crack near the position where the peak stress occurs does propagate parallel to the loading surface by kinking from its initial vertical path for the triangular loading with a steep slope and the uniform loading. This matches with the XFEM predictions shown in figure 3.59. However, it is should be noted that minor differences are to be expected between the direction of the maximum energy release rate calculated using the VCE method and the direction of crack propagation from the XFEM simulations. One reason is that the direction of the maximum release rate is calculated at the end of cooling, while the direction of crack propagation is calculated

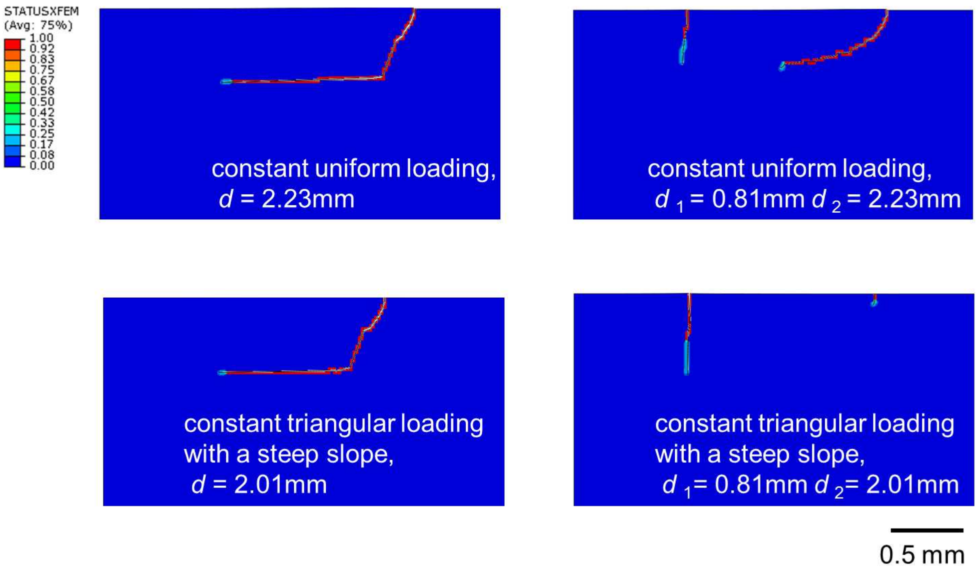

Figure 3.60: Cracks predicted using XFEM with two precracks assumed.

during the cooling.

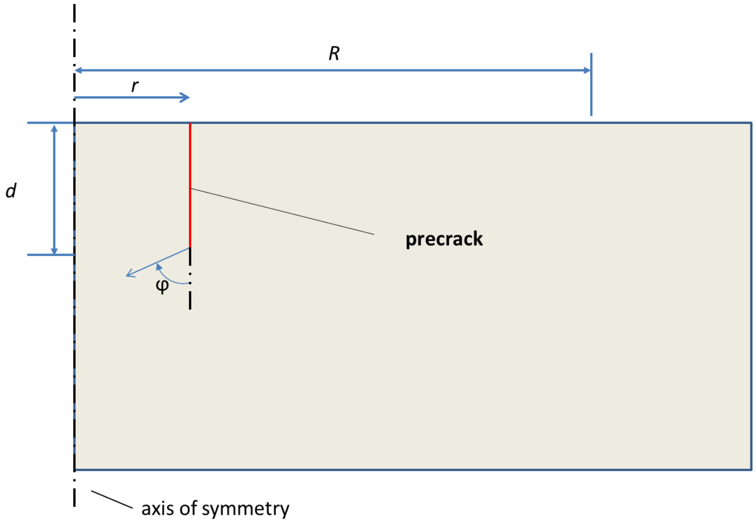

Figure 3.61: Precrack definition for the J-integral calculation. φ indicates the direction of the maximum energy release rate.

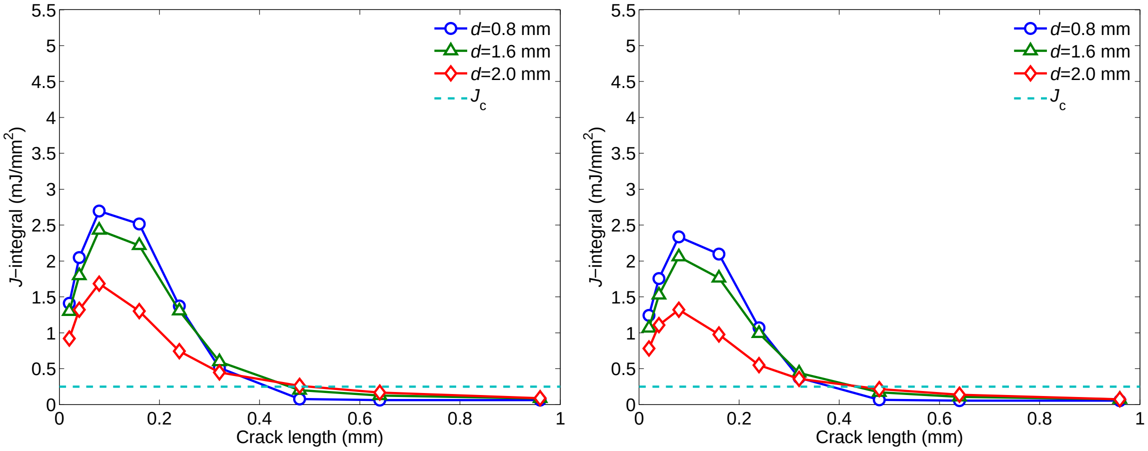

Figure 3.62: J-integral for the constant (left) and the ramp (right) uniform loadings.

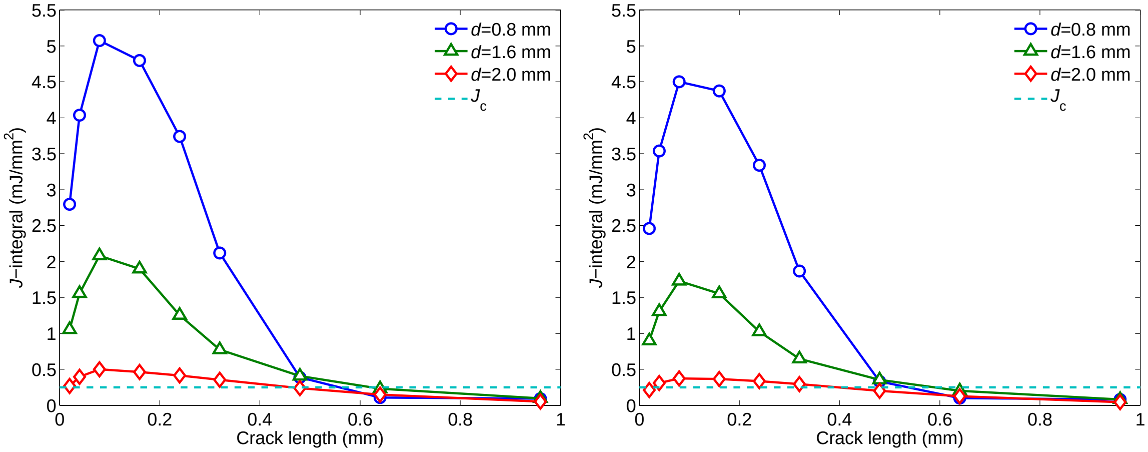

Figure 3.63: J-integral for the constant (left) and the ramp triangular (right) loadings with a steep slope.

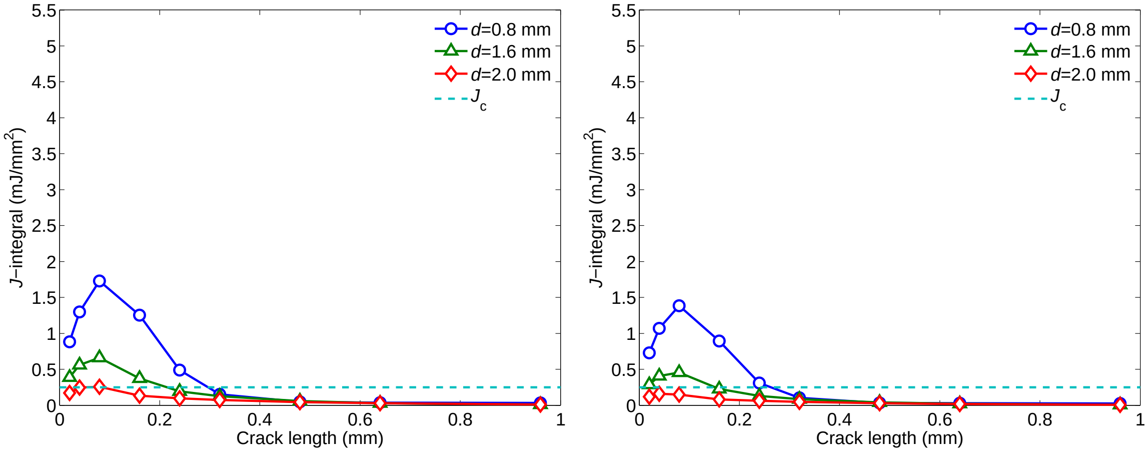

Figure 3.64: J-integral for the constant (left) and the ramp triangular (right) loadings with a gradual slope.

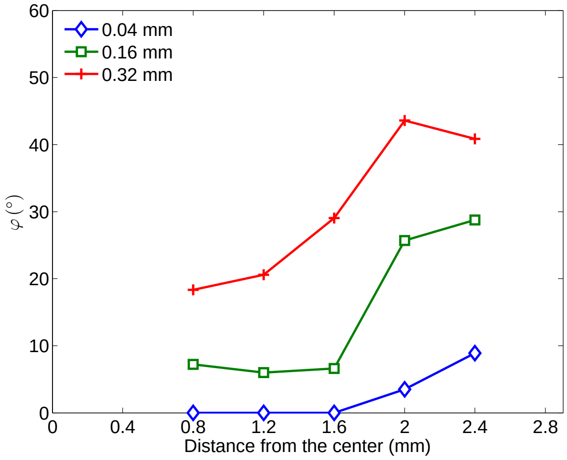

Figure 3.65: Direction of the maximum energy release rate represented by the angle φ of precracks of different lengths for the constant uniform loading.

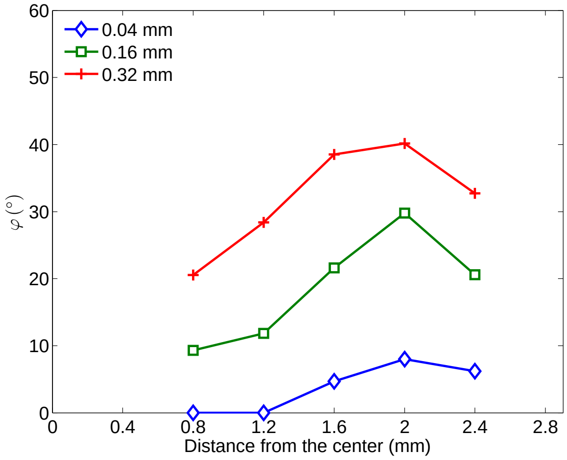

Figure 3.66: Direction of the maximum energy release rate represented by the angle φ of precracks of different lengths for the constant triangular loading with a steep slope.

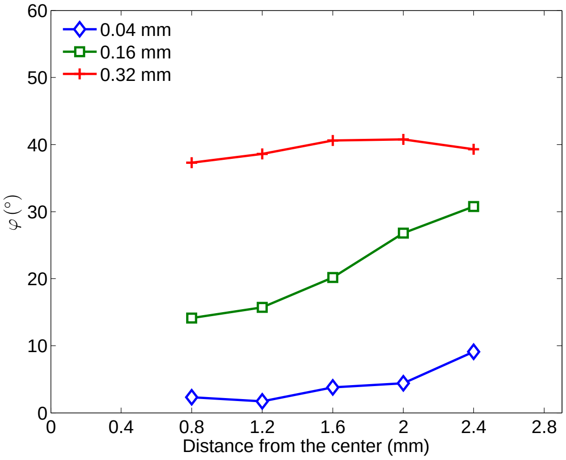

Figure 3.67: Direction of the maximum energy release rate represented by the angle φ of precracks of different lengths for the constant triangular loading with a gradual slope.

3.8 Summary

This chapter focused on a fracture mechanics analysis of tungsten under short transient thermal loads by ELMs, based on analytical and numerical calculations.

It was assumed that the solution assuming a semi-infinite space can give a good estimation of the behavior of tungsten in the central part of the loading area in the ELM-like thermal shocks tests, since the loading was nearly homogenous in the loading area. As a result, a simplified analytical solution was derived to capture the temperature, strain and stress distributions in a semi-infinite space. This analytical solution matched the numerical solution very well. By introducing the weight function of a semi-infinite space solution, the stress intensity factor was calculated for the prospective crack. Generally, the failure map based on the comparison of stress intensity factors and fracture toughness coincided with the experimental observations.

Other than analytical estimations, a comprehensive computational study of thermo-mechanical and fracture behaviors of tungsten under ELM-like thermal shocks was presented. A series of parametric simulations were conducted using an axisymmetric model based on elasto-plastic finite element analysis. The effects of power density and base temperature on the temperature, stress and strain distributions were evaluated. Based on the thermal simulations, a failure modeling on tungsten under ELM-like thermal shocks was conducted. Crack initiation and propagation were simulated using XFEM, while the J-integrals, which represent the energy release rate at crack tips, were evaluated using the FEM-based VCE method. The following features of tungsten behavior were found under ELM-like thermal shocks:

1. Upon cooling, tensile stress develops in the loaded surface layer as a consequence of plastic flow, coined as residual stress at the end of the cooling process. The radial component of tensile stress shows its maximum peak at the boundary of the loading area. At this position, a crack most probably first propagates in vertical direction, followed by a gradual horizontal kinking, parallel to the loading surface. Such cracking characteristics are typical for a power density of $1\,\mathrm{GW/m^2}$ and higher.

2. There is a threshold value of the heat flux load above which significant plastic flow takes place during both heating and cooling - and above which almost identical plastic strain and tensile stress are generated at the end of cooling. This threshold ranges between $0.3\,\mathrm{GW/m^2}$ and $0.6\,\mathrm{GW/m^2}$ at a base temperature of $20\,^\circ\mathrm{C}$.

3. The maximum peak value of the tensile residual stress (radial component) increases as the power density of the heat load is increased.

4. When the critical stress for crack initiation is reduced, many small cracks are formed in perpendicular direction to the surface over the whole loading area, especially in the central region. Once these cracks are initiated and continue to grow in the central part, the driving force for cracking near the boundary of the loading area is reduced.

5. The crack formation is predicted for the power density of 0.6 GW/m^2 and above, and when the base temperature is higher than 600 °C, almost no crack is predicted.
6. The predicted threshold values of power density and base temperature for cracking agree roughly with the experimental observations. There are no essential changes concerning the cracking threshold even if the value of fracture toughness assumed for the simulation is increased by a factor of two.

The last part of the chapter dealt with the influence of loading patterns of ELM-like transient thermal loads on the fracture behavior of tungsten. Comparative assessment of initial cracking and crack growth was conducted for six HHF loading patterns (combinations of three spatial and two temporal variants) assuming the same deposited energy for all cases. Several distinct effects were found.

1. A ramp pulse with a longer duration leads to lower temperatures and stresses in comparison to a constant pulse with a shorter duration. Yet, the difference is moderate when both their maximum power density and total deposited energy are identical. No significant deviation of cracking between these two temporal loading scenarios can be observed.
2. Cracks in the central part of the loading area are initiated in perpendicular orientation to the surface. The final length of these cracks is dependent on the applied power density. Thus, the length of the crack produced under the triangular loading profile with a steep slope is larger than those of the triangular profile with a gradual slope and of the uniform distribution.
3. Regardless of the thermal loading distribution, cracks produced near the position where the peak stress occurs tend to kink from their initial vertical path at a certain depth (e.g. 0.32 mm) and grow further in parallel to the surface.
4. Cracks initiated near the position where the peak stress occurs are more likely to grow further in parallel to the surface under the uniform loading, compared to the triangular loading.

Chapter 4

Fracture mechanics analysis of tungsten under slow high-energy-deposition thermal loads

4.1 Vertical displacement events

Besides the ELMs, PFCs will have to withstand slow high-energy-deposition thermal loads, which are characterized by a significantly longer duration than the ELMs. Vertical displacement events (VDEs) are a typical example for such events. A VDE is an uncontrolled growth of the plasma unstable vertical mode. The plasma has a tendency to be inherently instable and consequently effecting small vertical displacements due to the non-circular cross-section of the plasma confinement. Although, during operation of the fusion reactor, the plasma is always vertically controlled, such uncontrolled growths can occur for various reasons, for example [68]:

- fast disturbances acting on a time scale which is outside the control system bandwidth;
- delays in the control loop;
- wrong control action due to measurement noise, when plasma velocity is almost zero.

As a result, the plasma can then move vertically up or down and - in extreme cases - even contact with the vessel wall, which leads to a high-energy-deposition thermal loading on the PFCs. The typical pulse duration of VDEs ranges from 100 to 300 ms [69], which is nearly three magnitudes higher than the pulse duration of the ELMs. Such an event with deposited energy densities of 60 MJ/m^2 will cause the PFC's surface to melt and entail a loss of the PFM, which were observed in the VDE tests on water-cooled PFCs with active cooling of the heat sink performed by Linke et al. [69]. For analytical evaluation, Cardella et al. [70] have calculated the amount of melted and evaporated material, taking into account the evolution of the evaporated and melted layer and in order to assess possible effects of local temporary loss of cooling. Due to severe surface melting, erosion and substantial damage on the PFCs, only a few of these events can be tolerated. Thus, special measures must be taken so that no melting of the PFMs occurs or the melted PFMs under the VDEs do not lose their functionality. However, it is currently difficult to predict the VDEs in detail because of its uncertainty. Nevertheless, assuming there is a way to limit the thermal loading induced by the VDEs to an area that is sufficiently small, the temperature will not exceed the melting point of tungsten. In this sense, it is also of interest to assess the material behavior in this limited loading area. In this chapter, the thermo-mechanical and fracture behaviors of tungsten under VDE-like thermal loads are studied assuming no melting occurs. The numerical model is built according to the thermal shock experiments at Siemens Healthcare, where the VDE-like thermal load is loaded in a small spot.

4.2 Thermal shock experiments at Siemens Healthcare

4.2.1 Experimental setting

Plasma-facing components in future fusion devices will be subjected to intense thermal loads. To investigate these thermal loads experimentally, electron beam facilities (e.g. JUDITH, Jülich, Germany; FE-200, Le Creusot, France) are used frequently [71]. In X-ray tubes, the tungsten anode is subjected to similar thermal loadings, since X-rays are emitted by accelerating high energy electrons onto the anode material. The experimental facility involved in this dissertation (as shown in figure 4.1) is set up at Siemens Healthcare and is used to study the failure of tungsten anodes in X-ray tubes. Thus, the research results are expected to be beneficial for the design of both fusion devices and X-ray tubes (see [72] for details). Tungsten samples used in the experiments were made of rolled tungsten delivered by PLANSEE AG, Austria. The sample size was 27.5 mm × 27.5 mm × 3 mm. The surface of the samples was polished before the electron beam exposure. The focal spot of the electron beam is roughly a rectangle of 1223 μm × 271 μm. The test positions lie on a circle with a radius of 11.5 mm, and the angle between two neighboring test positions is $17\,^{\circ}$. Numerical simulations have shown that, for an individual test position, the impact resulting from the electron beam exposure of the neighboring test position is negligible. The samples were loaded with single thermal loads of power densities between 0.374 GW/m^2 and 0.624 GW/m^2, which is in the range of power densities of the VDEs loads in ITER. The power density in this chapter denotes the averaged absorbed power density in the loading area. The acceleration voltage was 65 kV and the tests were performed at room temperature. After the electron beam loading of 0.5 s, the sample was cooled to room temperature.

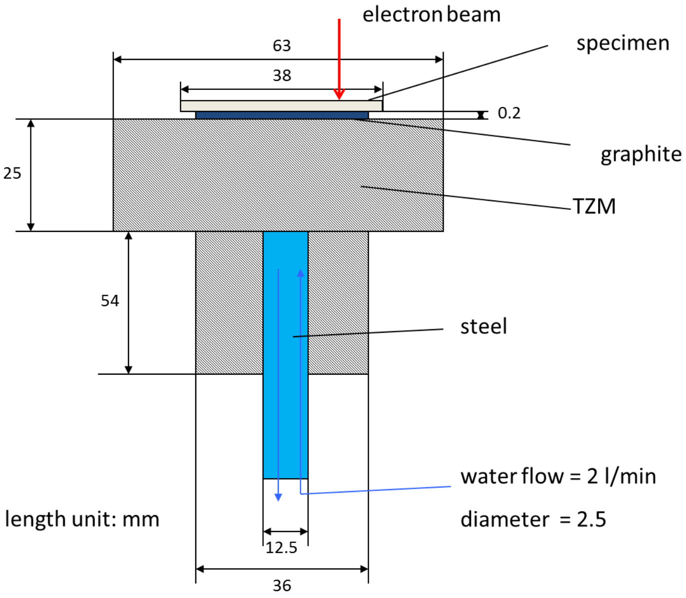

Figure 4.1: Schematic drawing of the cutting surface of the experimental facility at Siemens Healthcare. TZM refers to molybdenum alloy containing (in mass%) 0.50 titanium, 0.08 zirconium and 0.02 carbon.

4.2.2 Experimental observation

In order to confirm the numerical simulation results, the surface roughness was measured on the tested samples after cooling down from thermal shocks. The measurement was conducted using a Keyence three-dimensional Laser Scanning Microscope. Figures 4.2, 4.3 and 4.4 show Laser Scanning Microscopic (LSM) images as well as out-of-plane deformation images. To enhance the detail perceptibility of the out-of-plane deformation images, a factor of 20 is applied for the deformation. After the thermal loading, surface elevation results from the volume compensation to the inplane plastic deformation, which is shown in the following mechanical simulations. As power density of the electron beam increases, the surface elevation increases.

In LSM images, grain growth in the loading area is observed for thermal loads of 0.5 GW/m^2 and 0.624 GW/m^2. The grain growth is due to recrystallization at the sample surface. The recrystallization temperature of tungsten is between 1100 °C and 1400 °C [8]. The maximum temperatures measured for thermal loads of 0.374 GW/m^2, 0.5 GW/m^2 and 0.624 GW/m^2 are 1250 °C, 1880 °C and 2550 °C, respectively. The maximum temperatures for thermal loads of 0.5 GW/m^2 and 0.624 GW/m^2 are much higher than the recrystallization temperature of tungsten. As a result, recrystallization occurs in the loading area, although the high temperature only lasts for 0.5 s.

For a thermal shock load of 0.374 GW/m^2, no crack is observed at the sample surface. Tiny cracks occur under a thermal shock load of 0.5 GW/m^2. For a thermal shock load of 0.624 GW/m^2, there is a clear crack opening along the grain boundaries.

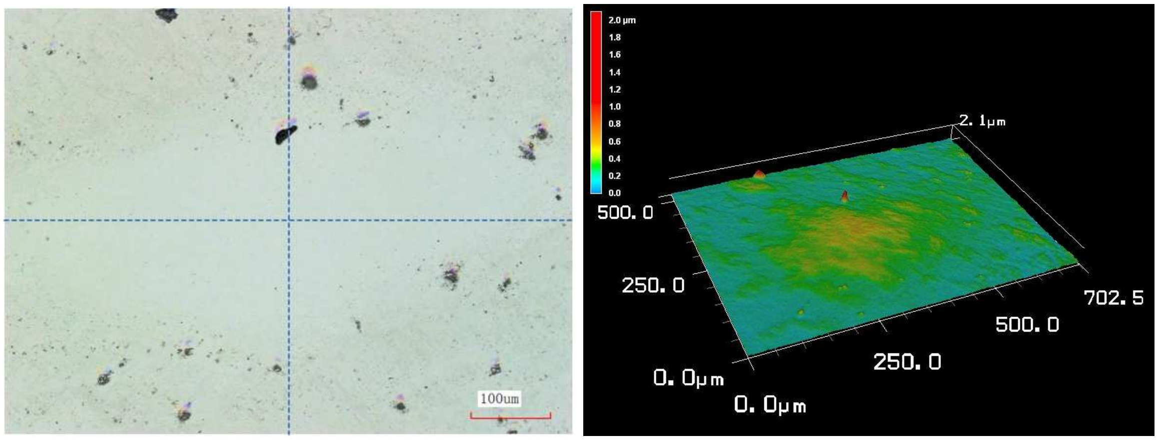

Figure 4.2: LSM and out-of-plane deformation images of the sample surface for a thermal shock load of 0.374 GW/m^2.

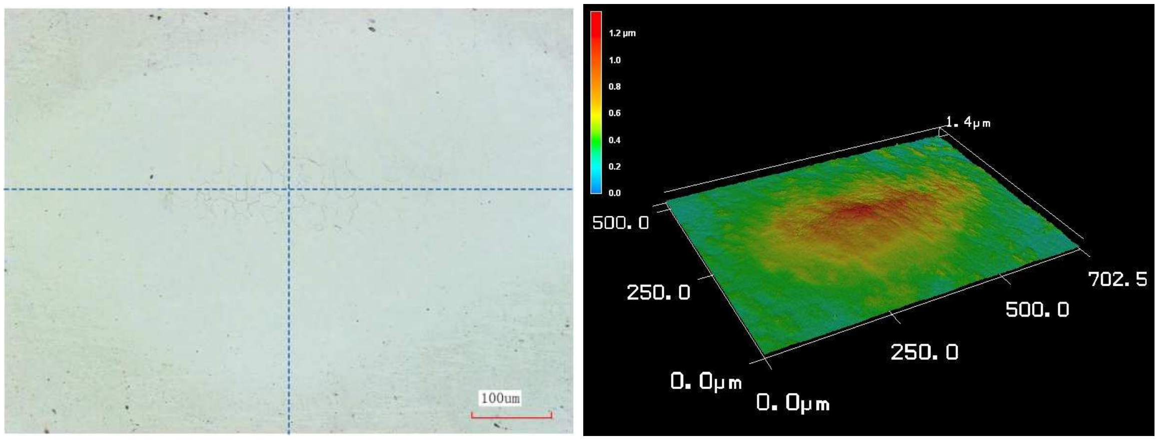

Figure 4.3: LSM and out-of-plane deformation images of the sample surface for a thermal shock load of 0.5 GW/m^2.

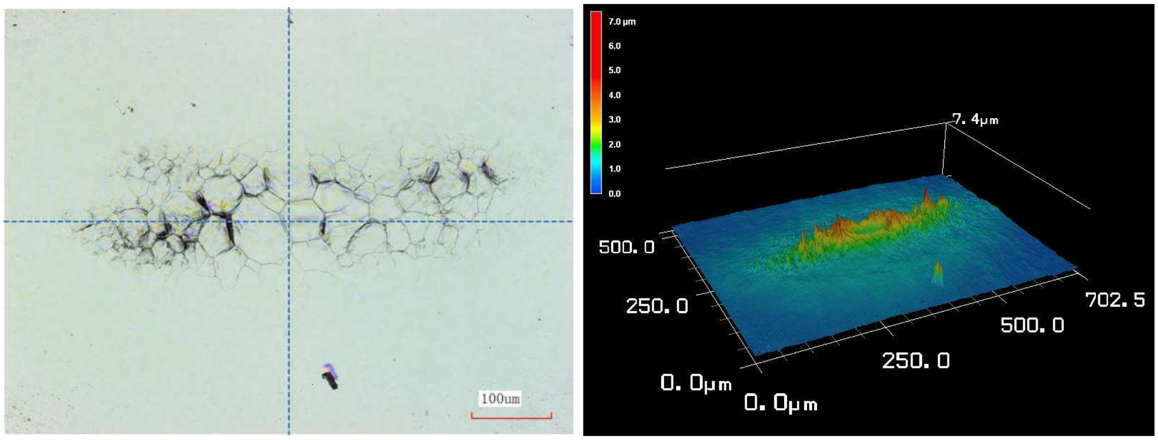

Figure 4.4: LSM and out-of-plane deformation images of the sample surface for a thermal shock load of 0.624 GW/m^2.

4.3 FEM simulation of thermal shock experiments at Siemens Healthcare

4.3.1 Geometry and FE mesh

In the single thermal shock experiments, the cooling and holding devices below the sample do not play a critical role for the material behavior near the sample's top surface, as the temperature at the bottom of the sample is not influenced significantly by the single thermal shock. Therefore, in the simulation, the cooling and holding devices below the sample are not modeled. For simplicity, a circular loading area was considered instead of the rectangular focal spot. The sample was assumed to be a disk with a thickness of 3 mm, and the loading was assumed in the central part of the top surface. The radius of the circular loading area was 324 µm to match the rectangular focal spot of the electron beam. The radius of the disk was set large enough (8 mm) so that the electron beam loading can be treated as a localized loading. The simplifications allow for a two-dimensional axisymmetric model. Compared to the three-dimensional model, the two-dimensional model saves a lot of computational effort and avoids convergence difficulties. For validation, a three-dimensional FEM simulation with a rectangular loading area was performed. The discrepancy between the maximum temperatures predicted by the three-dimensional and the two-dimensional simulations is less than 2%.

The simulations were performed with the commercial FEM tool ABAQUS [11]. A four-node axisymmetric quadrilateral element was used for the thermal and mechanical simulations. In total, there were 11598 elements. In order to obtain accurate results in the domain under the thermal shock loads, a finer finite element (FE) mesh with an element edge size of 4 µm was used in this area, see figure 4.5. The material parameters applied in this chapter is the same as in the previous chapter.

4.3.2 Loads and boundary conditions

In the simulations, the electron beam was modeled as a surface heat flux load. The energy of the electron beam, E_{B}, was Gaussian distributed at the sample surface, as described by

$$E_{\mathrm{B}} = 2.2061 F e^{-\frac{2r^2}{R^2}}, \tag{4.1}$$

where F is the averaged power density in the loading area, r is the distance from the center of the loading area and R is the radius of the loading area, see figure 4.5. The small amount of energy distributed outside the loading area is neglected in the simulations. The coefficient 2.2061 used here is based on the energy distribution measured in the loading area of the sample surface at Siemens Healthcare.

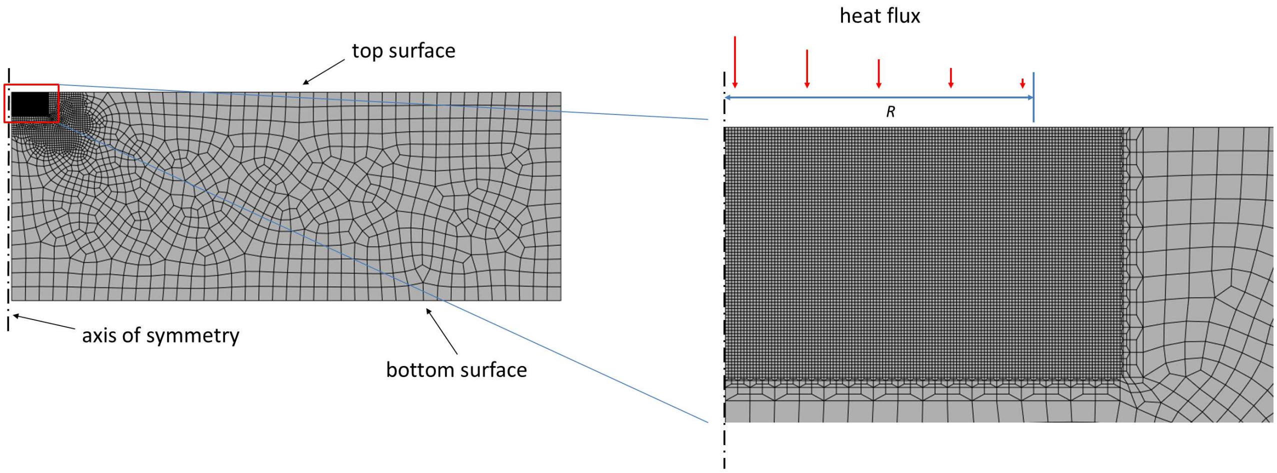

Figure 4.5: FE mesh of the two-dimensional axisymmetric model and finer mesh in the domain beneath the thermal shock loads. The axisymmetric boundary condition is applied on the left edge. R is the radius of the loading area.

The averaged power density in the loading area ranged from 0.374 GW/m^2 to 0.624 GW/m^2. The loading duration was 0.5 s and the base temperature is 20 °C. As cooling devices do not have much impact on the temperature near the top surface of the tungsten sample, a convective boundary condition was assumed at the bottom surface for the sake of simplicity.

4.3.3 Thermal simulation

For the numerical study in this chapter, the heat transfer problem was solved first. After that, its solution was read into the corresponding mechanical simulation as a predefined temperature field.

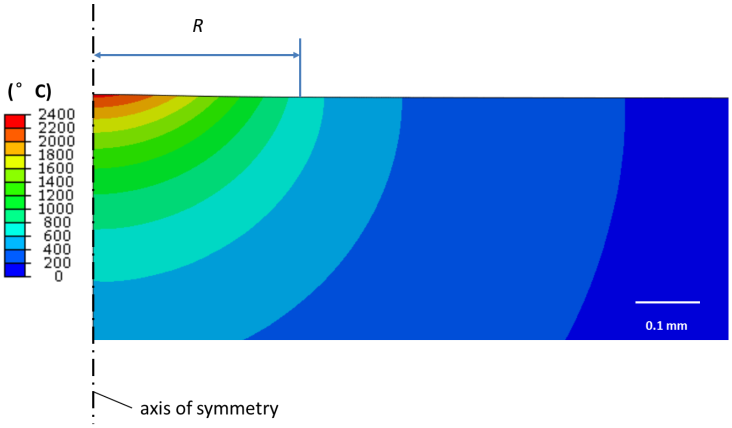

Figure 4.6: Temperature distribution at the end of heating for a thermal shock load of 0.624 GW/m^2.

The temperature distribution at the end of heating is shown in figure 4.6 for a thermal shock load of 0.624 GW/m^2. High temperature only occurs in the loading area. At a position of approximately 1 mm away from the loading center, the temperature is below 200 °C at the end of heating. The temperatures at the surface and along the axis of symmetry are shown in figures 4.7 and 4.8 for thermal shock loads of different power densities. Temperature increases as the power density increases. The temperature decreases as the distance from the center of the loading area increases. For all three power densities, the temperature during heating is above DBTT in most parts of the loading area. Figure 4.9 shows the temperature at the surface as a function of time for a thermal shock load of 0.624 GW/m^2. The temperature in the center of the loading area increases from room temperature to 2170 °C within 0.01 s. During the remaining heating time (0.49 s), it increases further by less than 100 °C, indicating that a quasi-steady-state is reached after the first few milliseconds. After heating, the temperature gradient in the loading area is drastically reduced within 0.002 s, as shown in figure 4.9. The numerical findings are in accordance with the analytical solutions reported in [58] for the one-dimensional heat conduction problem encountered when cooling down a sample of which its infinite surface is heated by a heat source of finite size prior to cooling.

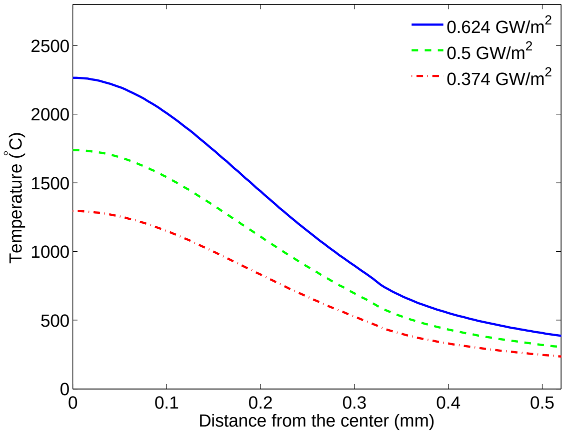

Figure 4.7: Temperature at the surface at the end of heating for thermal loads of different power densities.

4.3.4 Mechanical simulation

When the material is subjected to high temperatures and temperature gradients, plastic deformation cannot be avoided. Figure 4.10 gives an overview of the plastic strain distributions for a thermal shock load of 0.624 GW/m^2. During heating, the thermal expansion is largely constrained by the cold bulk material outside the loading area. As a result, plastic strain in radial direction is generated by compressive stress during the loading time. In the cooling phase, plastic strain in radial direction is generated by tensile stress due to the shrinking of the materials. However, the plastic strain in radial direction generated during cooling cannot counterbalance the plastic strain in radial direction

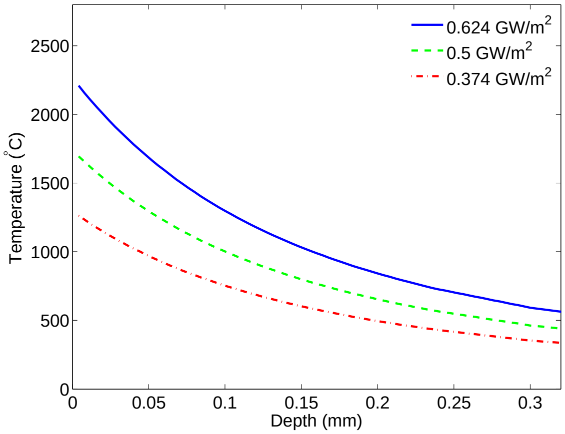

Figure 4.8: Temperature along the axis of symmetry at the end of heating for the thermal loads of different power densities.

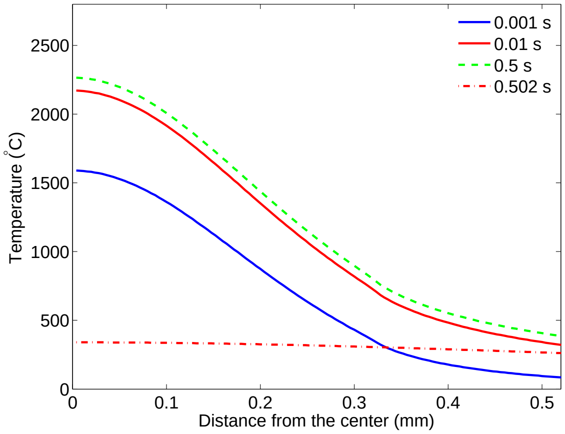

Figure 4.9: Temperatures at the surface at various times for a thermal shock load of 0.624 GW/m^2. The loading duration is 0.5 s.

generated during heating. The remaining plastic strain in radial direction leads to a residual stress distribution at the end of cooling. The plastic strains in the hoop and the radial directions are very similar. In axial direction, the plastic strain can be estimated under the assumption that the plastic flow usually takes place without change in volume, corresponding to a Poisson's ratio of 1/2. As a result, there is two times as much plastic strain in axial direction as there is in radial direction, see figure 4.11.

Figure 4.12 shows the surface plastic strain in radial direction after 0.5, 0.502 and 16 s for a thermal shock load of 0.624 GW/m^2. Plastic strain in radial direction is negative at the end of heating due to the constraint of the cold bulk material surrounding the loading area. After heating stops, a large reduction of the magnitude of the surface plastic strain in radial direction takes place within 0.002 s, which indicates that the material in the loading area is in a tensile state. The magnitude of the plastic

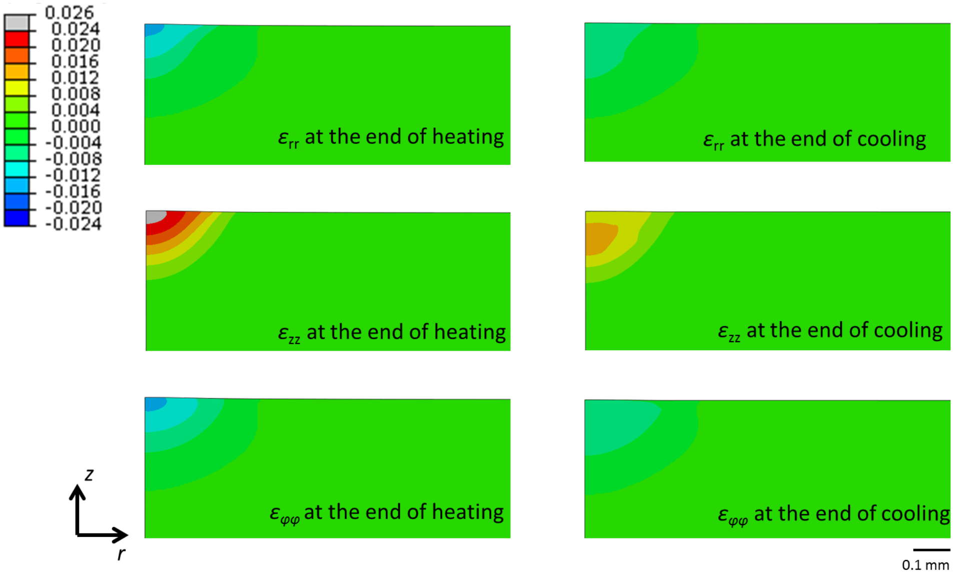

Figure 4.10: Plastic strain distributions for a thermal shock load of 0.624 GW/m^2. ε_{rr}, ε_{zz} and $\varepsilon_{\varphi\varphi}$ are the plastic strains in radial, axial and hoop directions.

strain in radial direction in the center of the loading area is significantly more reduced than at other locations. Within 0.002 s after heating stops, almost no further plastic strain in radial direction is generated, as the plastic strains are almost identical for 0.502 s and 16 s. In figure 4.13, plastic strain in radial direction at different depths is shown at the end of cooling for a thermal shock load of 0.624 GW/m^2. In the center of the loading area, the magnitude of plastic strain in radial direction at the surface is smaller than at a depth of 0.032 mm, while it is larger at the surface at the end of heating, see figure 4.10. This indicates that less plastic strain in radial direction is generated during cooling at a depth of 0.032 mm than there is at the surface.

The influence of power density at the surface plastic strain in radial direction is shown in figure 4.14. The size of the surface plastic zone increases, as the power density increases. Although a larger power density leads to a larger magnitude of plastic strain in radial direction in the center of the loading area during heating, the plastic strain in radial direction generated during cooling is larger during cooling as well. As a result, surface plastic strains in radial direction in the center of the loading area are almost identical at the end of cooling for thermal loads of 0.624 GW/m^2 and 0.5 GW/m^2. However, at a depth of 0.08 mm, the plastic strains in radial direction are different, see figure 4.15. The magnitude of plastic strain is larger for a larger power density.

Figure 4.16shows an overview of stress distributions. During heating compressive stresses are generated, and stresses are limited by the low yield stress of tungsten at high temperatures. After the sample is cooled down, residual tensile stress is generated due to the plastic strain distribution. There are two critical locations at which a concentration of residual stress in radial direction can be observed: firstly, the region right below the loading center; secondly, the region close to the edge of

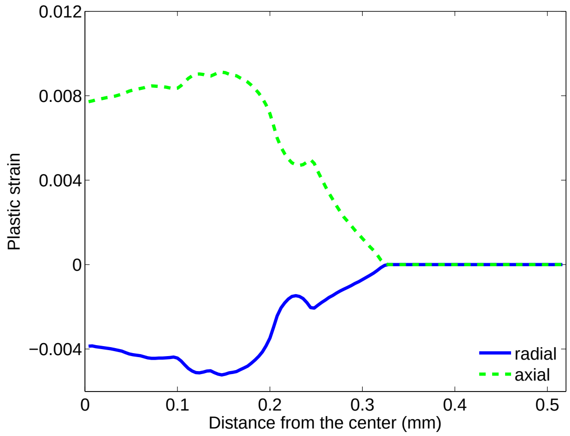

Figure 4.11: Surface plastic strain in radial and axial directions at the end of cooling for a thermal shock load of 0.624 GW/m^2

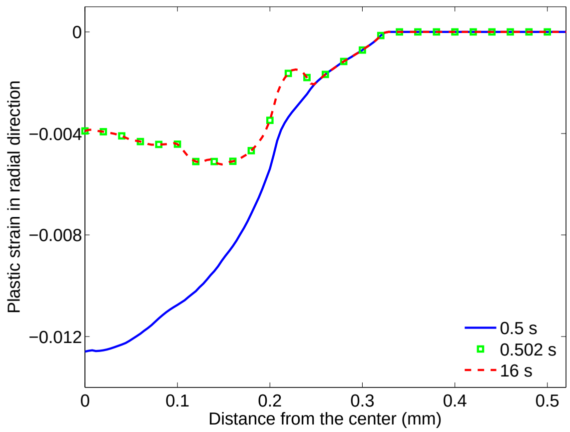

Figure 4.12: Surface plastic strain in radial direction at various times for a thermal shock load of 0.624 GW/m^2.

the loading area at the surface, see the distribution of stress in radial direction at the end of cooling in figure 4.16. The stress in hoop direction behaves similarly to the stress in radial direction except that there is no stress concentration near the edge of the loading area at the surface. Stress in axial direction is negligible compared to the radial or hoop stresses.

In figure 4.17 the evolution of surface stress in radial direction is shown for a thermal shock load of 0.624 GW/m^2. The surface stress in radial direction is compressive during heating and tensile during cooling. At the end of cooling, the stress in radial direction changes from tensile to compressive, as depth increases (see figure 4.18). This is due to the bending effect caused by the stress profile in depth direction.

The influence of power density on the stress in radial direction is shown in figure 4.19. The maximum surface stress in radial direction and the distance between the center of the loading area and the

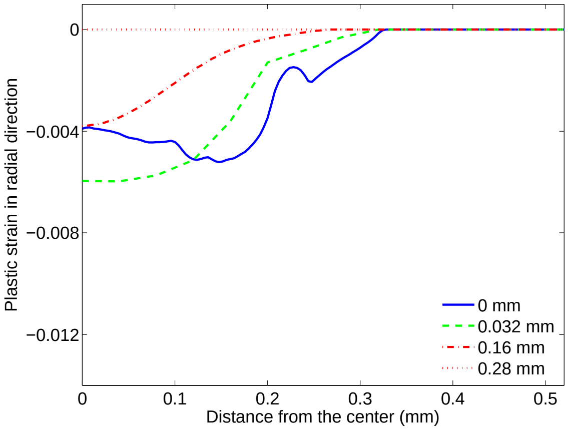

Figure 4.13: Plastic strain in radial direction at different depths at the end of cooling for a thermal shock load of 0.624 GW/m^2.

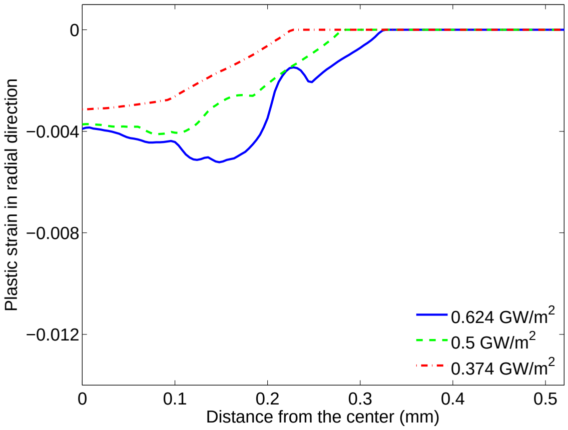

Figure 4.14: Surface plastic strain in radial direction at the end of cooling for thermal loads of different power densities.

position where the maximum surface stress in radial direction occurs both increase as the power density increases. In the center of the loading area, however, an increase in power density leads to smaller stress in radial direction. At a depth of 0.08 mm, the influence of power density on stress is more significant, see figure 4.19. Stress is larger for a larger power density.

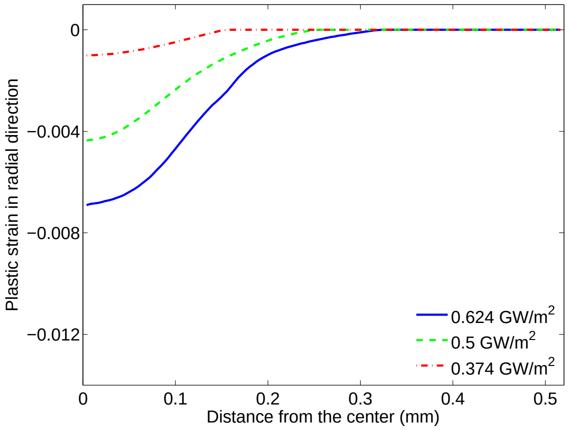

Figure 4.15: Plastic strain in radial direction at a depth of 0.08 mm at the end of cooling for thermal shock loads of different power densities.

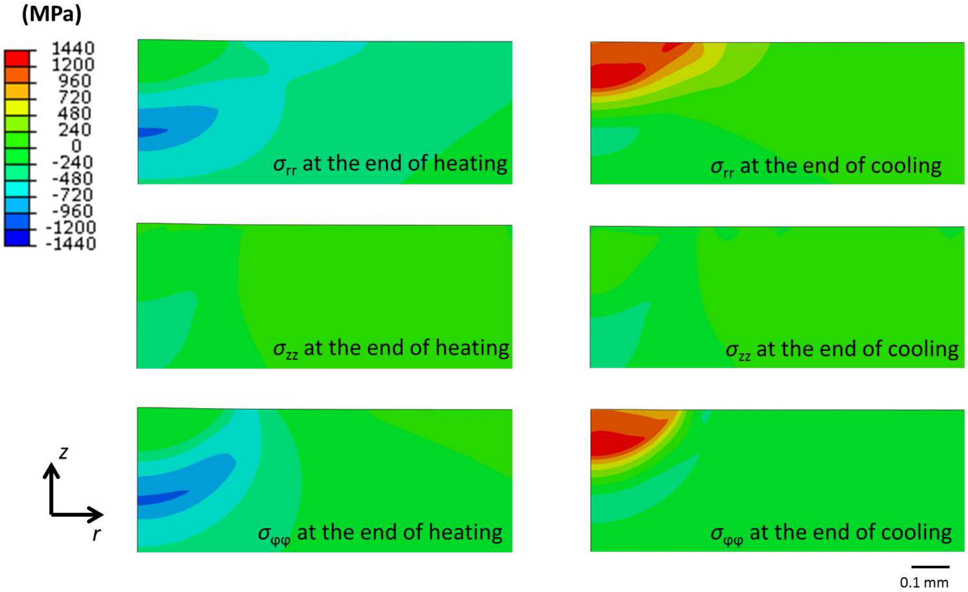

Figure 4.16: Distribution of stress in radial direction for a thermal shock load of 0.624 GW/m^2 (tension positive, compression negative). σ_{rr}, σ_{zz} and $\sigma_{\varphi\varphi}$ are the stresses in radial, axial and hoop directions, respectively.

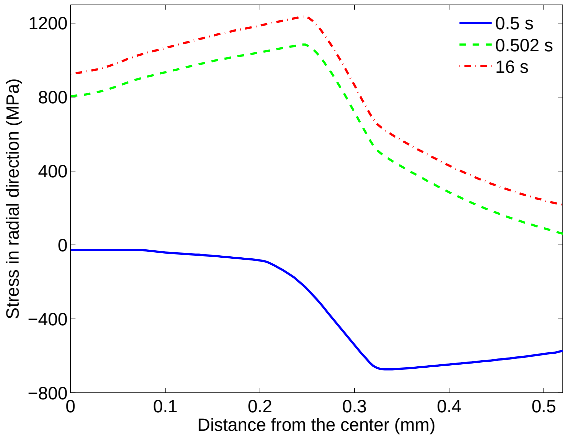

Figure 4.17: Surface stress in radial direction at various times for a thermal shock load of 0.624 GW/m^2.

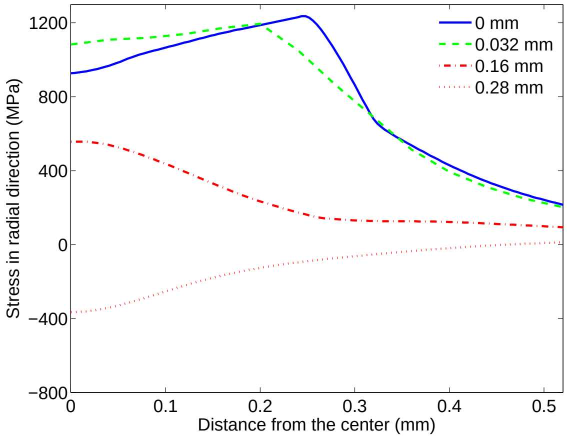

Figure 4.18: Stress in radial direction at different depths at the end of cooling for a thermal shock load of 0.624 GW/m^2.

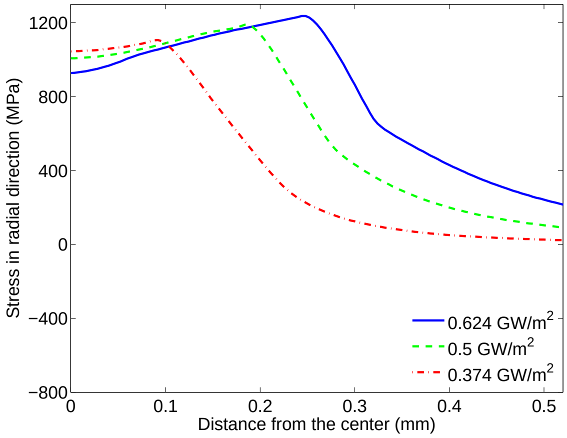

Figure 4.19: Surface stress in radial direction at the end of cooling for thermal loads of different power densities.

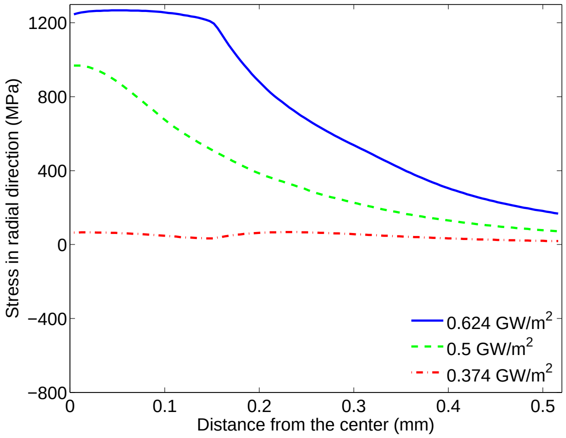

Figure 4.20: Stress in radial direction at a depth of 0.08 mm at the end of cooling for thermal shock loads of different power densities.

4.4 Fracture simulation of thermal shock experiments at Siemens Healthcare

Cracks at the surface of the tungsten armors can rapidly propagate into the tungsten component and lead to a loss of functionality, which shortens the life time of the component significantly. In this part, both XFEM and the FEM-based VCE method are used to conduct a fracture analysis. With XFEM, one is able to predict crack initiation and propagation, while the FEM-based VCE method can be used to calculate fracture mechanical parameters.

4.4.1 XFEM simulation

The XFEM predictions are collected in figures 4.21, 4.22 and 4.23. For a thermal shock load of 0.374 GW/m^2, initiation of a single crack that requires additional energy to be opened is predicted, which indicates that this loading is not critical for cracking, see figure 4.21. For a thermal shock load of 0.5 GW/m^2, several cracks are initiated (figure 4.22), but they need additional energy to be opened. The multiple crack initiations, which are close to each other, result in a degradation of the cohesive stiffness in the corresponding area. However, the densely distributed cracks will rarely occur in reality, since intergranular cracking is more likely to occur due to the weaknesses of the grain boundaries. For intergranular cracking the distance between two cracks is at least the size of a grain. When the distance between the cracks is larger, the energy dissipation associated with crack extension will be also larger, which indicates that opened cracks may occur for the loading of 0.5 GW/m^2. In figure 4.23, opened cracks are found for a thermal shock load of 0.624 GW/m^2. Compared to the tensile stress at the surface, the tensile stress below the surface is larger (as shown in figure 4.16). As a result, cracks are initiated below the surface. This effect leads to impurities below the surface, possibly as a result of the fabrication process, critical for cracking.

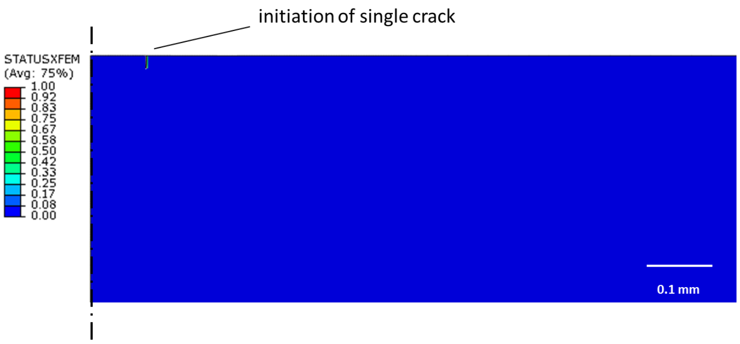

Figure 4.21: Crack predicted by XFEM simulation for a thermal shock load of 0.374 GW/m^2.

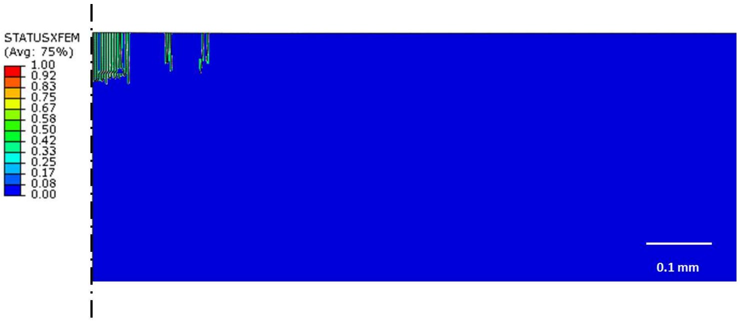

Figure 4.22: Cracks predicted by XFEM simulation for a thermal shock load of 0.5 GW/m^2.

Figure 4.23: Cracks predicted by XFEM simulation for a thermal shock load of 0.624 GW/m^2.

4.4.2 J-integral calculation

In the XFEM calculations, only cracks perpendicular to the top surface are found. Therefore, in this part, only J-integrals for precracks perpendicular to the top surface are computed at the end of cooling. The direction of the virtual crack tip extension is defined pointing into the sample. Length and location of precracks (see figure 4.24) are the variables of a parametric study. To avoid influence from other cracks, only one precrack is allowed in each simulation, where growth of the precrack is not possible.

Figure 4.25 shows the calculated J-integrals as a function of crack length and location for different thermal shock loads. In general, the J-integrals first increase as the distance from the center or the crack length increase. Then, after reaching a maximum, they decrease again. For a thermal shock load of 0.374 GW/m^2, J-integrals are much smaller than J_c, and no crack growth will occur. For a thermal shock load of 0.5 GW/m^2, in the central part of the loading area (r = 0.041, 0.162 mm) the J-integral for a precrack which is shorter than 8 μm, is smaller than J_c, while it is larger than J_c for a precrack longer than 16 μm. Since the grain boundaries are more vulnerable than the grain interior, and hence assuming that the initial defect can grow more easily along the interface between two grains into a crack of 16 μm perpendicular to the surface, further crack growth can occur according to the J-integral calculation. For a thermal shock load of 0.624 GW/m^2, nearly all J-integrals are larger than J_c in the central part of the loading area. Crack propagation is very likely to occur. However, the J-integral is smaller than J_c, as the crack length is larger than 0.15 mm, which indicates that this crack cannot become longer than 0.15 mm. The crack occurrence obtained from the J-integral calculations generally coincides with XFEM predictions.

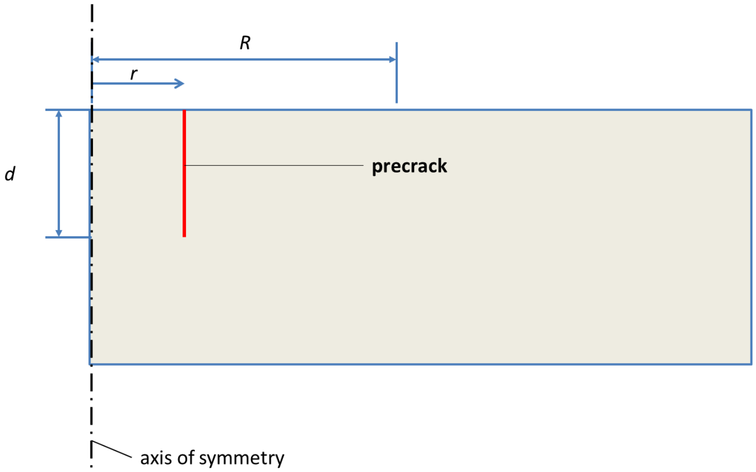

Figure 4.24: Precrack for calculation of J-integral, r is the distance from the axis of symmetry, d is the crack length of the precrack, and R is the radius of the loading area.

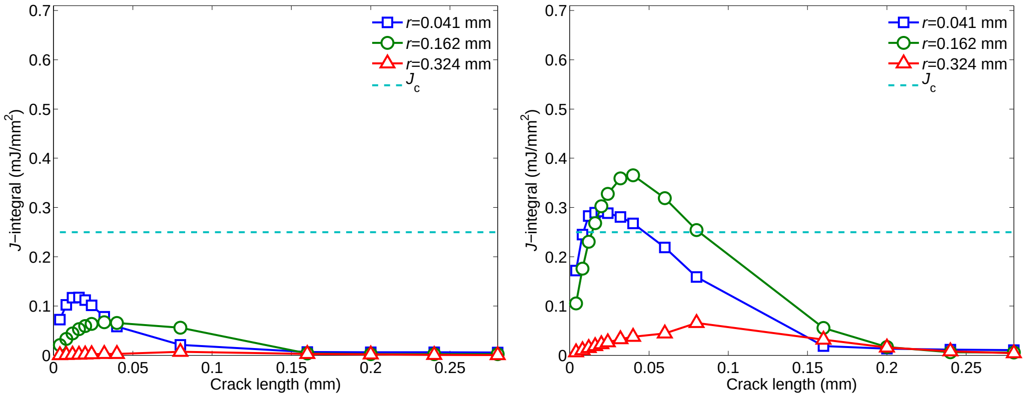

(a) 0.374 GW/m^2 (b) 0.5 GW/m^2

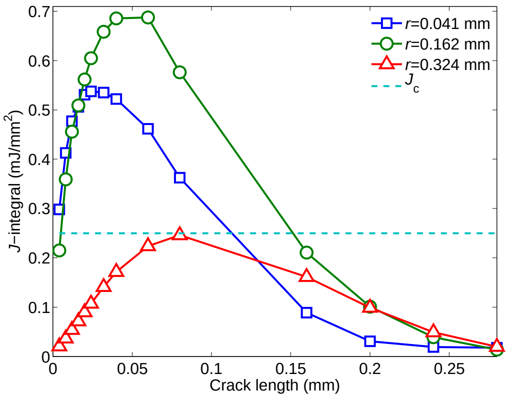

(c) 0.624 GW/m^2

Figure 4.25: J-integral for precracks at different locations as a function of the precrack length for thermal loads of 0.374 GW/m^2, 0.5 GW/m^2 and 0.624 GW/m^2.

4.5 Comparison of experimental and numerical results

4.5.1 Maximum temperature and cracking occurrence

Figure 4.26 shows a comparison of the maximum temperatures measured in the experiments and calculated in the corresponding simulations. The maximum temperature is linearly dependent on the power density. For a thermal shock load of 0.374 GW/m^2, the simulation result coincides with the measured value quite well. However, the deviation between the simulation results and the measured values is obvious for a thermal shock load of 0.624 GW/m^2. The reason may lie in the fact that the surface roughening caused by a thermal shock load of 0.624 GW/m^2 may result in a reduction of reflected electrons. Furthermore, the power density of thermal loads applied in chapter does not include the contribution of the secondary electron emission, which can result in an underestimation of the actual power density [48].

The cracking occurrence found in the experiments generally coincides with both the XFEM and the J-integral predictions. No cracking occurrence is found for a thermal shock load of 0.374 GW/m^2, while for a thermal shock load 0.624 GW/m^2 cracks are both predicted numerically and detected in the experiments. For a thermal shock load of 0.5 GW/m^2, the experiments show an occurrence of tiny cracks. XFEM simulation predicts the initiation of multiple cracks, but these cracks are not completely opened. The J-integral for the precrack, which is situated in the central part of the loading area and which is longer than 16 µm, is larger than J_c for a thermal shock load of 0.5 GW/m^2. The numerical results for a thermal shock load of 0.5 GW/m^2 indicate that cracks may occur, however, they do not grow as readily as for a thermal shock load 0.624 GW/m^2.

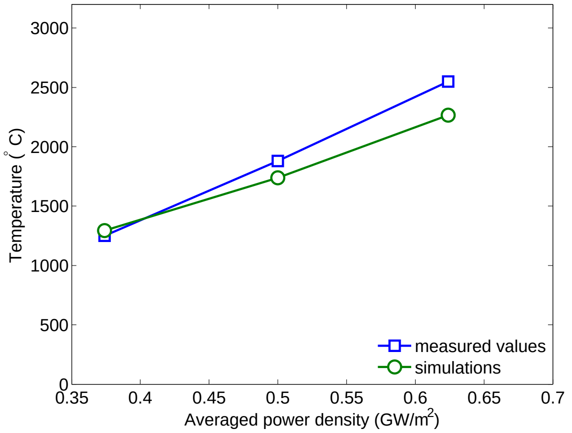

Figure 4.26: Comparison of maximum temperatures measured in the experiments and calculated in the corresponding simulation for thermal shock loads of different power densities.

4.5.2 Surface roughness

Line surface roughness results were extracted from figures 4.2, 4.3 and 4.4. Their results are shown in figure 4.27. Two lines (see the dashed lines in figures 4.2, 4.3 and 4.4), which pass through the center of the loading area and are parallel to either the horizontal (width) or the vertical (height) edges of the LSM images, are chosen for the line surface roughness measurements. The roughness far away from the loading area is assumed as zero. For thermal shock loads of 0.374 GW/m^2 and 0.5 GW/m^2, the roughness along the two lines does not exhibit dramatic local fluctuations, and surface roughening is induced by plastic deformation. For a thermal shock load of 0.624 GW/m^2, the zig-zag profile of roughness suggests that cracks are opened.

The roughness predicted by the thermo-mechanical simulations is plotted as well. The roughness in the simulation refers to the vertical displacement at the top surface. In these simulations, no cracks are considered. The findings of the experiments and the simulation results coincide with each other for thermal loads under which surface roughening is mainly induced by plastic deformation, and the minor error between the experimental and simulation results might result from the error in the thermal calculation and from errors due to the simplification of the model (e.g. circular

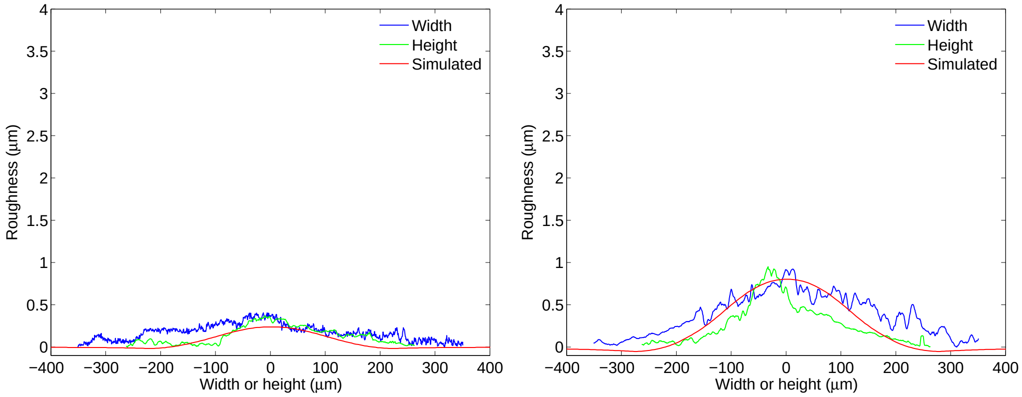

(a) 0.374 GW/m^2 (b) 0.5 GW/m^2

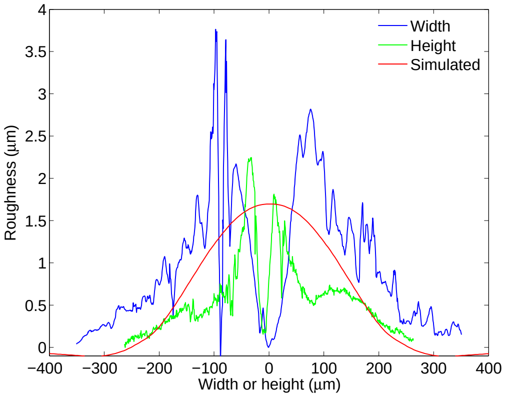

(c) 0.624 GW/m^2

Figure 4.27: Roughness for thermal shock loads of 0.374 GW/m^2, 0.5 GW/m^2 and 0.624 GW/m^2. Width: measured roughness along the horizontal dashed lines in figures 4.2, 4.3 and 4.4, Height: measured roughness along the vertical dashed lines in the same figures, Simulated: surface vertical displacement in the simulations.

instead of rectangular loading area). If cracks are opened, there are obvious differences between the experimental and the simulation results, see figure 4.27 c.

4.6 Summary

In this chapter, fracture behavior of tungsten under single thermal shock of a loading duration of 0.5 s was studied. Experimental and numerical studies were performed and compared. The primary conclusions can be summarized as follows:

1. Finite element simulations revealed that the thermal steady state was reached within several milliseconds after the onset of a heat flux pulse. Experimental observation showed that thermal shock loads could cause considerable grain growth, although the pulse duration was relatively short (0.5 s).
2. Finite element simulations confirmed that the surface cracking of tungsten was caused by tensile residual stress produced during cooling stage as a consequence of compressive plastic yield of the surface layer under heating.
3. At thermal shock loads below 0.5 GW/m^2 the loading area at the surface exhibited plastic roughening without occurrence of cracks. The plastic deformation of the surface layer was measured using the laser scanning microscope and compared with the predicted profile of the finite element simulations achieving good agreement.
4. According to the thermal shock tests open cracks began to form on the surface when the applied heat flux load was higher than 0.5 GW/m^2. This threshold value of power density for cracking was predicted by the computational fracture simulation as well. Both XFEM technique and VCE method yielded consistent predictions on the cracking behavior.

Chapter 5

Fracture mechanics analysis of a tungsten divertor under stationary thermal loads

5.1 Stationary thermal loads on the divertor

In addition to transient events, such as ELM and VDE, the divertor has to withstand stationary heat flux loads. The stationary heat flux loads can reach up to 10 MW/m^2 for the ITER divertor target [73]. In the case of the DEMO divertor, the range of possible heat flux load may be even larger. Although the stationary heat flux load is not as intensive as transient events, when the divertor target component (a bi-material joint structure) is loaded under such high heat flux loads continuously, it is subjected to high thermal stresses not only at the surface but also inside the divertor. Thus, the high heat flux loads impose a strong constraint on the structure-mechanical performance of the divertor, in particular if tungsten is considered as a structural material of a pressurized component [74]. The brittleness of tungsten should be a critical issue even for the functional application as armor, if the operation temperature is below the DBTT of tungsten. This is the case in a water-cooled tungsten mono-block divertor. The DBTT of a commercial tungsten material ranges between 400 °C - 700 °C depending on the loading modes [19]. This means that most of the tungsten armor in the water-cooled mono-block target will remain below the DBTT during typical high heat flux loadings. Furthermore, one has to consider the irradiation embrittlement effect in addition. Thus, the combination of brittleness and the thermally induced stress fields due to the high heat flux loads raises a serious reliability issue concerning the structural integrity of tungsten armor.

The literature only offers few previous works dealing with this issue. One relevant paper is the finite element method (FEM)-based probabilistic failure risk analysis of tungsten armor in a water-cooled divertor target published by You and Komarova [75]. They used the weakest-link failure theory expressed by the Weibull statistics and calculated the impact of embrittlement on the failure risk probability of tungsten armor considering four different cracking criteria based on linear elastic fracture mechanics. Another related work [76] is the crack loading analysis of the bond interface between a tungsten flat tile and a copper heat sink in a water-cooled target model. Furthermore, Blanchard and Martin studied the fracture and creep behavior of an all-tungsten divertor for ARIES [77]. However, there are no previous reports to be found in the literature that are dedicated to a thorough fracture analysis of tungsten armor apart from these.

The aim of this chapter is to deliver quantitative estimates of the vulnerability of a tungsten monoblock armor to cracking under stationary high heat flux loads. To this end, a comparative fracture mechanical investigation was carried out by means of two different types of computational approaches - namely, XFEM and the FEM-based VCE method. For the VCE method, the crack tip loading is described in terms of the stress intensity factor (SIF) or the J-integral. The results of a comprehensive parametric study obtained from both simulation methods are presented. In total, nine different load cases are considered as a combination of three different heat flux loads and three different coolant temperatures - and the impact of the temperature level and the temperature gradient resulting from the different loading cases on crack initiation is discussed.

5.2 FEM simulation of the water-cooled divertor under stationary thermal loads

5.2.1 Geometry, FE mesh and materials

The monoblock type divertor target model has already been applied to the water-cooled divertor target of ITER. Furthermore, it was also considered for the water-cooled divertor target of a fusion power plant in the framework of the Power Plant Conceptual Study (model A: WCLL) [78]. The monoblock target consists of a number of small rectangular tungsten blocks which are connected by a long cooling tube made of a high thermal conductivity metal (e.g. copper alloy) running through the central region of each block, see figure 5.1. Two neighboring blocks are separated by a thin gap (∼0.3 mm). The deposited heat is transported from the surface to the cooling tube through the tungsten block. The block functions as sacrificing armor whereas the tube acts as a heat sink. The typical dimensions of a block are roughly 20 × 20 × 3-5 mm, and the tube has an inner diameter of 10 mm (1 mm wall thickness). The distance from the loading surface to the tube is determined by the predicted erosion rate and the envisaged erosion lifetime. At the brazed bond interface between the tungsten block and the copper alloy tube, a thin (∼0.5 mm) interlayer of soft copper is placed in order to reduce the residual or thermal stress.

The model PFC considered for the FEM study is a water-cooled tungsten mono-block duplex structure consisting of a tungsten armor block and a CuCrZr alloy coolant tube (heat sink). The geometry, the finite element (FE) mesh and the constituent materials of the considered model PFC are shown in figure 5.2. The tungsten armor block has dimensions of 23 × 22 × 4 mm. The heat sink tube has a wall thickness of 1.0 mm and an inner diameter of 12 mm. The thickness of the copper interlayer is 0.5 mm. The geometry used here is based on the optimization of the geometry of the ITER tung-

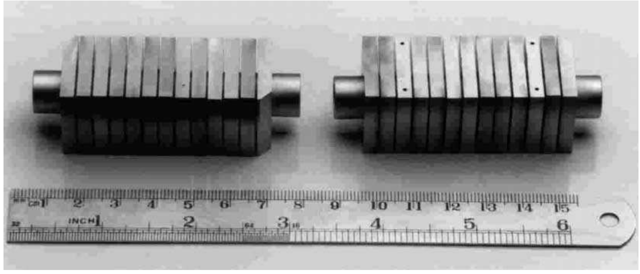

Figure 5.1: Picture of representative mock-ups with 13 tungsten blocks [6].

sten divertor [79]. The commercial FEM code ABAQUS was employed for the numerical studies employing quadratic brick elements of 20 nodes each. In total, there were 8496 finite elements. The mesh in the critical region of the component was refined.

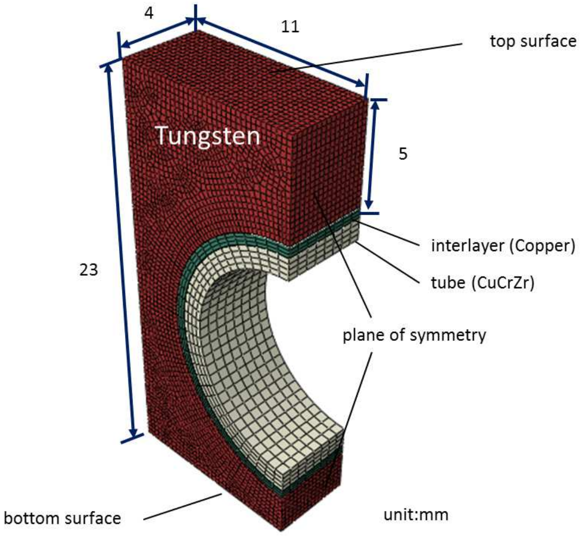

Figure 5.2: The FE mesh of the mono-block divertor model. Due to symmetry only one half of the structure was considered.

The thermo-mechanical elasto-plastic simulations are based on data of several materials in the PFC model. Cross-rolled and stress-relieved tungsten was applied for the tungsten armor block. Tungsten was assumed to behave elasto-ideally plastic. A precipitation-hardened CuCrZr alloy was considered for the heat sink tube and soft-annealed copper constituted the interlayer. The Frederick-Armstrong constitute model applied for copper and the CuCrZr alloy is based on the combination of non-linear isotropic and kinematic hardening laws [80–82] (for details, see appendix A). Temperature-dependent material properties are listed in table 5.1 for selected temperatures, corresponding to the operation temperatures of the considered materials. It should be noted that the material is assumed to be unirradiated due to lack of data of irradiated materials.

Table 5.1: Properties of the considered materials at selected temperatures [9, 10].

	Tungsten[1]			CuCrZr[2]		Copper[3]	
	20 °C	400 °C	1200 °C	20 °C	400 °C	20 °C	400 °C
Young's modulus (GPa)	398	393	356	115	106	115	95
Yield stress (MPa)	1385	1100	346	273	238	3	3
Q^* (MPa)				-43	-68	76	36
b^*				6	10	8	25
C^* (MPa)				148575	117500	64257	31461
γ^*				930	1023	888	952
Heat conductivity (W/mK)	175	140	105	318	347	379	352
Coefficient of thermal expansion (10^{-6}/K)	4.5	4.6	5.3	16.7	17.8	17.8	18.1

[1] Rolled and stress-relieved state.
[2] Precipitation-hardened state, the reference alloy: Elmedur-X (code: CuCr1Zr, Cr: 0.8%, Zr: 0.08%).
[3] Softened by annealing at 700 °C for 1 h.
[*] Material parameters entering the Frederick-Armstrong constitutive model (see Appendix A).

5.2.2 Loads and boundary conditions

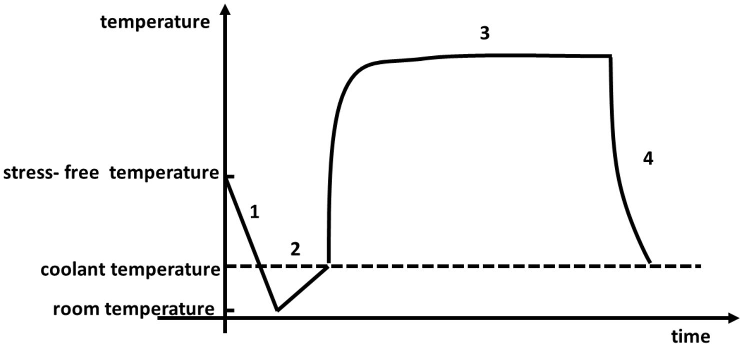

Figure 5.3: Schematic drawing of the thermal excursion of the PFC. 1: cooling from the stress-free temperature to room temperature, 2: preheating to the coolant temperature, 3: high heat flux loading, 4: cooling to the coolant temperature.

The thermal excursion (as shown in figure 5.3) of the PFC consists of 4 steps. The first step is cooling the PFC from the stress-free temperature[1] to room temperature. Subsequently, a pre-heating of the PFC to the coolant temperature is applied. Then, the HHF load is applied on the top surface of the PFC for 30 s. After HHF loading, the PFC is cooled to the coolant temperature within 10 s.

The heat transfer coefficient between the inner wall of the heat sink tube and the coolant water is plotted in figure 5.4. The pressure of the coolant water is 5 MPa. The displacement of the end cross-sections of the tube is fully fixed in the tube axis direction, as the tube is assumed to have infinite length. The bottom surface of the PFC is fixed in vertical direction. This full constraint boundary

---

[1] The stress-free temperature is assumed to be 450 °C, at which it is assumed that there is zero stress in the PFC.

condition is taken as an extreme case to gain a conservative prediction (i.e. higher stress in the tungsten block due to this constraint).

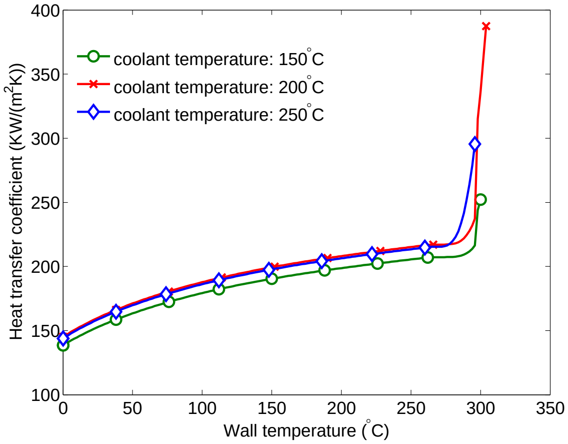

Figure 5.4: Heat transfer coefficient between the inner wall of the heat sink tube and the coolant water.

5.2.3 Thermal simulation

In this part, the heat transfer problem was solved first. Then its solution was read into the corresponding mechanical simulation as a predefined temperature field. In order to cover the loading conditions in DEMO and ITER, thermal simulations were performed for nine loading combinations of HHF loads of 10 MW/m^2, 15 MW/m^2, 18 MW/m^2 and coolant temperatures of 150 °C, 200 °C, 250 °C.

The temperature distribution of the tungsten armor block is shown for an HHF load of 15 MW/m^2 and a coolant temperature of 200 °C at the end of HHF loading in figure 5.5. Two positions in the tungsten armor block are selected to represent temperatures due to variations of HHF loads and coolant temperatures. The peak temperature in the tungsten armor block occurs at position 1. The temperature at position 2 is interesting, since this region is considered to be vulnerable, as shown by the following mechanical simulation.

Table 5.2 lists the peak temperatures at two positions for different HHF loads and coolant temperatures. The peak temperature in the tungsten armor block ranges from 820 °C to 1562 °C, while the peak temperature at position 2 lies between 294 °C to 447 °C, indicating that most of this region of the PFC is below the DBTT during the HHF loading. When a higher HHF load is applied, the peak temperature as well as the temperature difference between the peak temperature and the coolant temperature increases, while a higher coolant temperature only enlarges the peak temperature. The difference between the peak temperature and the coolant temperature remains almost the same, irrespective of the coolant temperature.

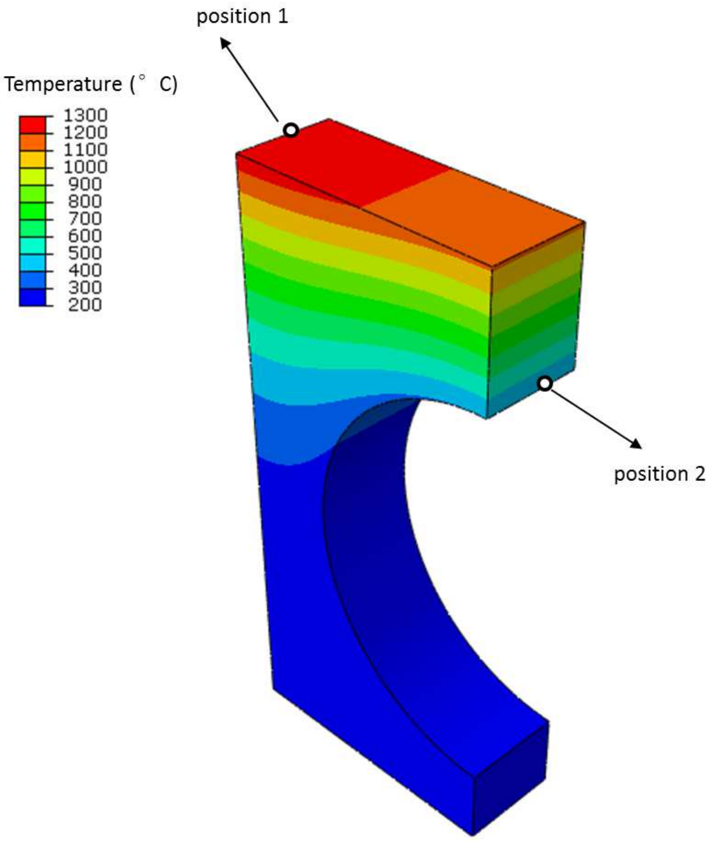

Figure 5.5: Temperature distribution of the tungsten armor block for an HHF load of 15 MW/m^2 and a coolant temperature of 200 °C at the end of HHF loading. Two positions are defined to represent temperatures due to variations of HHF loads and coolant temperatures. The heat sink tube and the interlayer are not shown.

5.2.4 Mechanical simulation

To illustrate the stress distribution, figure 5.6 shows the stress distribution plotted for an HHF load of 15 MW/m^2 and a coolant temperature of 200 °C. The stress distribution in the tungsten armor block results from the temperature distribution in the tungsten armor block as well as from the thermal mismatch between the tungsten armor block and the interlayer. Therefore, stresses are to be seen as most critical at the highest values of temperature and temperature gradient - namely at the end of the HHF loading. At the end of the HHF loading, compressive hoop stresses concentrate at the top surface close to the plane of symmetry and the back surface in the narrow strip-shaped domains of the tungsten armor block. Tensile hoop stresses are concentrated in the region close to the interlayer in the upper part of the tungsten armor block. Radial and axial stresses are negligible compared to the hoop stress. At the end of cooling, the hoop stress is significantly smaller than it is at the end of the HHF loading. Radial and axial stresses are similar to those at the end of HHF loading.

Table 5.2: Peak temperatures (°C) for different HHF loads and coolant temperatures at the two positions, as shown in figure 5.5.

coolant temperature	150 °C	200 °C	250 °C
position 1			
10 MW/m^2	820	879	924
15 MW/m^2	1221	1279	1315
18 MW/m^2	1478	1531	1562
position 2			
10 MW/m^2	294	339	368
15 MW/m^2	362	398	415
18 MW/m^2	404	434	447

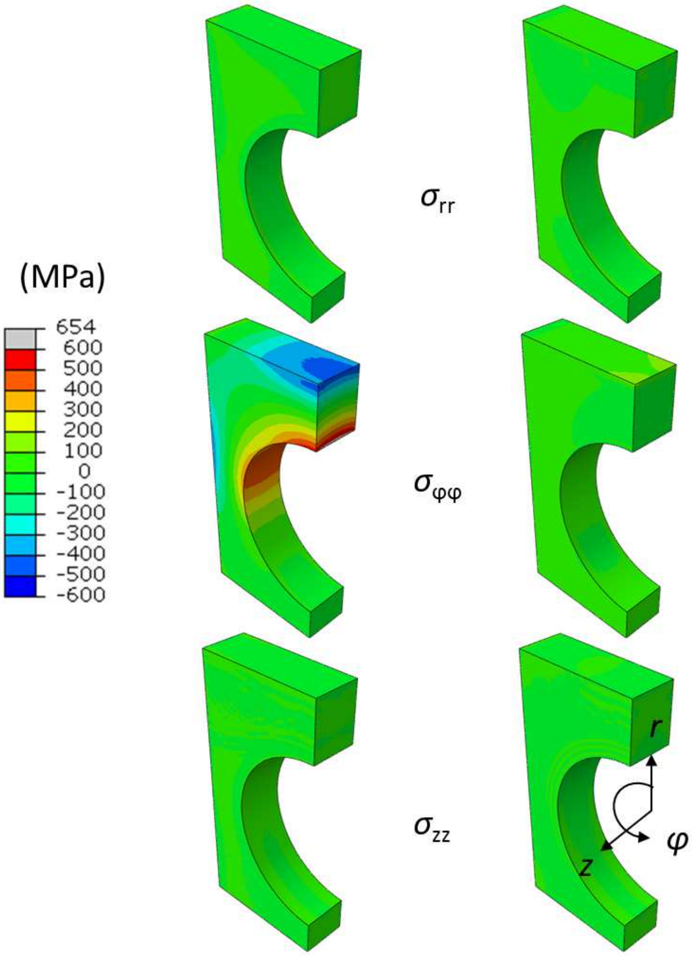

Figure 5.6: Stresses of the tungsten armor block for an HHF load of 15 MW/m^2 and a coolant temperature of 200 °C at the end of HHF loading (left column) and after final cooling (right column). The heat sink tube and the interlayer are not shown. Cylindrical coordinates with their origin at the center of the tube on the plane of the right end cross-section of the tube are applied for the plots.

5.3 Fracture simulation of the water-cooled divertor under stationary thermal loads

5.3.1 XFEM simulation

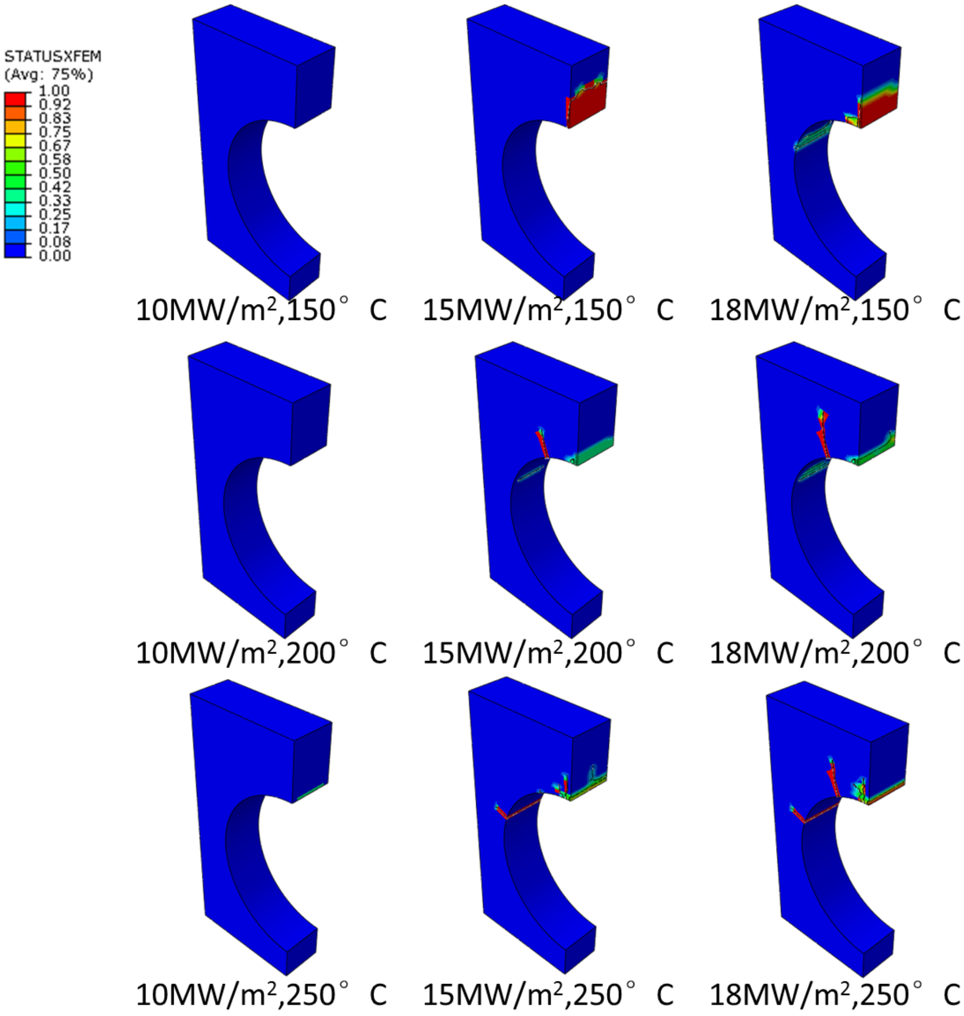

Figure 5.7: XFEM simulations for different HHF loads and coolant temperatures with an MPS of 400 MPa.

In this part, XFEM [1] is applied to predict the most probable location of crack initiation and the preferred orientation of initial crack growth. Basically, the value of the ultimate tensile strength could be used for the MPS. Table 5.2 shows the peak temperature in the region in which the hoop stress is concentrated is about 400 °C, while the ultimate tensile strength of tungsten at 400 °C is about 950 MPa [8]. Strictly speaking, the ultimate tensile strength cannot be reached in the simulation.

---

[1] In this part, linear brick elements were used for the XFEM simulations, as quadratic brick elements are not supported in the ABAQUS XFEM code.

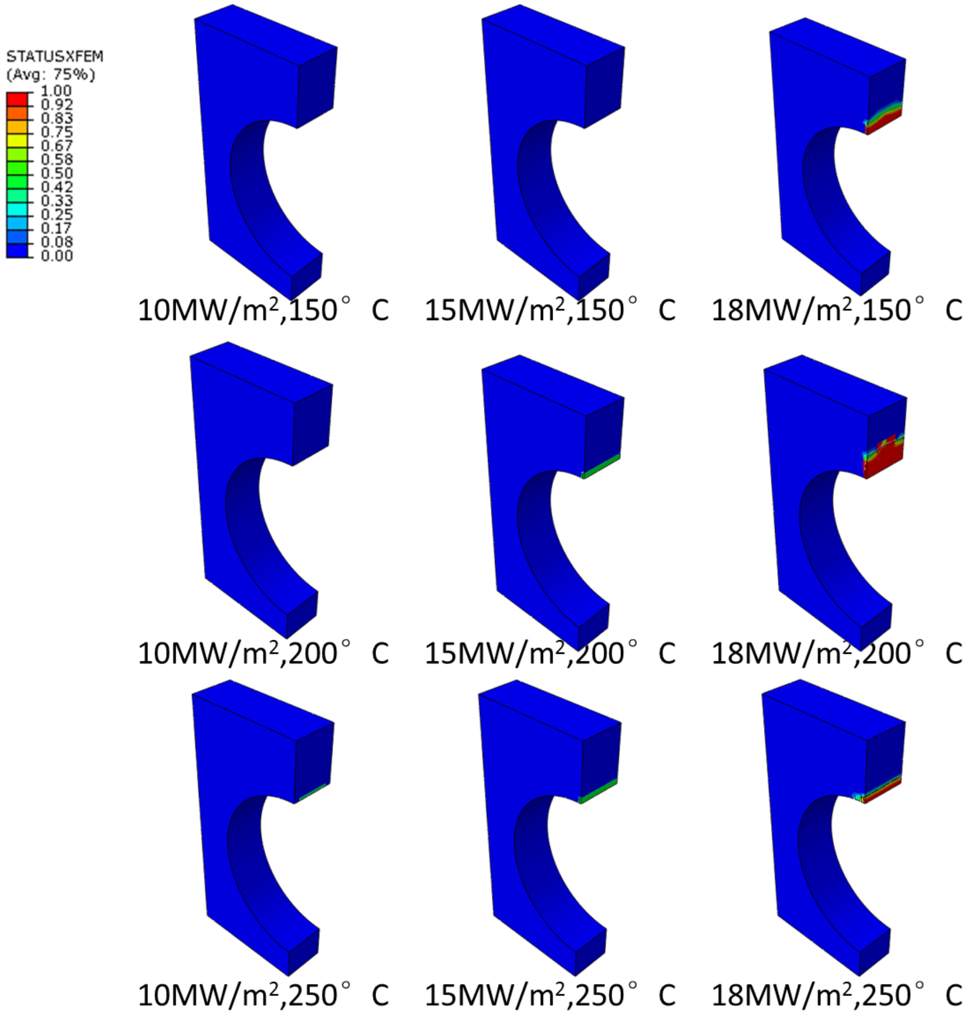

10MW/m^2,150° C 15MW/m^2,150° C 18MW/m^2,150° C

10MW/m^2,200° C 15MW/m^2,200° C 18MW/m^2,200° C

10MW/m^2,250° C 15MW/m^2,250° C 18MW/m^2,250° C

Figure 5.8: XFEM simulations for different HHF loads and coolant temperatures with an MPS of 600 MPa. The heat sink tube and the interlayer are not shown in the plots.

However, a parametric study of the MPS serves to study a possible crack propagation pattern and to consider a possible reduction of the strength of tungsten during the long term operation. Thus, values of 400 MPa, 600 MPa and 800 MPa are assumed and the fracture energy is set to be 0.25 mJ/mm^2, a value obtained from fracture toughness tests for tungsten at 400 °C [61]. In this dissertation, it is focused on the fracture behavior of tungsten, and thus cracking is only allowed in the tungsten armor block in the XFEM simulations.

Figure 5.7 shows the results of XFEM simulations with an MPS of 400 MPa for different HHF loads and coolant temperatures. Under the HHF load of 10 MW/m^2, no crack appears. When the HHF load is above 15 MW/m^2, radial cracks occur in the critical region as predicted by the stress analysis: Cracks are initiated near the interlayer in the upper part of the tungsten armor block and propagate along radial direction. The influence of multiple cracks is obvious in the simulations. The most critical region for cracking, as predicted by mechanical simulations, lies in the region near the interlayer and the plane of symmetry in the upper part of the tungsten armor block. However, if multiple cracks occur simultaneously in this region, the stress concentration is largely relaxed and cracks cannot grow significantly. At the same time, the radial crack at a larger angle has the possibility to be initiated and propagate, as shown in the HHF loading cases of 15 MW/m^2 and 18 MW/m^2 in figure 5.7. If the MPS is set to be 600 MPa, as shown in figure 5.8, no opened crack appears for the HHF loads of 10 MW/m^2 and 15 MW/m^2. When the MPS is set to 800 MPa, no opened crack is predicted for any HHF load studied in chapter.

5.3.2 Stress intensity factor calculation

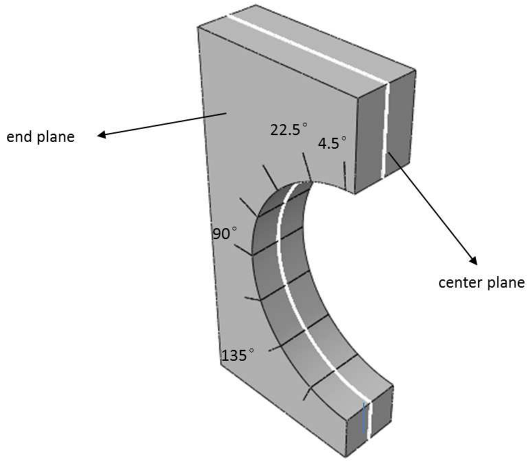

Figure 5.9: Precracks in radial direction through the tungsten armor block. The heat sink tube and the interlayer are not shown.

To capture the crack features in a quantitative way, SIFs and J-integrals for precracks are calculated by the FEM-based VCE method. As shown in figure 5.6, the tensile hoop stress is concentrated in the upper part of the tungsten armor block at the end of the HHF loading, while the stresses in other directions are negligible during the whole thermal excursion. Based on this result as well as XFEM simulation results, radial precracks for computing SIFs and J-integrals are inserted in the tungsten armor block, as shown in figure 5.9. The direction of the virtual crack tip extension follows the positive radial direction. All precracks are through-thickness cracks along the z-axis. For the purpose of a parametric study, the length of precracks in radial direction varies from 0.5 mm to 1.5 mm. The length of the precrack is fixed for each simulation - and only one precrack is set up at a time, in order to avoid interaction with other precracks.

Cracking is governed by the stresses in the vicinity of the crack tip and the SIF is the magnitude of the stress singularity at the tip of a mathematically sharp crack in a linear elastic material. The elasto-plastic simulations show that no plastic yielding occurred in the domain of the PFC where precracks

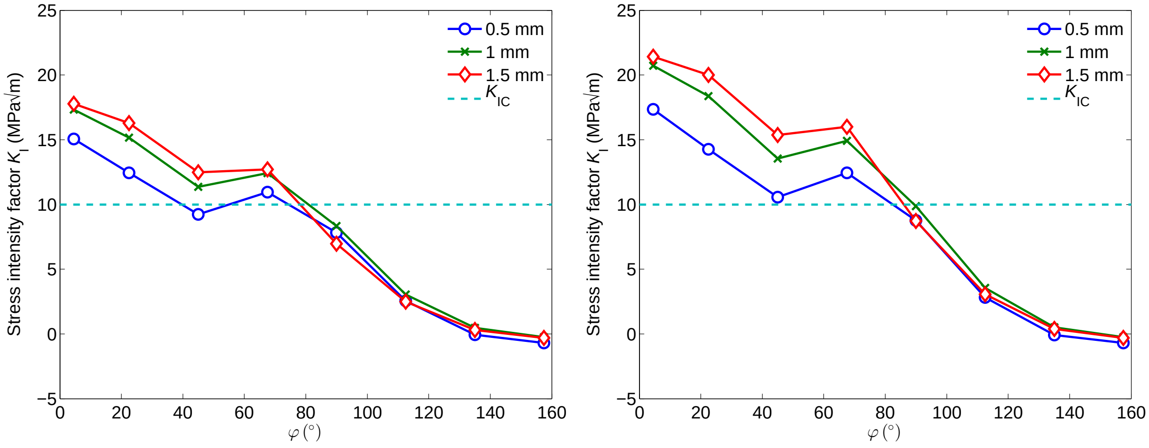

(a) End plane (b) Center plane

Figure 5.10: Stress intensity factor K_I for precracks of different angles and lengths at the end of the HHF loading for the HHF load of 15 MW/m^2 and the coolant temperature of 200 °C, see Figure 5.9.

were inserted in the tungsten armor block. This result ensures the prerequisites for applying a failure analysis based on linear elastic fracture mechanics concerning precracks in the tungsten armor block. Modes I, II and III of the SIFs are used to describe the cracking modes of normal opening, inplane shear and out-of-plane shear, respectively. Based on the stress analysis, mode I is considered to be the critical crack mode in chapter. A fracture criterion for crack propagation is defined as follows: As the stress intensity factor of mode I reaches the critical value, unstable fracture will occur and cracks can propagate. The critical value of K_I (K_IC: 10 MPa$\sqrt{\mathrm{m}}$) refers to the data gained from fracture toughness tests at 400 °C [61]. As stresses are not constant along the z-axis, K_I is calculated at each plane perpendicular to the z-axis in the tungsten armor block.

Figures 5.10 and 5.11 depict K_I at the end of HHF loading and cooling. K_I calculated for the end plane is slightly smaller than the one calculated for the center plane, as the free surface is subjected to lower stresses, see figure 5.6. However, the tungsten armor block is more vulnerable at the free surface due to the possible defects during fabrication, which means that a crack is more likely to be initiated at the free surface. In the following work, K_I is therefore evaluated at the free surface (end plane) unless mentioned otherwise.

In figure 5.10, K_I decreases as the angle of the precrack increases. While K_I for the precrack in the upper part ($\varphi \leq 90°$) of the tungsten armor block is larger than the critical value, K_I for the precrack in the lower part ($\varphi > 90°$) is much smaller, because here the temperature is not markedly influenced by the HHF loads. When the angle is 157 °, K_I even attains a small negative value, which indicates that the precrack tends to close. For precracks with small angles in the upper part K_I increases if the precrack length is increased from 0.5 mm to 1.0 mm. The difference of K_I for precracks of 1 mm and 1.5 mm is not significant.

At the end of cooling, K_I of all precracks are far smaller than the critical value (see figure 5.11),

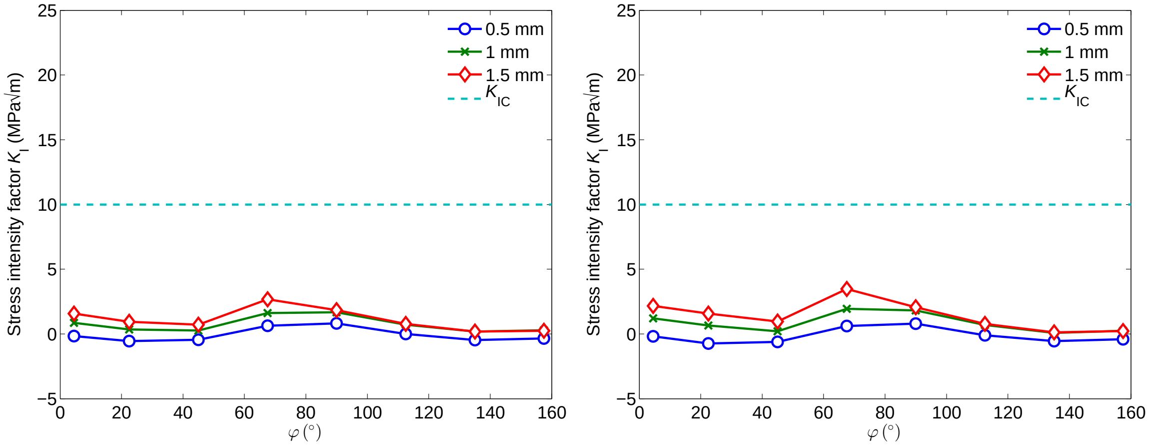

(a) End plane (b) Center plane

Figure 5.11: Stress intensity factor K_I for precracks of different angles and lengths at the end of cooling for an HHF load of 15 MW/m^2 and a coolant temperature of 200 °C, see Figure 5.9.

which suggests that radial cracks of mode I will not propagate in the tungsten armor block at the end of cooling. This result is in line with the outcome of the stress analysis.

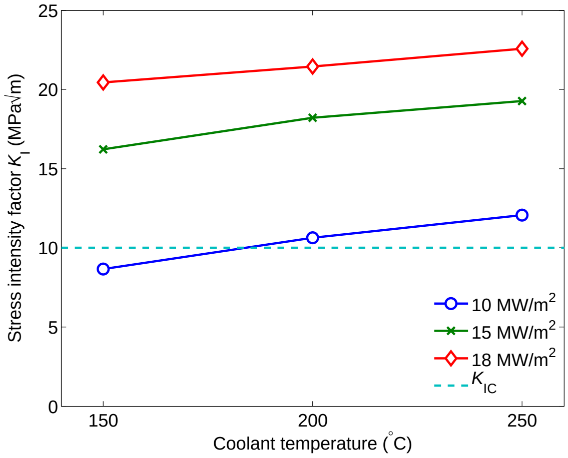

Figure 5.12: K_I for the precrack at the end of HHF loading for different HHF loads and coolant temperatures. The angle of the precrack is 4.5 °, and the length of the precrack is 1 mm.

Figure 5.12 shows K_I for the precrack at the end of the HHF loading for different HHF loads and coolant temperatures. K_I increases as the HHF loads and coolant temperatures increase. The increase of K_I is more significant as the HHF load changes from 10 MW/m^2 to 18 MW/m^2 than when the coolant temperature changes from 150 °C to 250 °C. K_I for an HHF load of 10 MW/m^2 corresponds to the critical value, while K_I for HHF loads of 15 MW/m^2 and 18 MW/m^2 exceeds the critical value by far.

Effect of stress-free temperature

In the thermal calculation, the stress-free temperature is set equal to the heat treatment (annealing) temperature of the joined mock-up that is assumed for prime hardening of the CuCrZr alloy (i.e. for precipitation hardening of the tube). This annealing is supposed to take place after joining at higher temperature and the subsequent cooling to room temperature. It is assumed that the previous residual stress will disappear during annealing, and the final residual stress is solely determined by the thermal expansion mismatch stress due to cooling from the annealing temperature (450 °C) to room temperature.

To study the effect of the annealing temperature on the behavior of tungsten, simulations with different stress-free temperatures (20 °C, 450 °C and 900 °C) were conducted. Figure 5.13 represents values of K_I for precracks subjected to different stress-free temperatures. K_I is much larger for a stress-free temperature of 20 °C than for the other two. If the PFC is cooled down from the stress-free temperature to room temperature, the tungsten block will show elastic deformation, which could be used to counteract the deformation resulting from preheating and HHF loading. Therefore, if there is no such elastic deformation in the tungsten armor block (e.g. with a stress-free temperature of 20 °C), the deformation resulting from the preheating and HHF loading will be larger. Accordingly, K_I will be larger, too. However, the stored elastic deformation is limited by the onset of the plastic deformation in the interlayer. When the interlayer behavior is dominated by plasticity, the increase of stored elastic deformation in the tungsten armor block due to an increase of the stress-free temperature is limited. This is the reason why the decrease of K_I resulting from the stress-free temperature change from 450 °C to 900 °C is not significant, compared to the decrease of K_I resulting from the stress-free temperature change from 20 °C to 450 °C.

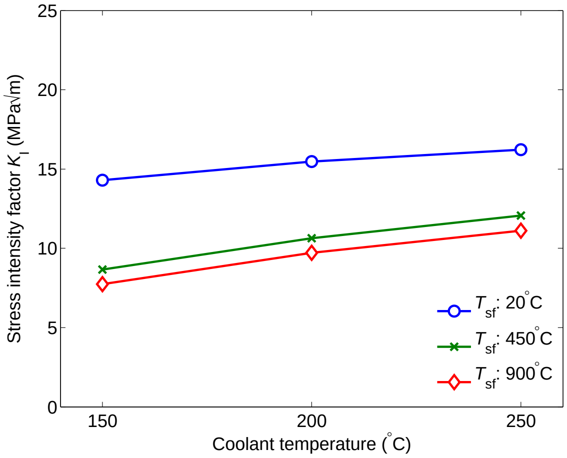

Figure 5.13: K_I for a precrack subjected to different stress-free temperatures for an HHF load of 10 MW/m^2 and different coolant temperatures. The angle of the precrack is 4.5 °, and the length of the precrack is 1 mm.

5.3.3 J-integral calculation

In the framework of elasticity, SIFs can be converted to J-integrals. Figure 5.14 shows J-integrals for the specified precrack at the end of the HHF loading for an HHF load of 15 MW/m^2 and different coolant temperatures. J-integrals show the same tendency as K_I: the J-integral increases as the coolant temperature increases. Generally, the J-integral results calculated from the SIFs and directly with ABAQUS tend to coincide with each other. The minor differences between J-integrals calculated from SIFs and directly with ABAQUS are to be expected as well, since the method of calculating J-integrals from the SIF is more sensitive to numerical precision than calculating J-integrals in ABAQUS [11]. Moreover, the J-integral could be used as an elasto-plastic fracture mechanics parameter, with which it is convenient to study the fracture behavior of tungsten, when plasticity occurs due to softening of the material by recrystallization or by long term cyclic loading.

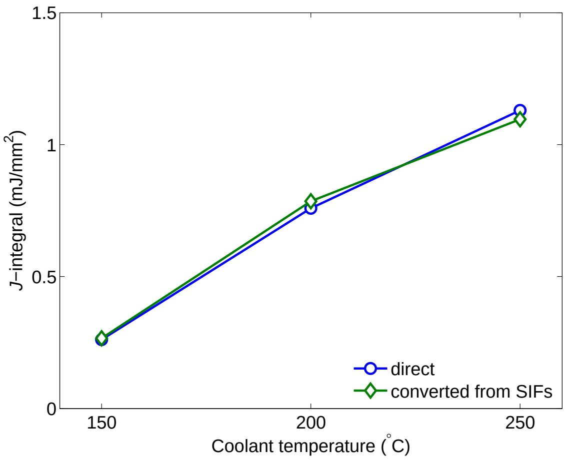

Figure 5.14: J-integrals for a precrack for an HHF load of 15 MW/m^2 and different coolant temperatures. The angle of the precrack is 4.5 °, and the length of the precrack is 1 mm.

5.4 Summary

In this chapter, an extensive finite element analysis of the fracture mechanical behavior of a tungsten mono-block divertor target was carried out considering ITER- and DEMO-relevant heat flux loading conditions. Two different computational approaches were employed for the fracture simulation, namely, the FEM-based VCE method for computing K_I (or J-integrals) and XFEM for predicting progressive cracking. A comparative parametric investigation was conducted for three different heat flux loads and three different coolant temperatures (nine load case combinations in total). The tungsten armor block showed several unique fracture mechanical features allowing to draw the following conclusions:

1. The most probable pattern of crack formation is radial cracking in the tungsten armor block starting from the interface with the copper interlayer.
2. The most probable area of cracking is the upper interfacial region of the tungsten armor block adjacent to the top position of the copper interlayer.
3. The driving force of cracking turns out to be heavily dependent on the thermal boundary condition. The driving force increases as either the heat flux load or the coolant temperature increase.
4. The initiation of a major crack only becomes likely if the strength of the tungsten armor block is significantly reduced compared to its original strength (e.g. due to embrittlement by neutron irradiation or recrystallization).
5. The threshold strength for cracking depends on the specific load case. For heat flux loads below 10 MW/m^2, the threshold value of the failure stress is about 400 MPa. Under heat flux loads of 15 MW/m^2 and 18 MW/m^2, the threshold values of the failure stress are about 600 MPa and 800 MPa, respectively.
6. A lower stress-free temperature increases the risk of radial crack growth.
7. Both simulation approaches yield qualitatively identical predictions. The methodology of the study in this chapter could be applied to design-by-analysis of a divertor target on the basis of the ITER Structural Design Criteria, even though the tungsten mono-block armor itself does not belong to the structural component.

Chapter 6

General conclusions and outlook

6.1 General conclusions

Nearly all plasma-facing surfaces in the International Thermonuclear Experimental Reactor (ITER) are/will be armored with tungsten. Also, tungsten is the most promising armor material for the plasma-facing components of the DEMOnstration power plant (DEMO). However, the inherent brittleness of tungsten at low temperature is a very critical issue to the reliability of the plasma-facing components. The aim of this dissertation is to understand and predict the brittle failure of tungsten under high heat flux loads using numerical approaches.

In this dissertation, three relevant high heat flux loads are considered: short transient thermal loads by edge localized mode (ELM), slow high-energy-deposition thermal loads (e.g. vertical displacement events (VDEs)) and stationary heat flux loads. Two-dimensional numerical simulations were performed for short transient thermal loads and slow high-energy-deposition thermal loads according to the corresponding electron beam irradiation tests. A three-dimensional finite element model was built to be able to study the failure behavior of the tungsten armored divertor under stationary heat flux loads.

The tungsten armor's thermal and mechanical responses to the three loading events were analyzed in detail. The maximum temperature under ELM-like transient thermal loads is in general below the melting point of tungsten for the power densities of 0.3-1.3 GW/m^2 at base temperatures of 20-800 °C. For slow high-energy-deposition thermal loads, the maximum temperature is usually above the melting point of tungsten due to its long loading pulse. However, if the loading is constrained to a small area, the temperature can be kept below the melting point of tungsten. The maximum temperatures in the armored tungsten divertor under ITER and DEMO relevant stationary heat flux (10-18 MW/m^2) with a coolant temperature up to 250°C are below 1600°C.

Plastic strains are generated at the surface of tungsten armors under ELM-like transient thermal loads and slow high-energy-deposition thermal loads, while there is almost no plastic strain in the tungsten armor block of the divertor under purely stationary loading. Tensile residual stress is generated during cooling for the ELM-like transient thermal loads and slow high-energy-deposition thermal loads. This residual stress turns out to be critical for cracking at the surface of the tungsten armor. For the stationary heat flux loads, the level of stress is much lower than that for transient thermal loads. In contrast to the transient thermal cases where the residual stress during cooling plays an important role, thermal stress during heating is the most critical stress for cracking in the tungsten block of the divertor under stationary heat flux loads. In the tungsten divertor, stress concentration occurs in the upper part of the tungsten block and close to the interlayer. The temperature in this area is below or close to the ductile-to-brittle transition temperature (DBTT) during the stationary heat flux loading, which increases the risk of a brittle failure of tungsten material. In general, cracking of tungsten is likely to occur during cooling for the transient thermal loads and during heating for the stationary heat flux loads.

Based on the different features of the three loading scenarios, fracture mechanical investigations were carried out with the help of the weight function method, the extended finite element method (XFEM) and the FEM-based virtual crack extension (VCE) method. Several conclusions are drawn from the fracture mechanics study for the three loading scenarios:

Short transient thermal loads

1. When the loading area is sufficiently large, the simplified analytical solution based on a semi-infinite space assumption can give good estimates of temperature, stress and strain in the central part of the loading area.

2. Cracking of tungsten under ELM-like transient thermal loads is due to the residual stress that is generated during cooling. Cracking occurs at the surface when the ductility of tungsten is significantly reduced as the temperature drops below DBTT.

3. The failure map, which is created by comparing the J-integrals for precracks with the critical energy release rate obtained from the fracture toughness tests, shows a reasonable agreement with the experimentally observed results. The crack formation is predicted for the power density of 0.6 GW/m^2 and above, and when the base temperature is higher than 600 °C, almost no cracks is predicted. An efficient way to prevent brittle cracking of tungsten is to operate the tungsten armor at the temperatures above the threshold temperature.

4. A ramp pulse with a longer duration leads to lower temperatures and stresses in comparison to a constant pulse with a shorter duration. Yet, the difference is moderate when both their maximum power density and total deposited energy are identical.

5. Compared to the triangular loading, cracks produced at the edge of the loading area under the uniform loading are more likely to grow further in parallel to the loading surface.

Slow high-energy-deposition thermal loads

1. When the loading area of the slow high-energy-deposition thermal loads is limited, the maximum temperature can be kept below the melting point of tungsten. A nearly steady-state of the temperature profile at the surface of tungsten can be reached after several milliseconds of the slow high-energy-deposition thermal loading.

2. In the experiments, recrystallization of tungsten could be observed after slow high-energy-deposition thermal loads in case the numerical prediction of the maximum temperature, which coincides with the temperature measurements, was above the recrystallization temperature of tungsten, even with a loading duration of only 0.5 s.

3. The good agreement between the experimental observations and the numerical predictions proves the validity of the computational approaches. The method used in this dissertation can therefore serve as an adequate basis for the design of divertors in fusion reactors.

Stationary heat flux loads

1. Stationary heat flux loads do not cause severe plastic deformation in the tungsten armor block of the divertor. The cracking due to stationary heat flux loads occurs most likely near the coolant pipe in the tungsten armor block due to the tensile thermal stress. The most probable pattern of crack formation is radial cracking in the tungsten armor block starting at the interface with the copper interlayer.

2. Under stationary heat flux loads, stress is not critical in the tungsten armor block as long as no severe material degradation occurs.

3. The joining technique of the divertor has significant impact on the stress distribution in the tungsten armor block (e.g. a lower stress-free temperature increases the risk of radial crack growth.).

6.2 Outlook

In this dissertation, the numerical predictions generally coincide with the experimental observations. However, there is still much space to improve the accuracy of the current numerical results. A promising approach would be to compile a more detailed material characterization, as follows:

(1) Thermal and mechanical properties of tungsten should be investigated under cyclic thermal loadings and in operationally relevant environments. The high fluxes of energetic neutrons, hydrogen and helium ions, as well as a bombardment by helium isotopes may degrade the thermal and mechanical properties of tungsten.

(2) As the plasma-facing components will be exposed to stationary heat flux for longer time periods while in operation, creep can occur due to the critical exposure time and exposure temperature. Considering the corresponding material parameter in the calculation may help to obtain more realistic results.

(3) Microstructure characterizations (e.g. grain size, material properties at grain boundaries, grain orientations and pore distributions) of tungsten or tungsten alloys should be determined in detail, as microstructure features have significant impact on the behavior of a material. Once a micromechanical finite element model is established, a multiscale model can serve to transfer the results obtained at the microscopic to the macroscopic scale.

From the result of this study, it becomes evident that cracking of tungsten is inevitable under some ITER relevant transient thermal loadings. Therefore, future work should address numerical investigations concerning the development of cracks based on a more detailed model (e.g. a microstructure model). Once the cracking patterns are understood and can be controlled, strategies can be developed to conquer the material weakness. One possibility is to use a tungsten composite instead of tungsten and tungsten alloys. The composite concept cannot only improve the material properties (e.g. the reinforcement with tungsten fibers, which is considered as a way to retain tungsten toughness even under conditions of embrittlement), but also help to control the cracking patterns. Furthermore, modelling of thermal fatigue of tungsten under ITER relevant thermal loadings will be of great interest to the component design in case that the proper material data can be obtained from the corresponding tests.

Appendix A

Frederick-Armstrong model

Considering asymmetric hardening, the von Mises yield criterion is given by

$$F_{\mathrm{potential}} = [\frac{3}{2}(\mathbf{S} - \boldsymbol{\alpha}') \colon (\mathbf{S} - \boldsymbol{\alpha}')]^{0.5} - \sigma_{\mathrm{e}}\varepsilon_{\mathrm{e}}^{\mathrm{p}} = 0, \tag{A.1}$$

where $F_{\mathrm{potential}}$ is the plastic potential in the sense of the associated flow rule, **S** the deviatoric stress tensor, $\boldsymbol{\alpha}'$ the deviatoric backstress tensor, σ_{e} the equivalent stress and $\varepsilon_{\mathrm{e}}^{\mathrm{p}}$ the equivalent plastic strain. The backstress tensor α stands for the yield surface displacement in a stress space, whereas σ_{e} indicates the size of the yield surface. The non-linear kinematic hardening law is expressed as [83]

$$\dot{\boldsymbol{\alpha}} = \frac{C}{\sigma_e}(\boldsymbol{\sigma} - \boldsymbol{\alpha})\dot{\varepsilon}_{\mathrm{e}}^{\mathrm{p}} - \gamma\boldsymbol{\alpha}\dot{\varepsilon}_{\mathrm{e}}^{\mathrm{p}}, \tag{A.2}$$

where $\dot{\boldsymbol{\alpha}}$ is the backstress rate tensor, C is the initial kinematic hardening modulus, $\boldsymbol{\sigma}$ is the stress tensor, $\varepsilon_{\mathrm{e}}^{\mathrm{p}}$ is the equivalent plastic strain rate and γ is a constant determining the rate at which the kinematic hardening modulus decreases with increasing plastic strain. C and γ are material parameters to be calibrated. The first term in A.2 is the contribution of Ziegler's linear kinematic hardening, and the second one is the non-linear relaxation term. The non-linear isotropic hardening law is expressed as

$$\sigma_e = \sigma_0 + Q[1 - \exp(-b\varepsilon_{\mathrm{e}}^{\mathrm{p}})], \tag{A.3}$$

where σ_0 is the initial size of the yield surface, Q the maximum change in the size of the yield surface and b defines the rate at which the size of the yield surface changes as plastic straining progresses. Q and b are material parameters to be calibrated. The five material parameters of the combined nonlinear hardening law are calibrated by fitting method using the stabilized loops of unidirectional strain controlled cyclic tension-compression tests [78].

Bibliography

[1] BP p.l.c, BP Energy Outlook 2030, London, United Kingdom, 2013.

[2] European Fusion Development Agreement, Tokamaks, 2014, `http://www.efda.org/fusion/fusion-machine/types-of-fusion-machines/tokamaks`.

[3] M. Merola, D. Loesser, A. Martin, P. Chappuis, R. Mitteaua, V. Komarova, R. Pitts, S. Gicquel, V. Barabash, L. Giancarli, J. Palmer, M. Nakahira, A. Loarte, D. Campbell, R. Eaton, A. Kukushkin, M. Sugihara, F. Zhang, C. Kim, R. Raffray, L. Ferrand, D. Yao, S. Sadakov, A. Furmanek, V. Rozov, T. Hirai, F. Escourbiac, T. Jokinen, B. Calcagno, S. Mori, ITER plasma-facing components, Fusion Engineering and Design 85 (2010) 2312–2322.

[4] T. Hirai, K. Ezato, P. Majerus, ITER relevant high heat flux testing on plasma facing surfaces, Materials Transactions, The Japan Institute of Metals 46 (2005) 412–424.

[5] M. Rödig, M. Akiba, P. Chappuis, R. Duwe, M. Febvre, A. Gervash, J. Linke, N. Litounovsky, S. Suzuki, B. Wiechers, D. Youchison, Comparison of electron beam test facilities for testing of high heat flux components, Fusion Engineering and Design 51-52 (2000) 715–722.

[6] E. Visca, B. Riccardi, A. Orsini, C. Testani, Manufacturing and testing of monoblock tungsten small-scale mock-ups, Fusion Engineering and Design 56-57 (2001) 343–347.

[7] Siemens AG, Internal report on physical parameters of tungsten, 1995.

[8] PLANSEE, Tungsten material properties and applications, 2014, `http://www.plansee.com/en/Materials-Tungsten-403.htm`.

[9] J.-H. You, M. Miskiewicz, Material parameters of copper and CuCrZr alloy for cyclic plasticity at elevated temperatures, Journal of Nuclear Materials 373 (2008) 269–274.

[10] ITER Structural Design Criteria for In-vessel Components (SDC-IC), ITER Document No. G 74 MA 8 01-05-28 W0.2, 2008.

[11] Abaqus analysis user’s manual 6.12., Dassault Systémes Simulia Corp., Providence, RI, USA, 2012.

[12] Wikipedia, Nuclear binding energy, 2014, `http://en.wikipedia.org/wiki/Nuclear_binding_energy`.

[13] S. Glasstone, R. H. Lovberg, Controlled thermonuclear reactions, 1960.

[14] C. M. Braams, P. E. Stott, Nuclear Fusion: Half a Century of Magnetic Confinement Fusion Research, Taylor & Francis, 2002.

[15] ITER, The ITER story, 2014, `http://www.iter.org/proj/iterhistory`.

[16] V. Barabash, M. Akiba, I. Mazul, M. Ulrickson, G. Vieider, Selection, development and characterisation of plasma facing materials for ITER, Journal of Nuclear Materials 233-237 (1996) 718–723.

[17] T. Hirai, H. Maier, M. Rubel, P. Mertens, R. Neu, E. Gauthier, J. Likonen, C. Lungu, G. Maddaluno, G. Matthews, R. Mitteau, O. Neubauer, G. Piazza, V.Philipps, B. Riccardi, C. Ruset, I. Uytdenhouwen, R& D on full tungsten divertor and beryllium wall for JET ITER-like wall project, Fusion Engineering and Design 82 (2007) 1839 – 1845.

[18] F. Elio, K. Ioki, P. Barabaschi, L. Bruno, A. Cardella, M. Hechler, T. Kodama, A. Lodato, D. Loesser, D. Lousteau, N. Miki, K. Mohri, R. Parker, R. Raffray, D. Williamson, M. Yamada, W. Daenner, R. Mattas, Y. Strebkov, H. Takatsu, Engineering design of the ITER blanket and relevant research and development results, Fusion Engineering and Design 46 (1999) 159–175.

[19] D. Rupp, S. M. Weygand, Loading rate dependence of the fracture toughness of polycrystalline tungsten, Journal of Nuclear Materials 417 (2011) 477–480.

[20] A. A. Griffith, The phenomena of rupture and flow in solids, Philosophical Transactions of the Royal Society of London 221 (1921) 163–198.

[21] G. Irwin, Analysis of stresses and strains near the end of a crack traversing a plate, Journal of Applied Mechanics 24 (1957) 361–364.

[22] H. Tada, P. C. Paris, G. R. Irwin, The Stress Analysis of Cracks Handbook, 3rd Edition, American Society of Mechanical Engineers Press, 2001.

[23] D. P. Rooke, D. J. Cartwright, Compendium of Stress Intensity Factors, Her Majesty's Stationery Office, 1976.

[24] J. R. Rice, A path independent integral and approximate analysis of strain concentration by notches and cracks, Journal of Applied Mechanics 35 (1968) 379–386.

[25] H. Bückner, A novel principle for the computation of stress intensity factors, Journal of Applied Mathematics and Mechanics 50 (1970) 529–546.

[26] T. Fett, D. Munz, Stress intensity factors and weight functions, Computational Mechanics Publications, Southampton, 1997.

[27] G. Glinka, G. Shen, Universal features of weight functions for cracks in mode I, Engineering Fracture Mechanics 40 (1991) 1135–1146.

[28] C. F. Shih, B. Moran, T. Nakamura, Energy release rate along a three-dimensional crack front in a thermally stressed body, International Journal of Fracture 30 (1986) 79–102.

[29] Y. Lei, N. P. O'Dowd, G. A. Webester, Fracture mechanics analysis of a crack in a residual stress field, International Journal of Fracture 106 (2000) 195–216.

[30] J. F. Yau, S. S. Wang, H. T. Corten, A mixed-mode crack analysis of isotropic solids using conservation laws of elasticity, Journal of Applied Mechanics 47 (1980) 335–341.

[31] T. Belytschko, T. Black, Elastic crack growth in finite elements with minimal remeshing, International Journal for Numerical Methods in Engineering 45 (1999) 601–620.

[32] J. M. Melenk, I. Babuška, The partition of unity finite element method: Basic theory and applications, Computer Methods in Applied Mechanics and Engineering 139 (1996) 289–314.

[33] S. Osher, J. A. Sethian, Fronts propagating with curvature dependent speed: Algorithms based on Hamilton-Jacobi formulations, Journal of Computational Physics 79 (1988) 12–49.

[34] M. Stolarska, D. Chopp, N. Moës, T. Belytschko, Modelling crack growth by level sets in the extended finite element method, International Journal for Numerical Methods in Engineering 51 (2001) 943–960.

[35] N. Moës, J. Dolbow, T. Belytscheko, A finite element method for crack growth without remeshing, International Journal for Numerical Methods in Engineering 46 (1999) 131–150.

[36] F. Wagner, G. Becker, K. Behringer, D. Campbell, A. Eberhagen, W. Engelhardt, G. Fussmann, O. Gehre, J. Gernhardt, G. v. Gierke, G. Haas, M. Huang, F. Karger, M. Keilhacker, O. Klüber, M. Kornherr, K. Lackner, G. Lisitano, G. G. Lister, H. M. Mayer, D. Meisel, E. R. Müller, H. Murmann, H. Niedermeyer, W. Poschenrieder, H. Rapp, H. Röhr, F. Schneider, G. Siller, E. Speth, A. Stäbler, K. H. Steuer, G. Venus, O. Vollmer, Z. Yü, Regime of improved confinement and high beta in neutral-beam-heated divertor discharges of the ASDEX tokamak, Physical Review Letters 49 (1982) 1408.

[37] H. Zohm, Edge localized modes (ELMs), Plasma Physics and Controlled Fusion 38 (1996) 105.

[38] P. Monier-Garbet, P. Andrew, P. Belo, G. Bonheure, Y. Corre, K. Crombe, P. Dumortier, T. Eich, R. Felton, J. Harling, J. Hogan, A. Huber, S. Jachmich, E. Joffrin, H. Koslowski, A. Kreter, G. Maddison, G. Matthews, A. Messiaen, M. Nave, J. Ongena, V. Parail, M. Puiatti, J. Rapp, R. Sartori, J. Stober, M. Tokar, B. Unterberg, M. Valisa, I. Voitsekhovitch, M. von Hellermann, JET-EFDA contributors, Impurity-seeded ELMy H-modes in JET, with high density and reduced heat load, Nuclear Fusion 45 (2005) 1404–1410.

[39] A. W. Degeling, Y. R. Martin, J. B. Lister, L. Villard, V. N. Dokouka, V. E. Lukash, R. R. Khayrutdinov, Magnetic triggering of ELMs in TCV, Plasma Physics and Controlled Fusion 45 (2003) 1637.

[40] P. Lang, G. Conway, T. Eich, L. Fattorini, O. Gruber, S. Günter, L. Horton, S. Kalvin, A. Kallenbach, M. Kaufmann, G. Kocsis, A. Lorenz, M. Manso, M. Maraschek, V. Mertens, J. Neuhauser, I. Nunes, W. Schneider, W. Suttrop, H. Urano, the ASDEX Upgrade Team, ELM pace making and mitigation by pellet injection in ASDEX upgrade, Nuclear Fusion 44 (2004) 665.

[41] T. E. Evans, R. A. Moyer, K. H. Burrell, M. E. Fenstermacher, I. Joseph, A. W. Leonard, T. H. Osborne, G. D. Porter, M. J. Schaffer, P. B. Snyder, P. R. Thomas, J. G. Watkins, W. P.

West, Edge stability and transport control with resonant magnetic perturbations in collisionless tokamak plasmas, Nature Physics 2 (2006) 419–423.

[42] B. Hudson, T. Evans, T. Osborne, C. Petty, P. Snyder, E. Unterberg, ELM suppression by resonant magnetic perturbation in high-performance, stationary plasmas, Nuclear Fusion 50 (2010) 045006.

[43] A. Loarte, M. Sugihara, M. Shimada, A. Kukushkin, D. Campbell, M. Pick, C. Lowry, M. Merola, R. Pitts, V. Riccardo, G. Arnoux, W. Fundamenski, G. Matthews, S. Pinches, A. Kirk, E. Nardon, T. Eich, A. Herrmann, G. Pautasso, A. Kallenbach, Power and particle fluxes at the plasma edge of ITER: Specifications and physics basis, 22nd IAEA Fusion Energy Conference, Geneva, Switzerland, 2008.

[44] N. Klimov, V. Podkovyrov, A. Zhitlukhin, D. Kovalenko, B. Bazylev, G. Janeschitz, I. Landman, S. Pestchanyi, G. Federici, A. Loarte, M. Merola, J. Linke, T. Hirai, J. Compan, An experimental study of PFCs erosion under ITER-like transient loads at plasma gun facility QSPA, 18th PSI Conference, Toledo, Spain, 2008.

[45] G. Federici, A. Loarte, G. Strohmayer, Assessment of erosion of the ITER divertor targets during type I ELMs, Plasma Physics and Controlled Fusion 45 (2003) 1523.

[46] T. Hirai, G. Pintsuk, J. Linke, M. Batilliot, Cracking failure study of ITER-reference tungsten grade under single pulse thermal shock loads at elevated temperatures, Journal of Nuclear Materials 390-391 (2009) 751–754.

[47] G. Pintsuk, A. Prokhodtseva, I. Uytdenhouwen, Thermal shock characterization of tungsten deformed in two orthogonal directions, Journal of Nuclear Materials 417 (2011) 481–486.

[48] M. Wirtz, J. Linke, G. Pintsuk, L. Singheiser, I. Uytdenhouwen, Comparison of the thermal shock performance of different tungsten grades and the influence of microstructure on the damage behaviour, Physica Scripta T145 (2011) 014058.

[49] J. Linke, T. Loewenhoff, V. Massaut, G. Pintsuk, G. Ritz, M. Roedig, A. Schmidt, C. Thomser, I. Uytdenhouwen, V. Vasechko, M. Wirtz, Performance of different tungsten grades under transient thermal loads, Nuclear Fusion 51 (2011) 073017.

[50] I. Garkusha, I. Landman, J. Linke, V. Makhlaj, A. Medvedev, S. Malykhin, S. Peschanyi, G. Pintsuk, A. Pugachev, V. Tereshin, Performance of deformed tungsten under ELM-like plasma exposures in QSPA Kh-50, Journal of Nuclear Materials 415 (2011) 481–486.

[51] S. E. Pestchanyi, J. Linke, Simulation of cracks in tungsten under ITER specific transient heat loads, Fusion Engineering and Design 82 (2007) 1657–1663.

[52] T. Hirai, G. Pintsuk, Thermo-mechanical calculations on operation temperature limits of tungsten as plasma facing material, Fusion Engineering and Design 82 (2007) 389–393.

[53] K. Kamiya, N. Asakura, J. Boedo, T. Eich, G. Federici, M. Fenstermacher, K. Finken, A. Herrmann, J. Terry, A. kirk, B. Koch, A. Loarte, R. Maingi, R. Maqueda, E. Nardon, N. Oyama, R. Sartori, Edge localized modes: Recent experimental findings and related issues, Plasma Physics and Controlled Fusion 49 (2007) S43.

[54] J. Linke, H. Bolt, R. Duwe, W. Kühnlein, A. Lodato, M. Rödig, K. Schöpflin, B. Wiechers, High heat flux simulation experiments with improved electron beam diagnostics, Journal of Nuclear Materials 283-287 (2000) 1152–1156.

[55] I. Uytdenhouwen, M. Decréton, T. Hirai, J. Linke, G. Pintsuk, G. V. Oost, Influence of recrystallization on thermal shock resistance of various tungsten grades, Journal of Nuclear Materials 363-365 (2007) 1099–1103.

[56] G. Pintsuk, Armour material optimisation-testing of tungsten under high cyclic transient thermal loads, Presented at the EFDA-Meeting, Garching, Germany, 2011.

[57] A. Faghri, Y. Zhang, Transport Phenomena in Multiphase Systems, Elsevier, 2006.

[58] H. S. Carslaw, J. C. Jaeger, Conduction of Heat in Solids, 2nd Edition, Oxford University Press, New York, 1959.

[59] W. Mack, U. Gamer, Stress distribution in an elastic plastic disk subjected to a circular heat source, Journal of Thermal Stresses 6 (1983) 323–336.

[60] M. Ishihara, Y. Tanigawa, R. Kawamura, N. Noda, Theoretical analysis of thermoelastoplastic deformation of a circular plate due to a partially distributed heat supply, Journal of Thermal Stresses 20 (1997) 203–225.

[61] B. Gludovatz, S. Wurster, A. Hoffmann, R. Pippan, Fracture toughness of polycrystalline tungsten alloys, International Journal of Refractory Metals and Hard Materials 28 (2010) 674–678.

[62] I. Uytdenhouwen, Degradation of first wall materials under ITER relevant loading conditions, Ph.D. thesis, University Gent (2011).

[63] G. D. Temmerman, J. Zielinski, S. van Diepen, L. Marot, M. Price, ELM simulation experiments on Pilot-PSI using simultaneous high flux plasma and transient heat/particle source, Nuclear Fusion 51 (2011) 073008.

[64] P. Gumbsch, Brittle fracture and the brittle-to-ductile transition of tungsten, Journal of Nuclear Materials 323 (2003) 304–312.

[65] B. Riccardi, P. Gavila, R. Giniatulin, V. Kuznetsov, R. Rulev, N. Klimov, D. Kovalenko, V. Barsuk, V. Koidan, S. Korshunov, Effect of stationary high heat flux and transient ELMs-like heat loads on the divertor PFCs, Fusion Engineering and Design 88 (2013) 1673 – 1676.

[66] A. Huber, A. Arakcheev, G. Sergienko, I. Steudel, M. Wirtz, A. V. Burdakov, J. W. Coenen, A. Kreter, J. Linke, P. Mertens, V. Philipps, G. Pintsuk, M. Reinhart, U. Samm, A. Shoshin, B. Schweer, B. Unterberg, M. Zlobinski, Investigation of the impact of transient heat loads applied by laser irradiation on ITER-grade tungsten, Physica Scripta T159 (2014) 014005.

[67] T. Dümmr, J. C. Lasalvia, G. Ravichandran, M. A. Meyers, Effect of strain rate on plastic flow and failure in polycrystalline tungsten, Acta Metallurgica 46 (1998) 6267–6290.

[68] G. Ambrosino, M. Ariola, G. D. Tommasi, A. Pironti, Plasma vertical stabilization in the ITER tokamak via constrained static output feedback, Transactions on Control Systems Technology 19 (2011) 376–381.

[69] J. M. Linke, T. Hirai, M. Rödig, L. A. Singheiser, Performance of plasma-facing materials under intense thermal loads in tokamaks and stellarators, Fusion Science and Technology 46 (2004) 142–151.

[70] A. Cardella, H. Gorenflo, A. Lodato, K. Ioki, R. Raffray, Effects of plasma disruption events on ITER first wall materials, Journal of Nuclear Materials 283-287 (2000) 1105–1110.

[71] J. Linke, P. Lorenzetto, P. Majerus, M. Merola, D. Pitzer, M. Roedig, EU development of high heat flux components, Fusion Science and Technology 47 (2005) 678–685.

[72] M. Sommerer, Multiple-Use-Technologie der Fusionsforschung: Mikrostrukturelle Aspekte des thermozyklischen Bruchverhaltens von Wolfram in industrieller Anwendung, Ph.D. thesis, Technische Universität München (in preparation).

[73] J. Linke, High heat flux performance of plasma facing materials and components under service conditions in future fusion reactors, Fusion Science and Technology 49 (2006) 455–464.

[74] Y. Ishijima, H. Kurishita, K. Yubuta, H. Arakawa, M. Hasegawa, Y.Hiraoka, T. Takida, K. Takebe, Current status of ductile tungsten alloy development by mechanical alloying, Journal of Nuclear Materials 775 (2004) 329–333.

[75] J.-H. You, I. Komarova, Probabilistic failure analysis of a water-cooled tungsten divertor: Impact of embrittlement, Journal of Nuclear Materials 375 (2008) 283–289.

[76] M. Miskiewicz, J.-H. You, Impact of plastic softening of over-aged CuCrZr alloy heat sink tube on the structural reliability of a plasma-facing component, Fusion Engineering and Design 83 (2008) 66–71.

[77] J. P. Blanchard, C. Martin, Fracture and creep in an all-tungsten divertor for ARIES, Fusion Science and Technology 64 (2013) 435–439.

[78] D. Maisonnier, I. Cook, P. Sardain, R. Andreani, L. D. Pace, R. Forrest, L. Giancarli, S. Hermsmeyer, P. Norajitra, N. Taylor, A conceptual study of commercial fusion power plants, EFDA(05)-27/4.10, 2005.

[79] F. Crescenzi, A. Moriani, S. Roccella, E. Visca, M. Richou, Water-cooled divertor target design study CuCrZr/W monoblock concept, EFDA report: TA WP13-DAS02-T02-D02, 2013.

[80] J. Lemaitre, J.-L. Chaboche, Mechanics of Solid Materials, 1st Edition, Cambridge University Press, 1994.

[81] P. J. Armstrong, C. O. Frederick, A mathematical representation of the multiaxial Bauschinger effect, G.E.G.B. Report RD/B/N (1966) 731.

[82] J. Chaboche, Constitutive equations for cyclic plasticity and cyclic viscoplasticity, International Journal of Plasticity 5 (1989) 247–302.

[83] M. Lipa, A. Durocher, R. Tivey, T. Huber, B. Schedler, J. Weigert, The use of copper alloy CuCrZr as a structural material for actively cooled plasma facing and in vessel components, Fusion Engineering and Design 75-79 (2005) 469–473.